FLOOD INUNDATION MAPPING AND HAZARD ASSESSMENT- A GOOGLE EARTH ENGINE APPROACH: CASE OF THE LOWER AWASH RIVER BASIN, ETHIOPIA.

EYOB DANGISO WAKO

A THESIS SUBMITTED TO
THE DEPARTMENT OF WATER RESOURCES ENGINEERING
SCHOOL OF CIVIL ENGINEERING AND ARCHITECTURE

PRESENTED IN PARTIAL FULFILLMENT OF THE REQUIREMENT FOR THE DEGREE OF MASTER'S IN WATER RESOURCES ENGINEERING (SPECIALIZATION IN HYDRAULIC ENGINEERING)

OFFICE OF GRADUATE STUDIES
ADAMA SCIENCE AND TECHNOLOGY UNIVERSITY

JUNE, 2024
ADAMA, ETHIOPIA

Flood Inundation Mapping and Hazard Assessment- a Google Earth Engine Approach**:** Case of The Lower Awash River Basin, Ethiopia.

Eyob Dangiso Wako

ID: PGR/28091/15

Advisor: Mengistu Addis Jenbere (PhD)

A Thesis Submitted To
The Department of Water Resources Engineering
School Of Civil Engineering and Architecture

Presented In Partial Fulfillment of The Requirement for The Degree of Master's in Water Resources Engineering (Specialization in Hydraulic Engineering)

Office Of Graduate Studies
Adama Science and Technology University

June, 2024
Adama, Ethiopia

DECLARATION

I hereby declare that this Master Thesis entitled **"Flood Inundation Mapping and Hazard Assessment- a Google Earth Engine Approach: Case of The Lower Awash River Basin, Ethiopia"** is my original work. That is, it has not been submitted for the award of any academic degree, diploma or certificate in any other university. All sources of materials used for this thesis have been duly acknowledged through appropriate citations.

Eyob Dangiso	_____	_____
Name of student	Signature	Date

RECOMMENDATION

I, the advisor of this thesis, hereby certify that I have read and revised version of the thesis entitled **"Flood Inundation Mapping and Hazard Assessment- a Google Earth Engine Approach: Case of The Lower Awash River Basin, Ethiopia"** prepared under my guidance by Eyob Dangiso Wako submitted in partial fulfillment of the requirements for the degree of masters of science in Water Resources Engineering (Specialization in Hydraulic Engineering). Therefore, I recommend the submission of a revised version of the thesis to the department following the applicable procedures.

Mengistu Addis (PhD) _____ _____

Major Advisor/Supervisor Signature Date

APPROVAL PAGE

I, the advisor of the thesis entitled **"Flood Inundation Mapping and Hazard Assessment- a Google Earth Engine Approach: Case of The Lower Awash River Basin, Ethiopia"** and developed by Eyob Dangiso Wako, hereby certify that the recommendation and suggestions made by the board of examiners are appropriately incorporated into the final version of the thesis.

Mengistu Addis (PhD)	_____	_____
Major Advisor/Supervisor	Signature	Date

We, the undersigned members of the Board of Examiners of the thesis by Eyob Dangiso Wako, have read and evaluated the thesis entitled **"Flood Inundation Mapping and Hazard Assessment- a Google Earth Engine Approach: Case of The Lower Awash River Basin, Ethiopia"** and examined the candidates during the open defense. This is, therefore, to certify that the thesis is accepted for partial fulfillment of the requirement of the degree of Master of Science in Water Resources Engineering (Specialization in Hydraulic Engineering).

_____	_____	_____
Chairperson	Signature	Date
_____	_____	_____
Internal Examiner	Signature	Date
_____	_____	_____
External Examiner	Signature	Date

Finally, approval and acceptance of the thesis is contingent upon submission of its final copy to the Office of Postgraduate Studies (OPGS) through the Department Graduate Council (DGC) and School Graduate Committee (SGC).

_____	_____	_____
Department Head	Signature	Date
_____	_____	_____
School Dean	Signature	Date
_____	_____	_____
Office of Postgraduate Studies	Signature	Date

ACKNOWLEDGEMENT

First, I would like to express my gratitude to Almighty God, whose boundless mercy and guidance have illuminated my academic journey and enabled the completion of this MSc thesis.

I am profoundly grateful to my advisor, Mengistu Addis (PhD), for his unwavering support, invaluable guidance, and scholarly mentorship throughout the research process. I would like to extend my heartfelt appreciation for his expertise, encouragement, and constructive feedback, which have been instrumental in shaping the direction of this thesis

I would also like to acknowledge Dereje Berhanu (PhD) for graciously providing me with the necessary data and information for conducting this research. His generosity and willingness to share knowledge have significantly enriched the quality of this work.

Furthermore, I sincerely thank the Department of Water Resources Engineering staff members for their assistance, cooperation, and support throughout my academic journey. Their dedication to excellence and commitment to fostering a conducive learning environment has been instrumental in my growth and development.

I am deeply indebted to Adama Science and Technology University for sponsoring my MSc studies. Their investment in my education has been invaluable, and I am profoundly grateful for the opportunities provided to pursue advanced studies in my field of interest.

I thank the Ministry of Water and Energy, Ethiopia, for delivering the necessary data for this study. Their contribution has been essential in facilitating the research process and enhancing the depth of this thesis.

Last but certainly not least, I extend my heartfelt gratitude to my beloved family for their unwavering love, encouragement, and support throughout this endeavor. Their sacrifices, understanding, and belief in my abilities have been my source of strength and motivation.

This thesis is a testament to the collective efforts, support, and encouragement of all those mentioned above. I am profoundly grateful to every one of them for their contributions to this significant milestone in my academic journey.

Contents

DECLARATION ii
RECOMMENDATION iii
APPROVAL PAGE iv
ACKNOWLEDGEMENT v
Contents vi
LIST OF TABLES ix
LIST OF FIGURES x
LIST OF ABBREVIATIONS xii
ABSTRACT xv
1 INTRODUCTION 1
1.1 Background 1
1.2 Statement of the Problem 4
1.3 Objectives: 6
1.3.1 General Objectives 6
1.3.2 Specific Objectives: 6
1.4 Research Questions 7
1.5 Significance of the Study 7
1.6 Scope of the Study 8
1.7 Thesis Organization 8
2 LITERATURE REVIEW 9
2.1 The Concept of Flood 9
2.2 Hydrological Data Quality Assessment 9
2.2.1 Filling of Missed Hydrological Data 9
2.2.2 Data Homogeneity Analysis 11
2.3 Estimation of Flood Quantiles 11
2.4 Hydrodynamic model 13
2.4.1 Hydraulic Modeling (HEC-RAS) 13
2.4.2 HEC-RAS-One Dimensional (1D) Model 14
2.4.3 HEC-RAS Two-Dimensional Model (2D Model) 15
2.5 Flood Inundation Mapping 16

2.6 Flood Hazard Assessment 18
2.7 Flood Risk Assessment 20
2.8 Application of Google Earth Engine Cloud Platform 20
2.8.1 Overview of Google Earth Engine (GEE) Platform 20
2.9 Studies Held on Awash Basin 22
3 MATERIALS AND METHODS 23
3.1 Study Area Description 23
3.1.1 Location 23
3.1.2 Climate 24
3.1.3 Soil 24
3.1.4 Land Use Land Cover 25
3.2 Datasets 26
3.3 Data Quality Analysis 28
3.3.1 Filling of Missed Data 28
3.3.2 Data Homogeneity Analysis 28
3.3.3 Test for Outliers 29
3.4 Flood Quantile Estimation Methods 29
3.4.1 Goodness of Fit Test 30
3.5 HEC-RAS Modelling Approach and Inundation Mapping 33
3.5.1 1D HEC-RAS Modeling 34
3.5.2 2D Modelling Process 36
3.5.3 Flood Inundation Mapping 39
3.6 Model Calibration and Validation of the hydrodynamic model 39
3.6.1 Calibration 39
3.6.2 Validation 40
3.7 Flood Hazard Assessment 42
3.8 Application of Google Earth Engine Cloud Platform 43
3.8.1 Methods to Flood Mapping Using Google Earth Engine Platform 43
4 RESULTS AND DISCUSSIONS 47
4.1 Hydrological Data Analysis 47
4.1.1 Filling of Missed Data 47

4.1.2 Homogeneity Analysis 50
4.1.3 Outlier Detection and Treatment 57
4.2 Goodness of Fit and Flood Quantile Estimation 58
4.2.1 Goodness of Fit Analysis 58
4.2.2 Flood Quantiles Estimation 59
4.3 HEC-RAS Model Computation 62
4.4 Calibration and Validation of HEC-RAS Model 63
4.4.1 Calibration 63
4.4.2 Validation 66
4.5 Flood Hazard Assessment 69
4.5.1 1D HEC-RAS Model Flood Inundation and Hazard Assessment 69
4.5.2 2D HEC-RAS Model Flood Inundation and Hazard Assessment 74
4.6 Flood Inundation mapping Using Google Earth Engine and Hazard Assessment 80
4.6.1 Hazard Assessment From Google Earth Engine Flood Inundation Results 83
4.7 Discussions 84
4.7.1 From 1D HEC-RAS Simulation Results 84
4.7.2 From 2D HEC-RAS Simulation Results 86
4.7.3 From the results GEE 88
4.7.4 Overall Discussions Regarding on the Results of 1D, 2D, and GEE 89
5 CONCLUSION AND RECOMMENDATION 93
5.1 Conclusion 93
5.2 Recommendation 94
REFERENCES 96
APPENDICES 104

LIST OF TABLES

Table 3. 1 Data needed and their sources 27
Table 3. 2 Acquired stream flow data 27
Table 3. 3 Software Used in the Study 28
Table 3. 4 L-Moments of some common distributions (Hosking, 1990) 32
Table 4. 1 Python code used to fill missed data 48
Table 4. 2 Python code used to check non-homogeneity 51
Table 4. 3 Python code used to treat non-homogeneity by identifying the change point 54
Table 4. 4 Outlier detection and treatment 57
Table 4. 5 HEC-SSP statistical software output KS test 59
Table 4. 6 Stations near the Dubti station with their catchment area and flood quantiles 59
Table 4. 7 Developed equations to estimate flood quantiles for Dubti Station 60
Table 4. 8 Flood quantiles for different return periods for the hydrological stations 61
Table 4. 9 Calibration result of both Mille and Logia River Water Surface Elevation (Water level) 63
Table 4. 10 performance criteria for model calibration and validation (Tamiru & Dinka, 2021) 64
Table 4. 11 Specification of Landsat 7 (Deoli et al., 2022) 66
Table 4. 12 Validation Results 68
Table 4. 13 Flood hazard classification based on flood depth and velocity (Ahmad et al., 2022; Ongdas et al., 2020) 71
Table 4. 14 Representation of hydraulic properties created within HEC-RAS. Elevation vs. Area (a), Elevation vs. wetted perimeter (b). elevation vs. manning's coefficient (c). elevation vs conveyance (d). 75
Table 4. 15 Affected areas and Hazard level from 2D inundation depth 77
Table 4. 16 Affected areas and Hazard level from 2D flow velocity 78
Table 4. 17 Flood Affected Land Use Land Cover from 2D inundation depth results 80
Table 4. 18 GEE Flood Affected Land Use Land Cover 84

LIST OF FIGURES

Figure 3. 1 Location Map of the Study Area. 23
Figure 3. 2 Monthly average rainfall distribution of the station 24
Figure 3. 3 Soil map of the study area 25
Figure 3. 4 LULC map of the study area 26
Figure 3. 5 Geometric data..... 34
Figure 3. 6 Steady flow data for different return periods 35
Figure 3. 7 Manning's roughness coefficient assigned to the 2D region 38
Figure 3. 8 Created a geometric layer using a two-dimensional flow area cell mesh 38
Figure 3. 9 Data process algorithm and 2D hydrodynamic model in HEC-RAS (Brunner, 2016; Trambadia et al., 2023) 42
Figure 3. 10 Process algorithm showing the flood inundation mapping via the GEE platform. .. 46
Figure 4. 1 Missed data graphical plot for Mille station..... 47
Figure 4. 2 Filled data graphical plot for Mille station 50
Figure 4. 3 Before Homogenization..... 53
Figure 4. 4 After Homogenization 55
Figure 4. 5 Homogeneity test using Rainbow software tool for Mille Station 57
Figure 4. 6 Catchment Area Vs flood quantiles Mille, Tendaho, and Logia stations..... 60
Figure 4. 7 Rating curve of Mille River Station 22400 65
Figure 4. 8 Rating curve of Logia River station 21600 65
Figure 4. 9 NDWI calculated from satellite image in August 2005 67
Figure 4. 10 MNDWI calculated from satellite image in August 2005..... 67
Figure 4. 11 Inundation boundary for the year August 2005..... 68
Figure 4. 12 Inundation depth 500 Yr..... 70
Figure 4. 13 Velocity map 500 Yr 70
Figure 4. 14 Flood events Vs Inundation area 71
Figure 4. 15 Flood affected areas and Hazard Levels for different return periods in case of inundation depth..... 72
Figure 4. 16 Flood affected areas and Hazard Levels for different return periods in case of Velocity map 72
Figure 4. 17 Percent of Hazard level change in area from depth to velocity..... 73
Figure 4. 18 Flood affected areas and Hazard Levels for different return periods in terms of Land use Land cover 74
Figure 4. 19 Maximum depth on 2D Mille river profile..... 76
Figure 4. 20 Maximum depth on 2D Logia river profile. 77
Figure 4. 21 2D flood hazard level of affected areas in bar graph in terms of inundation depth. 78
Figure 4. 22 2D flood hazard level of affected areas in bar graph in terms of flow velocity. 79
Figure 4. 23 Percent of area change bar graph between 2D depth and velocity..... 79
Figure 4. 24 Flood Affected Land Use Land Cover from 2D inundation results in bar graph..... 80
Figure 4. 25 Before flood (a) and After flood (b) 81

Figure 4. 26 Speckle filter..... 81
Figure 4. 27 Initial flooded area..... 82
Figure 4. 28 Apply Masks..... 82
Figure 4. 29 Flooded Area in ha 83
Figure 4. 30 GEE final Flood Affected Land Use Land Cover 84

LIST OF ABBREVIATIONS

1D	One-Dimensional
2D	Two-Dimensional
AD	Anderson-Darling
AMS	Annual Maximum Series
ANRS	Afar National Regional State
ArcGIS	Geographic Information System software
BRT	Buishand Range Test
CDF	Cumulative Distribution Function
DEM	Digital Elevation Model
DMC	Double Mass Curve
EV1	Extreme Value Type 1
GEE	Google Earth Engine
GEV	Generalized Extreme Value
GIS	Geographic Information System
GL	Generalized Logistic
GoF	Goodness of Fit
GP	Generalized Pareto
GRD	Ground Range Detected
GUI	Graphical User Interface
HEC-GeoRAS	Hydrologic Engineering Center's Geographic River Analysis System
HEC-RAS	Hydrologic Engineering Center's River Analysis System
HEC-SSP	Hydrologic Engineering Center's Statistical Software Package
IFM	Index Flood Method
JSON	JavaScript Object Notation

KS	Kolmogorov-Smirnov
LARB	Lower Awash River Basin
LMRD	L-Moment Ratio Diagram
LN2	Two-Parameter Log Normal
LN3	Three-Parameter Log Normal
LP3	Log Pearson Type III
LULC	Land Use Land Cover
MI	Multiple Imputation
MNDWI	Modified Normalized Difference Water Index
MoWE	Ministry of Water and Energy
NDVI	Normalized Difference Vegetation Index
NDRMC	National Disaster Risk Management Commission
NIR	Near-Infrared
NSE	Nash-Sutcliffe Efficiency
PDF	Probability Density Function
PMF	Probable Maximum Flood
PMP	Probable Maximum Precipitation
PPCC	Probability Plot Correlation Coefficient
QGIS	Quantum Geographic Information System
QRT	Quantile Regression Technique
RAS	River Analysis System
RFFA	Regional Flood Frequency Analysis
RGB	Red, Green, Blue
RS	Remote Sensing
SAR	Synthetic Aperture Radar

SDGs	Sustainable Development Goals
SNHT	Standard Normal Homogeneity Test
SVE	Saint-Venant Equations
SWI	Short-Wave Infrared
TIN	Triangulated Irregular Network
USACE	United States Army Corps of Engineers
VH	Vertical Horizontal Polarization
VNR	Von Neumann Ratio
VV	Vertical Vertical Polarization
WMO	World Meteorological Organization
WSE	Water Surface Elevation
WL	Water Level
XS	Cross Section

ABSTRACT

In Ethiopia, flooding is a serious natural hazard that can result in fatalities, property damage, and interruption of livelihoods. Floods are becoming more frequent and powerful, putting sustainable development at risk and calling for efficient flood control measures. This thesis employed Google Earth Engine (GEE) and an integrated hydrodynamic model to map flood inundation and analyze hazards in the Lower Awash River Basin, Ethiopia. The project's objective was to simulate the *Lower Awash River basin's water level with flood mapping, to make a hazard assessment for the sub-basin, to compare the Google Earth Engine capabilities with the integration of the hydrodynamic model. The stream flow data of ten gauging stations were analyzed for estimating flood quantiles on the gauged site by applying regional flood frequency analysis based on an L-moment-based index flood. From probability distribution functions; generalized Pareto, generalized extreme value, generalized logistic, and Pearson III were selected as best-fitted distributions for 2, 3, 4, and 1 gauging stations from the total stations respectively. The flood quantiles were estimated using the best-fitted distributions for the specified stations for the return periods of 5, 10, 20, 50, 100, 200, 500. At-site quantiles are estimated and fed into HEC-RAS as profiles for developing inundation extent, depth, and flow velocity based on the regional quantiles and the index flood. HEC-RAS Simulation and inundation results were calibrated and validated. Calibration was undertaken for the water level of two stations, Mille and Logia. The performance of the model examined Adjusted n value for the main river channel was 0.042. NSE, PBIAS, and R2 give of values 0.714273 (Very Good), -7.200516629 (Very Good), and 0.8785 (Very Good) respectively for Mille River. NSE, PBIAS, and R2 give values 0.755333 (Very Good), 1.384083045 (Very Good), and 0.8576 (Very Good) respectively for Logia River. The historical flood extent from satellite images and the HEC-RAS simulation were compared for model validation, yielding a good agreement by the overlapping percentage of 88.72. Hazard level and affected land use were computed. A considerable increase in inundated areas was found with increased return periods. The bulk of LARB's floodplain is classified as having very low, low, medium, and high hazards. the results from the three analyses indicate the increasing risk and vulnerability of different areas to flooding events as the return period extends. Agriculture and range land consistently showed high vulnerability. Gewane and Dubti emerged as the most flood-prone locations across all three analyses and agriculture and rangeland were the most affected land uses from the 1D, 2D HEC-RAS, and GEE results. The distribution of hazard levels and affected land use varied across different regions, highlighting the complex interactions between flood hazards and land vulnerability. Therefore, it can be concluded that GEE is a good alternative for flood mapping, especially for data-scarce areas.*

Key Words: Hydrodynamic model, GEE, GIS, LARB, Flood Inundation

1 INTRODUCTION

1.1 Background

Floods are considered the most damaging threat in the world. According to (Shadmehri Toosi et al., 2020), floods cause more deaths than any other hydrometeorological disaster and harm the socio-economic development of many countries. Moreover, there are significant worries about the sustainable development of flood-prone countries due to the increasing frequency and intensity of these flood events around the world (Dewan, 2015). The principal factor contributing to these exceptional floods is the increase in temperature and precipitation that has transpired since the 1950s as a result of increased greenhouse gas emissions and human activities (Bhandari et al., 2017). A sizeable amount of the total number of natural catastrophes reported worldwide are reportedly caused by this natural hazard. This is a challenge for both wealthy and developing nations. Several global locations have experienced a significant increase in the frequency of climate-related disasters as a result of rapid changes in hydro-climatic conditions and other disturbances. The development of socioeconomic activity and changes in land use in places susceptible to flooding are additional factors that may impact the frequency of flood disasters. Such activities affect how a river's hydrology naturally behaves and how floodplains react to a flood hazard (Ongdas et al., 2020).

These drivers are not entirely preventable due to their complexity. However, if sufficient flood risk management techniques and knowledge about the places that are prone to flooding are accessible beforehand, it is possible to lower the associated hazards. Understanding, evaluating, and forecasting floods and their effects has long been essential. This is now more attainable thanks to recent developments in technology and processing power. Utilizing cloud computing services and parallel computing to satisfy the enormous processing demand is one such example. Furthermore, the integration of Remote Sensing (RS) and Geographic Information Systems (GIS) data has greatly facilitated the process of creating flood hazard maps. In addition to providing data for model building, remote sensing also gives data for model validation (Ahmed et al., 2021; Ongdas et al., 2020; Sajjad et al., 2020).

One of Ethiopia's most common natural disasters, flooding drastically destroys lives and means of subsistence in several parts of the country. Ethiopia's lowland plains and highland ranges, which have natural drainage systems formed by the major river basins, and excessive rainfall are the main causes of floods in the nation. In the country, prolonged periods of heavy rains

usually result in rivers overflowing and submerging lowland plains areas adjacent to the rivers. Low-lying Gambella districts along the Baro River, sections of the Somali region along the Wabe Shebelle, Genale, and Dawa Rivers, and parts of the Oromia and Afar regions along the upper, middle, and downstream plains of the Awash River are some of the primary river areas that are prone to flooding (NDRMC, 2018).

According to (Getahun YS, 2015), floods are characterized by an abundance of water that surpasses the carrying capacity of a river channel, lake, pond, reservoir, drainage system, dam, or other water-related structure, submerging the land outside of water bodies. Because floods are the result of both hydrological and climatic causes, they are among the most destructive natural occurrences. This is a natural phenomenon in which water explodes and overtops a channel, either naturally occurring or man-made, briefly inundating the land's surface beyond the body of water.

The severity of floods is apparent when a country lacks structural affordability due to financial constraints (Chen et al., 2014). Currently, river floods pose a serious risk to people who live next to rivers everywhere in the world (Cirella & Iyalomhe, 2018). The number of households impacted by this disaster and left without shelter is rapidly increasing throughout Africa, and Ethiopia is not an exception (Desalegn & Mulu, 2021; Thiemig et al., 2011). The country is become increasingly susceptible to flooding as a result of its topography, high rainfall, unexpected damage to river banks, overflowing river banks, insufficient urban drainage systems, steep channel design slopes, and changes in land use and cover (Gashaw & Legesse, 2011).

The early mapping, monitoring, and effect assessment of flood events is critical to the establishment of flood management, risk mitigation plans, and various preventive initiatives, as well as the coordination of flood relief activities. Because of the temporal and spatial aspects of floods, this knowledge is typically difficult to gather using standard methods (Psomiadis et al., 2020). For the purpose of identifying flood risks, flood-prone locations, and future mitigation methods, it is critical to assess flood risk and management practices. Comprehending the attributes of floods is crucial for formulating action plans for flood control and evaluating the effects of diverse management strategies. The simplest methods for interpreting the flood risk are in situ observations of flood episodes. However, in many underdeveloped nations, on-the-ground observations of the floods are unavailable. Furthermore, these observations-based flood analysis is restricted to particular flood events.

Consequently, using the RS data is one of the alternative methods for carrying out flood risk modeling studies (Albu et al., 2020; Hagen & Lu, 2011; Psomiadis et al., 2020; Su et al., 2021).

These geospatial tools have been widely used to map the results of simulation models of past flood occurrences, including flood levels and inundation extents. They have also been used to identify the critical infrastructure that is at risk (Dasallas et al., 2019; Santillan et al., 2016). These technologies also support the creation of flood forecasts and early warning systems in areas that are prone to flooding, which help control flood risks and become ready for emergencies (Asare-Kyei et al., 2015; Baky et al., 2019). To generate and validate the output of the flood model, assessing the probability of flooding, and identifying the infrastructure that is vulnerable (such as commercial and urban districts, transportation infrastructure, health and education facilities, etc.), RS is a crucial tool. According to (Santillan et al., 2016), GIS makes it possible to create automated flood models, flood risk assessments, which classify urban areas, settlements, and agricultural lands according to varying degrees of flooding, flood inundation maps, and other statistical analyses that might be useful in the creation of flood disaster management plans at various flood event levels.

The main instruments used in inundation mapping are hydrodynamic and hydraulic models. Their primary applications include planning flood management, estimating vulnerable areas, simulating flood occurrences, and identifying spatially distributed variables of relevance. Generally speaking, they explain the fluid motion and dynamics of the flood wave using mathematical equations based on the ideas of mass and momentum conservation. The user can select models with various dimensionalities (1D, 2D, etc.), numerical schemes (finite volume, finite difference, etc.), mesh representations (structured, unstructured, etc.), and equations (Kinematic Wave, Diffusion Wave, Muskingum, etc.) based on the study area and project goals (Ongdas et al., 2020).

The climate of the Earth is changing constantly, which presents serious problems for the ecosystem and society. The remote sensing community primarily uses geospatial datasets collected from mobile, satellite, and aircraft sensors to address these issues globally. However, during the past few decades, the enormous development of geographic information has exceeded the remote sensing community's ability to store, process, and visualize data. Processing and managing a significant number of heterogeneous satellite images taken by a variety of sensors is required for large-scale mapping, which presents a "Big Data" challenge. This has led to new problems with dataset processing, which have made the creation of

innovative methods for obtaining important information from remote sensing data necessary. In addition, processing a large number of satellite pictures from various sensors to create high-resolution damage assessment maps for vast areas (>10,000 sq km) at various time scales for disaster management applications is a challenge for the remote sensing community (Ghosh et al., 2022).

1.2 Statement of the Problem

Flooding is one of Ethiopia's regular issues. The frequency and magnitude have both rapidly increased during the last few decades. Floods mostly cause property and human casualties, damage to roads and electrical infrastructure, crop destruction, and malnourishment that follows. Most of the flooding in this stretch of the Awash River is caused by the Kessem and Kebena rivers, tributaries of the Awash from the western highland drainage. This could get worse with the large flood flow from Koka Reservoir. The Amibara Project Control Center, which is in charge of maintaining the dikes that protect the development from flooding, has become weaker as a result of repeated flooding, which has caused enormous financial losses over the past few years (Achamyeleh, 2003). Zones 1, 2, and 3 of the Afar Regional State are at risk of flooding, per reports from the UNDP Emergencies Unit for Ethiopia (1999) and (NDRMC, 2018). Zone 3 areas—Awash Fentale and Buremudaytu, Amibara, Dulecha, Gewane, Ambash, Sheleko, and Assoba—as well as Oromia East Showa (Dugda, Bora, Adama, Boset, Fentale, Wonji, and Ziekula)—are at risk of flooding.

On May 13, 2021, the UN announced that flooding that started in late April and affected three districts of Ethiopia had caused some 70,000 people to be relocated. A study from UNOCHA covering the period from April 26 to May 10, 2021, states that the flooding has had a major effect on Ethiopia's Somali, Afar, and Southern Nations, Nationalities, and People's (SNNP) areas. About 27,400 people have been forced to flee their homes in the Afar Region as a result of flooding in the woredas of Gulina, Ewa, Beyalo, Dulecha, Harunka, and Mile brought on by strong winds and rain (FloodList, 2021). On August 8, 2021, the Afar Regional State's Asayta Woreda locality saw catastrophic floods as a result of the River Awash overflowing its banks due to heavy rainfall. According to Aydahis Yasin, the head of the region's Disaster Risk Management and Food Security Bureau, flooding destroyed residential areas in 100 houses, forcing residents to evacuate. Furthermore, there was substantial crop damage on more than 50 hectares of seriously affected agricultural area. Furthermore, in some of the region's woredas, 90,000 residents in 40 villages within these three zones could be at risk of floods. The bureau

and other relevant stakeholders have implemented preventive measures and increased community awareness in high-risk locations (Fana FBC, 2021).

Since July, Ethiopia has been severely hit by water and heavy rain, affecting over 500,000 people and uprooting almost 300,000 others. Flooding began in the country in late July due to unusually high rainfall during the Kiremt season, which runs from June to September. According to a UN assessment, the flood of the Awash River has displaced 30,000 people by early August. Many of these people were in the Afar region. Significant damage was also done to Gambella, Oromia, SNNP, and Amhara. The UN Office for the Coordination of Humanitarian Affairs (OCHA) stated in a report dated September 6 that "heavy summer season (June-September) rains continue to cause flooding in many parts of the country." Up to now, 500,000 individuals have been impacted, including about 300,000 displaced. The Awash River burst its banks again on September 1, inundating parts of the Afar region's Amibara and Awash Fentale woredas. To evacuate flood victims, the government sent out a military chopper; according to local accounts, at least five people had perished. OCHA also noted that villages downstream are at higher risk of flooding due to releases from the Koka and Kesem dams. Working with the Oromia and Afar areas, the National Disaster Risk Management Commission (NDRMC) is attempting to evacuate (FloodList, 2020).

On August 5, 2020, the report by (Fana FBC, 2020) the Afar Regional State Disaster Prevention and Food Security Program Coordination Office disclosed that the overflow of the Awash River has displaced 32,000 people. This flood event, which occurred in six woredas, was triggered by heavy rainfall during the rainy season. Despite flood prevention efforts by the Awash Basin Authority, in collaboration with regional and federal governments, the unusual rainfall led to significant devastation. Displacement and Vulnerability: 32,000 people were displaced due to the overflow of the Awash River. Of these, 17,450 lived in the five kebeles of Asayta Woreda. Seven woredas along the Awash River basin are highly vulnerable to flooding. Additionally, 1,266 individuals in Kolodura and Geleali Kebeles have been surrounded by water since the overflow began. Risk and Vulnerability Assessment: An estimated 63,000 people are vulnerable to future floods, while 44,000 people in the lower and middle Awash regions are at risk of displacement due to flooding. Damage to Livelihoods: Extensive damage to crops and animals has been reported in the affected areas. Emergency Response and Relief: The government has provided relief to over 1,100 individuals in two kebeles of Asayta Woreda. Continuous and effective relief efforts are required to support the displaced and vulnerable populations. Flood Prevention Measures: Despite ongoing flood prevention activities by the

Awash Basin Authority, the measures were insufficient to prevent the devastation caused by the unusual rainfall. There is a need to evaluate and potentially enhance the current flood prevention and management strategies to mitigate future risks.

As a result, flooding in the LARB has frequently led to the eviction of thousands of people and the death of thousands of animals. Because of this, there is a significant flooding issue in the area that calls for careful consideration of suitable building design, flood forecasting, and flood risk assessment in order to control and reduce the damages brought on by river floods. We have to accept that there is no 100% reliable way to prevent flooding. However, more should be done to employ non-structural techniques like mapping and flood risk assessment. By using these maps, the local populace and the agencies responsible for managing floodplains can lessen the number of fatalities and damage caused by flooding. They could help warn the residents about the danger because they graphically depict the possibility of flooding.

In conclusion, the challenges outlined underscore the urgency and importance of conducting a comprehensive study titled "Riverine Flood Inundation Mapping and Hazard Assessment Using an Integrated Hydrodynamic Model and Google Earth Engine: Case of the Lower Awash River Basin, Ethiopia." This study aimed to address the critical issues of riverine flooding in the region by leveraging advanced hydrodynamic modeling techniques and the capabilities of Google Earth Engine. By integrating data-driven approaches with scientific modeling, the study seeks to improve flood mapping accuracy, enhance hazard assessment capabilities, and inform evidence-based decision-making for flood risk management and disaster preparedness in the Lower Awash River Basin.

1.3 Objectives:

1.3.1 General Objectives

The general objective of the study was to comprehensively map the riverine flood and hazard assessment in the Lower Awash River basin by integrating the HEC-RAS model and Google Earth Engine.

1.3.2 Specific Objectives:

- To simulate the Lower Awash River basin's water level with flood mapping.
- To assess the flood hazard for the Lower Awash River basin.
- To compare the Google Earth Engine capabilities with the integration of the hydrodynamic model.

1.4 Research Questions

- How can we accurately simulate water levels in the Lower Awash River basin using hydrodynamic models?
- Which areas within the Lower Awash River basin are most hazardous to flooding?
- How effectively does the hydrodynamic model integrate with Google Earth Engine (GEE) for simulating water flow and flood dynamics?

1.5 Significance of the Study

For underdeveloped countries where the majority of the population is dependent on agriculture, flood assessment is essential (Trambadia et al., 2023). The planned study would provide a thorough evaluation of flood inundation patterns and advance knowledge of flood dynamics in the Lower Awash River basin. Future efforts to evaluate and reduce flood risks and protect infrastructure, towns, and agricultural areas will require this knowledge. Modern modeling methods will be used in this study with the integration of a sophisticated hydrodynamic model and the use of Google Earth Engine. Compared to conventional methods, this novel approach will allow for more precise and thorough assessments of flood inundation, which will eventually improve prediction reliability and aid in well-informed decision-making.

The investigation's findings will offer a solid foundation for the development of effective early warning systems. Comprehending the geographical and temporal patterns of flood inundation will enable prompt alerts to be distributed to areas at risk, enabling preventative actions to reduce property damage and potential casualties during flood events. Resource managers, legislators, and planners of land use will find considerable value in the findings. In the Lower Awash River watershed, accurate mapping of flood inundation will be helpful in identifying high-risk locations, directing land-use planning decisions, and promoting sustainable development practices.

This study will support efforts for adapting to climate change in the context of possible implications of climate change on hydrological systems and precipitation patterns. It will be crucial to comprehend future flood evolution in order to build resilient infrastructure and modify land-use practices in response to shifting environmental factors. The Lower Awash River basin's integration of Google Earth Engine and hydrodynamic modeling is a scientific first. The project will contribute to the corpus of knowledge in hydrology, remote sensing, and

geospatial analysis by demonstrating the usefulness and effectiveness of cutting-edge technology in tackling pressing issues in the real world.

1.6 Scope of the Study

The study's scope is restricted to specific geographical and thematic domains. Due to time and resource constraints, the study's focus is restricted to the lower Awash River basin, even though seasonal flooding has an impact on the top, middle, and lower sub-basins of the Awash Sub-basin. The need for extensive data and funding for on-site data collection prevented the flood risk and damage assessment from being carried out. For the same reason, the dimensions of the structures on the floodplain, Manning's roughness assessment, and the input geometric data were not obtained through a field survey; rather, these data were taken from secondary data sources and currently available remote sensing (RS) products.

1.7 Thesis Organization

The present thesis is structured into five sections. The backdrop, the issue statement, the study's purpose, the research questions, the study's importance, and its scope are all included in the first chapter, which serves as the introduction. The literature review, which covers articles and other relevant materials produced on numerous theme areas to thoroughly address the study's topic and make it simply understandable, is the second chapter. The review describes various names and terminology related to floods, as well as flood hazards, vulnerability, and risk mapping and their evaluation, methods for estimating the magnitude of floods, analysis of flood frequency, probability distributions, regionalization, 1D and 2D hydraulic models, Google Earth Engine flood mapping, and flood modeling. Finally, the review examines studies on mapping and assessment of flood hazards. The third chapter's materials and methods section covered the approach used from the phase of data collecting to the phase of mapping and assessing flood hazards. The methodology includes a description of the research region, statistical tests, flood frequency analysis, HEC-RAS execution, GEE flood hazard methodologies, and flood hazard mapping and evaluation. Details of the preparation and execution phases are also included in the middle of the methodology. The study's findings are presented in the fourth chapter along with a discussion of them. Ultimately, the fifth chapter presents conclusion and recommendations based on the analysis of the study's data and draws inferences from the outcomes analyzed.

2 LITERATURE REVIEW

2.1 The Concept of Flood

A flood is a river's abnormally high stage, usually the point at which the river breaches its banks and submerges the nearby area. It is common knowledge that floods may inflict significant harm to people and property, as well as generate economic losses by disrupting economic activities. The annual cost of flood prediction and control is in the thousands of crores of rupees. The hydrograph of extreme floods and phases correlated with flood peaks provide valuable information for hydrologic design. Moreover, of all the aspects of the flood hydrograph, the flood peak is perhaps the most important and commonly used statistic (Subramanya, 2008).

The location of flood peaks in a stream varies annually, and their combined magnitudes create a hydrologic series that makes it possible to assign a frequency to a particular flood-peak value. An individual can assign a frequency to a particular flood-peak value by utilizing the hydrologic series formed by the amplitude of the flood peaks at a certain location in a stream, which varies annually. The peak flow that can be anticipated with a given frequency (let's say once every 100 years) is crucial for designing nearly all hydraulic systems to appropriately proportion the structure to accommodate its influence. A streaming site's flood-peak values are required for many different applications, including the design of bridges, culvert waterways, dam spillways, and the assessment of scour at a hydraulic structure. Two features define a flood: (i) the peak's size, or the maximum discharge rate, and (ii) the peak's stage, or the elevation of the water surface at the peak flow. Peak flow rate determines the design of (i) dam and barrage spillways and (ii) bridge and culvert waterway capacities. This scene is really important (Subramanya, 2008).

2.2 Hydrological Data Quality Assessment

2.2.1 Filling of Missed Hydrological Data

Like nearly every other scientific discipline, hydrology has profited greatly from the remarkable advancements in scientific apparatus designed to gather extended data sets and the rise in accessible processing power and storage capacity in recent years. These time series are the foundation for numerous model applications and statistical analyses, such as extreme value analysis. As such, the accuracy and comprehensiveness of these time series are crucial. Therefore, preprocessing raw data sets by completing data gaps is essential. In general, missing data lowers the precision and power of statistical research techniques (Gao et al., 2018).

Techniques For Handling Missed Data

Listwise and pairwise deletion

Listwise deletion is the process of removing all observations for which there is missing data in one or more variables. Convenience is listwise deletion's main advantage. This strategy has several problems since eliminating observations to deal with insufficient data will always result in a smaller sample size (Gao et al., 2018).

Single-imputation methods

Before the data are analyzed, single-imputation techniques produce a single replacement for each missing value with an appropriate value.

Arithmetic mean and median imputation

By using the arithmetic mean of the observed values for the same variable, arithmetic mean imputation fills in any missing values in the variable. By using the median of the observed values for the same variable, median imputation fills in the missing values. Given how easily a comprehensive dataset can be generated, both ways are incredibly convenient. When the underlying variable has a skewed distribution rather than a symmetric distribution, median imputation is the better option. These methods, however, skew the final parameter estimations even in cases when the strong MCAR assumption is true. They reduce, for example, the variance and the standard deviation of estimates derived from mean-imputed variable analyses. The imputed values are the same and at the center of the estimations, which accounts for the decrease in the standard deviation of estimates (Gao et al., 2018).

Multiple imputation

More advanced techniques have been created to lessen the detrimental effects of regression imputation as previously indicated. The main idea is to substitute two or more reasonable values, which reflect a range of alternatives, for each missing piece. These are hence referred to as multiple imputation techniques. Multiple imputations have been possible due to recent improvements in computing power as pertinent methods are increasingly included in common statistical software packages. The primary benefit of multiple imputation is that, because it accounts for missing data uncertainty, conclusions made about statistics like correlations and errors are not overstated. Nevertheless, MI has certain drawbacks. The primary drawback of MI is that it necessitates greater computational work because of both the imputation and the ensuing (Gao et al., 2018).

Multivariate imputation, on the other hand, considers the entire set of available features to estimate missing values. More complex imputations result from modeling each feature with missing values

as a function of other features. It is an effective method for dealing with incomplete data in hydrological research.

2.2.2 Data Homogeneity Analysis

Homogeneity testing is essential for climatological research to accurately depict the fluctuations in weather and climate. Climate data can be inhomogeneous for several causes, such as human error, changes in the instrument's surrounding surroundings, and technical errors. If the homogeneity is not looked at prior to trend analysis, the results will display inaccurate trends. Relative homogeneity tests were performed in this work by calculating the ratio of the observed series to the reference series and utilizing the Anclim software application to create a reference series. Individual station records were subjected to absolute homogeneity testing (Patakamuri et al., 2020). Homogeneity tests can be conducted using a variety of techniques, including the Von Neumann ratio (VNR), Pettitt's test, the standard normal homogeneity test (SNHT), and the Buishand range test (BRT) (Daba et al., 2020; Patakamuri et al., 2020).

2.3 Estimation of Flood Quantiles

Floods are common, and planning hydraulic structures and flood control systems requires anticipating peak discharge at various frequencies. As a result, forecasting the peak flood for a longer return time becomes challenging and even more challenging in an unmonitored area. Frequency distributions such as Log Pearson Type III (LP3) and Gumbel Extreme Value Type I (EV1) were frequently employed to estimate peak discharge at the place where discharge is monitored. Higher order distributions, such as Generalized Extreme Value (GEV), Generalized Pareto (GPA), Generalized Logistic (GLO), Log Normal (LN3), and Pearson Type III (PE3), were used in the RFFA scenario in addition to the two distributions previously described (Drissia et al., 2019).

Among the various techniques available for estimating the distribution's parameters, the maximum likelihood (ML) approach and the method of moments (MoM) were extensively employed. GPA was discovered to be the best-suited distribution in a study using the machine learning method to estimate parameters in the Abiod watershed in Algeria (Benameur et al., 2017). The best-fit distribution for each site was identified among the distributions using Chi-square, the Anderson-Darling Test, Kolmogorov-Smirnov goodness-of-fit tests, mean absolute relative deviation (ARD), and mean squared relative deviation (MSD) (Heidarpour et al., 2017; Kamal et al., 2017).

In flood frequency studies, particularly RFFA, the creation of L moments by Hosking and Wallis (1993) marked a turning point, even though MoM was utilized extensively in earlier research for parameter estimates. A linear combination of probability-weighted moments is called L moments, and it is a robust technique for RFFA. It is noted that L moments as metrics of distributional form are easier to interpret. This technique was created for RFFA, but it was also used to estimate the peak discharge for various frequencies at the location (Drissia et al., 2019).

L-moments

L-moments, which are the linear combination of order statistics, are suitable for FFA, including appropriation recognition and parameter calculation. They are strong against anomalies and unbiased for small trials (Hosking, 1990).

When estimating hydrological data and distribution characteristics, the L-moment offers an acceptable and effective estimate. The L-moment approach has some practical advantages over other ordinary moments of probability distributions, including greater dispersion, less biased skewness and kurtosis, and better functioning with tiny data samples (Kar et al., 2017).

Common L-moment ratios include:
L-skewness (τ3/τ2) The distribution's skewness is gauged by this ratio. Left skewness is shown by negative values, and right skewness is indicated by positive values. In hydrology, it helps determine whether the distribution is skewed towards high or low values.
L-kurtosis (τ4/τ2) The kurtosis, or peakedness, of the distribution is measured by this ratio. Lower values show flatter distribution and lighter tails, whereas higher values show heavier tails and a more peaked distribution.
After analyzing the goodness of fit using Kolmogorov-Smirnov and L-moment ratios, the following table summarizes the best-fitted distribution for each station.

Goodness-of-fit (GOF) tests

The observed data are tested for distributional consistency using goodness-of-fit tests.

Chi-Square Test:

A statistical technique called the chi-square test is used to assess whether observed and predicted frequencies in categorical data differ significantly from one another. By segmenting the temperature range into bins and contrasting the observed frequencies of temperature values

in each bin with the expected frequencies based on the fitted pdf, the chi-square test can be used in the context of fitting pdfs to temperature data. A chi-square distribution is used to compute the chi-square statistic and evaluate its significance. A low p-value suggests that the selected pdf might not accurately represent the temperature data since it shows a poor fit between the observed and expected frequencies (Haddad, 2021).

Kolmogorov-Smirnov Test:

A non-parametric test called the Kolmogorov-Smirnov (KS) test is used to compare a sample's cumulative distribution function (or CDF) to a reference CDF. The KS test is used to evaluate how well pdfs fit temperature data by contrasting the CDF of the fitted pdf with the empirical CDF that was created using the observed temperature data. The greatest vertical distance between the two CDFs is represented by the KS statistic, which is computed. The Kolmogorov distribution's critical values are used to assess the KS statistic's importance. A lower p-value suggests a poor fit since it shows a considerable divergence between the fitted pdf and the observed data (Haddad, 2021).

Anderson-Darling Test:

Another statistical measure for determining how well a sample fits a given distribution is the Anderson-Darling (AD) test. Though it gives the distribution's tails more weight, it is comparable to the KS test. By computing the AD statistic, the AD test assesses the difference between the fitted pdf and the observed data. Critical values unique to the distribution under test are used to calculate the significance of the AD statistic. A poor match between the selected pdf and the observed data is indicated if the p-value is less than a predetermined threshold (Haddad, 2021).

2.4 Hydrodynamic model

2.4.1 Hydraulic Modeling (HEC-RAS)

The integrated software system HEC-RAS is intended for interactive use in a multitasking environment. The system includes the following components: graphics, mapping, reporting tools, independent analysis components, data management and storage features, and GUI. The river analysis components of the HEC-RAS system include one-dimensional and/or two-dimensional unsteady flow simulation, one-dimensional steady flow water surface profile computations, quasi-unsteady or fully unsteady flow movable boundary sediment transport computations (1D and 2D), and one-dimensional water quality analysis. The fact that the four

components share the same geometric data structure and hydraulic and geometric computing methods is one of their key features. The system has extra hydraulic design elements that can be used after the water surface profiles are calculated, in addition to the four components for river analysis. Another feature of HEC-RAS is HEC-RAS Mapper, a powerful mapping and data integration tool. One- and two-dimensional hydraulic calculations for a vast network of man-made and natural waterways, overbank/floodplain areas, levee-protected areas, etc. can be performed using HEC-RAS. The main responsibilities of HEC-RAS are described here (Brunner, 2016).

2.4.2 HEC-RAS-One Dimensional (1D) Model

HEC-RAS uses both steady and unsteady flow analysis to determine the flood plain and calculate the water surface profile. Unsteady flow routing is used to solve the 1D Saint-Venant problem, which is made up of the momentum equation (18) and continuity equation (17), respectively (Ghimire et al., 2022). These equations are as follows:

$$\frac{\partial A}{\partial \mathrm{t}} + \frac{\partial \mathrm{Q}}{\partial \mathrm{x}} = 0 \qquad (1)$$

$$\frac{\partial \mathrm{Q}}{\partial \mathrm{t}} + \frac{\left(\frac{Q^2}{A}\right)}{\partial \mathrm{x}} + gA\frac{\partial \mathrm{H}}{\partial \mathrm{x}} + gA(S0\ Sf) = 0 \qquad (2)$$

Kinematic Wave (Steady Uniform Flow)

Diffusion Wave (Steady non-uniform flow)

Dynamic Wave (Unsteady non-uniform flow)

where x is the measured distance in the channel's direction, g is the gravitational acceleration, t is time, Q is water flow, and A is the cross-section area. H is the water level height above the datum. The energy slope is represented by Sf, while the river bed's slope is S0.

Using an iterative standard step approach between the two successive cross-sections, 1D constant flow solves the energy equation to get the water surface elevation for slowly variable water profiles (Brunner, 2016).

$$\mathrm{Z1} + \mathrm{Y1} + \frac{\alpha 1 V1\hat{}2}{2\mathrm{g}} = \mathrm{Z2} + \mathrm{Y2} + \frac{\alpha 2 V2\hat{}2}{2\mathrm{g}} + \mathrm{he} \qquad (3)$$

Z1 and Z2 denote the elevations in Section 1 and Section 2, respectively, and Y1 and Y2 represent the water heights in Section 1 and Section 2, respectively. The velocity weighting

coefficients in Section 1 and Section 2 are represented by α1 and α2, and the variables g and he represent the gravitational acceleration and energy loss between the upstream and downstream cross-sections, respectively.

2.4.3 HEC-RAS Two-Dimensional Model (2D Model)

Either the entire Saint-Venant equation or the diffusion wave equation are applied in the 2D model. In contrast to the 2D diffusion-wave equation, which solves issues more quickly and stably, the 2D Saint-Venant equation requires more processing power to handle specific difficulties. Equation 4 (Courant condition) for the Saint-Venant equation (full momentum) and Equation 5 for the diffusion-wave equation specify the time step for executing the model.

$$C = \frac{V\Delta T}{\Delta X} \leq 1 \text{ (with a max C = 3)} \quad (4)$$

$$C = \frac{V\Delta T}{\Delta X} \leq 2 \text{ (with a max C = 5)} \quad (5)$$

where V is the flood wave celerity, C is the Courant Number, ΔX is the average cell size, and ΔT is the computing time step. The 2D unsteady flow equation is solved implicitly using a finite volume methodology. When compared to conventional finite element techniques, this strategy allows for wider time intervals than the explicit method, improving the model's stability and robustness (Brunner, 2016). The following equations illustrate how the unsteady flow routing solves the continuity and momentum equations in space and time.

$$\frac{\partial H}{\partial \mathrm{t}} + \frac{\partial (hu)}{\partial \mathrm{x}} + \frac{\partial (hv)}{\partial \mathrm{y}} + q = 0 \quad (6)$$

$$\frac{\partial u}{\partial \mathrm{t}} + \frac{\mathrm{u}\,\partial u}{\partial \mathrm{x}} + \frac{\mathrm{v}\,\partial v}{\partial \mathrm{y}} = -g\frac{\partial H}{\partial \mathrm{x}} + vt\left(\frac{\partial^2 u}{\partial \mathrm{x}^2} + \frac{\partial^2 u}{\partial \mathrm{y}^2}\right) - cf.u + fv \quad (7)$$

$$\frac{\partial u}{\partial \mathrm{t}} + \frac{\mathrm{u}\,\partial v}{\partial \mathrm{x}} + \frac{\mathrm{v}\,\partial v}{\partial \mathrm{y}} = -g\frac{\partial}{\partial \mathrm{x}} + vt\left(\frac{\partial^2 v}{\partial \mathrm{x}^2} + \frac{\partial^2 v}{\partial \mathrm{y}^2}\right) - cf.v + fu \quad (8)$$

The variables in this equation are time (t), velocity components (u, v), x- and y-direction (h(x,y,t)), total head (H), source (q) of the flux term (g), gravitational acceleration (g), horizontal eddy velocity (vt), bottom friction coefficient (cf), hydraulic radius (R), and Coriolis coefficient (f). Acceleration is represented on the left side of the equations, while forces acting on the fluid from the inside or outside are represented on the right side. The documentation

manual contains further information regarding the theoretical foundation of HEC-RAS (Brunner, 2016).

The surface flow is regulated by the 2D Saint-Venant equations. By using a depth averaging technique, these equations are derived from the continuity and momentum equations. The hydrostatic pressure distribution and small channel slope are the fundamental presumptions made when creating 2D SV equations. The following are the surface flow regulating equations (Kamboh et al., 2016).

2.5 Flood Inundation Mapping

Hazard mapping and inundation prediction are the first steps in flood mitigation and adaptation. It is used to mark areas that, in the case of significant precipitation, may flood (Erena et al., 2018). Using a hydraulic model and all available primary and secondary data, flood inundation maps are created following the determination of the design floods. Hydrodynamic models like FLUCOMP, ISIS, ONDA, MIKE11, SOBEK, Delft3D, and HEC-RAS are commonly employed when mapping flood inundation at the watershed level (Baky et al., 2019).

Due to extensive agricultural practices and inadequate land use management implemented over a long period, the whole Awash River basin was experiencing frequent flooding. For instance, one of the greatest flood incidents to ever occur in Ethiopia's lower Awash River basin was the abrupt flood that overflowed the town of Dire Dawa at midnight on August 6, 2006 (Namara et al., 2022).

The study (Papaioannou et al., 2016) investigated the sensitivity of flood inundation mapping to the spatial resolution of riverine data and the choice of hydraulic modeling approach. The researchers used four types of riverine data - terrestrial laser scanner (TLS) data, topographic land survey data, and digitized contours from 1:5000 scale maps - along with various hydraulic modeling techniques, including 1D models (HEC-RAS, MIKE 11), 2D models (MIKE 21, MIKE 21 FM), and coupled 1D/2D models (MIKE FLOOD). The study area was the lower Xerias River basin in Volos, Greece, which experienced a major flash flood event in 2006. Flood inundation maps were generated for each data/model combination and compared to the observed 2006 flood extent using contingency tables. The results showed the sensitivity of flood mapping to both DEM spatial resolution and the choice of hydraulic modeling approach.

The HEC-RAS v5 model was calibrated and validated using flood events from 2010 and 2015, respectively. The Manning's roughness coefficient (n) values were optimized through the

simulation process. Satellite imagery from Landsat 5/8 and MODIS were used to delineate water bodies using various water indices (NDWI, MNDWI1, MNDWI2). The satellite-derived flood extents were used to assess the accuracy of the HEC-RAS simulations. The optimized n values for rivers and floodplains were 0.055 and 0.06 respectively, which showed good agreement between simulated and observed flood extents. The integrated HEC-RAS and satellite imagery approach can be further used for early flood warning in the central part of the Indus River basin. In summary, the study demonstrates the potential of coupling hydrodynamic modeling with remote sensing data to improve flood monitoring and early warning capabilities in a data-scarce region like the Indus River basin in Pakistan (Afzal et al., 2022).

The paper (Tansar et al., 2020) presents a flood inundation modeling and hazard assessment study in the Lower Ping River Basin in Thailand. The authors state that floods are common and devastating natural disasters globally, with increasing intensity and frequency due to climate change and human activities. Flood risk assessment and management are crucial initial steps to delineate inundation extents and identify flood-prone areas. Numerical modeling approaches have become popular for evaluating flood mitigation measures, as in-situ observations and remote sensing data have limitations. The background information provided outlines the evolution of flood modeling techniques and their advantages/limitations. 1D models can simulate flow within the channel but fail to capture floodplain dynamics, while 2D models can simulate floodplain flooding but require higher computational resources and struggle to link river overflow with floodplain inundation. Coupled 1D-2D models like MIKE FLOOD can dynamically link the river and floodplain to provide more comprehensive flood simulations. The study utilized a coupled 1D-2D hydrodynamic modeling approach using MIKE FLOOD to simulate flooding under different return periods (2-, 5-, 10-, 25-, 50-, and 100-year) in the Lower Ping River Basin. The 1D hydrodynamic model was calibrated using observed discharge and water level data, while the 2D model was calibrated using observed flood maps. Flood hazard levels were categorized based on critical flood depths, with the results showing that 28.8% of the basin area was flooded during the 100-year event. The maximum flood inundation was observed in Kamphaengphet and Nakhon Sawan provinces, with over 40% of the sub-districts in these areas flooded.

2.6 Flood Hazard Assessment

The primary characteristics that contribute to flooding that are included in the assessment of flood hazards are elevation, land use, drainage density, average rainfall, slope, and soil type (Getahun YS, 2015). Based on their degree of influence on the outcome, the sub-factors and map layer were ranked and assigned weights using the Analytic Hierarchy Process (AHP), a multi-criteria decision-making technique. Following a weighted overlay analysis of these layers, a final map was created and classified according to how the flood hazard model indicated each layer's impact on flood danger (Hagos et al., 2022).

Flood hazard = $\sum W_i X_i$ Where Wi = weight of factor i; Xi = criterion score of factors i.

In the study conducted by (Farooq et al., 2019), Flood hazards were categorized into different zones based on simulated flood depth and extent. High and very high flood hazard zones were found in the central and lower reaches of the river. These areas are characterized by flat land, low slopes, and low drainage density.

The study, (Vojtek & Vojteková, 2016) presented a case study on assessing flood hazard and flood risk at the local spatial scale using GIS, remote sensing, and hydraulic modeling. In determining flood hazard, the researchers estimated maximum flood discharges and conducted 1D hydraulic modeling to obtain water depth and flow velocity data. To define flood risk, they followed a comprehensive approach - first determining flood intensity from the water depth and velocity, then classifying flood hazard into low/medium/high categories, defining vulnerability for different land use classes, and finally combining hazard and vulnerability to determine overall flood risk. The authors note that while traditional flood protection measures remain important, flood prevention and risk management are playing an increasing role. The study highlights some of the key challenges in this process, including accurately estimating maximum flood discharges, dealing with uncertainties in statistical methods, and effectively integrating hazard and vulnerability assessments.

Another study (Farooq et al., 2019) presented a comprehensive flood hazard assessment and mapping study for a 60 km stretch of the Swat River in northern Pakistan. The researchers utilized the HEC-RAS 2D hydrodynamic model in combination with high-resolution 12 m WorldDEM data to simulate the flood dynamics. The model was calibrated and validated using the historic 2010 flood event, with inputs including Manning's roughness, flood stage, and

satellite-derived flood extent. An important aspect of the study was the sensitivity analysis performed to assess the

impact of using different DEM datasets, including 12 m WorldDEM, 30 m SRTM, 30 m ALOS, and 30 m ASTER, on the simulated flood depths. The researchers then generated synthetic flood hydrographs for return periods of 2, 5, 10, 25, 50, and 100 years, and used the 2D model to simulate the corresponding flood extents. Based on the 12 m WorldDEM simulations, the study produced comprehensive flood hazard maps for the study area. Additionally, the researchers analyzed the exposure of different land cover classes, such as agriculture and orchards, to the simulated flood events.

The paper (Baky et al., 2019) presented a new approach to assessing flood risk by integrating GIS, hydraulic modeling, and field information. The key premise is that while flood hazard may be the same for a given area, the risk can differ depending on the vulnerability. The study aims to address this critical issue in flood risk assessment by evaluating flood risk from both flood hazard and vulnerability indices. The methodology involves several steps. First, a 2D flood flow simulation using the Delft3D model is performed to compute floodplain inundation depths for hazard assessment. For vulnerability assessment, the researchers identify key elements at risk and assess flood damage functions. Finally, flood risk is assessed by combining the replacement values of the elements and using the depth-damage functions. The study findings are noteworthy. It reveals that areas with different levels of flood risk do not always increase with the increase in the return period of flood, though inundated areas with different flood depths always increase with higher return periods. This successfully addresses the limitation of previous studies that assumed vulnerability to be proportional to population density, which does not accurately represent flood damage. The paper highlights the importance of considering both hazard and vulnerability components to accurately assess flood risk. This comprehensive methodology, which combines hydrodynamic modeling, elements at risk, and depth-damage functions, can inform effective flood mitigation and management strategies. Overall, the study presents a robust approach to flood risk assessment that addresses a key shortcoming in previous flood risk studies.

2.7 Flood Risk Assessment

Flood risk mapping is the process of charting places that are vulnerable to floods, inundation zones, and dangerous environments and buildings as a result of a flooding incident. This might involve estimating and drawing the boundaries of flood inundation zones, as well as the depths of floods and the frequency at which popular foods reoccur (Edamo et al., 2023). Sensitivity to the likelihood of flooding or other potential damage was the main factor used to determine which risk categories to allocate to functional area classes. Therefore, locations with less risk of flooding are regarded as model areas. The aforementioned areas comprise residential zones, civil engineering facilities, agricultural and forestry areas, technical facilities, and transportation facility locations. Moreover, there are places where it's okay to take a small chance, such local green spaces and public parks. Agricultural areas, forests, green spaces in landscapes, and locations with streams and reservoirs are examples of high-acceptable risk settings. Accurate geographic information of high-risk areas and sensitive places is essential for disaster preparedness. The process of identifying regions that are susceptible to flooding catastrophes in order to reduce flood risk must include mapping flood vulnerability (Edamo et al., 2023).

2.8 Application of Google Earth Engine Cloud Platform

2.8.1 Overview of Google Earth Engine (GEE) Platform

In order to address massive data difficulties and improve satellite image processing for wide-ranging applications, Google Earth Engine (GEE) was launched as a web-based platform in 2010. As demonstrated, Google Earth Engine (GEE) is a web-based platform that offers a multitude of globally available, analysis-ready earth observation datasets along with cloud computing infrastructure that includes the reliable methods needed for analysis on a single platform. This can be acquired through an online application programming interface (API) and a web-based interactive development environment (IDE) that speed up result visualization and prototyping. The cloud computing architecture of Google Earth Engine allows real-time access, manipulation, and analysis of large amounts of geographic data. This includes a vast public data archive with petabytes of geospatial data from various sensors and satellite imagery. Moreover, fresh photos are published every day in the publicly available data database, which is free to use for anybody. This is an easy-to-use platform that has gained prominence in the remote sensing community recently and has helped numerous local, regional, and international

earth science investigations. GEE thus provides prospects and applications at many spatial and temporal dimensions that benefit human civilization and the environment (Ghosh et al., 2022).

Recently, because machine learning-based simulations can save time and don't require specialized equipment, researchers have concentrated on them. A terminal shows the outcome. The Google Earth Engine platform offers an interface for working with JavaScript object notation (JSON). GEE has over forty years of data that are available and archived thanks to the scripts on the platform. In addition to environmental mapping, GEE is highly regarded for its contributions to air pollution, atmospheric analysis, hazard management, and NDVI (normalized difference vegetation index). Thanks to a modern approach, the study shows how to use GEE to map floods in many parts (Trambadia et al., 2023).

A). Data catalog in Google Earth Engine (GEE)

The Google Earth Engine (GEE) data catalog includes information on meteorological forecasts, environmental variables, topography, and socioeconomic datasets at the international, national, and local levels. These data, which span both optical and non-optical wavelengths, are gathered from various satellite and aerial imaging systems. The bulk of the catalog consists of Earth observation remote sensing pictures, such as the whole Landsat dataset collection, Sentinel satellite images, MODIS images, and other relevant datasets used in various applications. Additionally, MODIS images are included in Google Earth Engine and present a wealth of opportunities for regional and global real-time ground surface mapping (GEE).

B). Function of Google Earth Engine (GEE)

The JavaScript code editor works effectively for large-scale operational processing in this setting. There are more than 800 prebuilt functions in the GEE earth engine library. The API reference documentation found on the Doc page helps users learn about all of the library's functions. This platform has many built-in algorithms, like classification algorithms, to analyze data at the planetary size and help scientists create their algorithms more effectively and with less work. Once an algorithm is built, users can quickly create systematic data products or arrange interactive applications using resources from earth engine data. Many image classification techniques are available on the GEE platform, and they can be used on an individual image or a set of images. Supervised and unsupervised categorization is supported by the Google Earth Engine library, which includes sophisticated machine learning algorithms

in addition to built-in operations. Pixels were assigned to one of many user-specified class groupings using unsupervised techniques (Ghosh et al., 2022).

2.9 Studies Held on Awash Basin

Many research on flood hazards and risk mapping has been conducted in the Awash River basin, focusing on the upper sub-basin. Numerous methodologies have been employed in these studies, such as the topographic wetness index (TWI) and topographic position index (TPI), multi-criteria evaluation, HEC-HMS and HEC-RAS with HEC-GEORAS and GIS, Analytic Hierarchy Process (AHP) and GIS, and Geospatial Stream Flow Model (GeoSFM) in the Upper Awash River Basin (UARB).

Nevertheless, prior to conducting this study, all I could find were two journal articles and one master's thesis on MARB (Getaneh, 2023) using the HEC-RAS 1D model; (Fenglin et al., 2023) employing GIS and exploratory regression analysis; (Koriche & Rientjes, 2016) satellite-based flood early warning in the Awash River Basin using the Standard Precipitation Index (SPI) and Topographic Wetness Index (TWI); (Getaneh, 2023) used a combination of tools (HEC-RAS, ArcGIS, and HEC-GeoRAS) to generate flood 1D hazard, vulnerability, and risk maps for; and one journal article for LARB (Wondim, 2016) that assessed flood hazard and risk in the Lower Awash sub-basin. Though they have been conducted in the upper, middle, and lower Awash sub-basins, the aforementioned research solely addresses 1D flood modeling. The one-dimensional constant flow assumption of the HEC-RAS model flow is not always true in natural river channels since natural river courses are turbulent. It is wise to consider unstable flow simulation models in two dimensions because of this. Furthermore, no research has been conducted in Ethiopia that makes use of the Google Earth engine platform for mapping flood inundation and risk assessment. Additionally, as everyone is aware, our nation has data limitations. Google Earth Engine (GEE) is an efficient and potent tool for mapping flood inundation. In order to analyze big datasets fast and effectively, it provides open-source data availability, scalability, cloud-based processing, and machine learning methods. Change detection, flood risk assessment, mapping flood extent, early warning systems, and post-flood damage assessment are all possible using GEE. We may therefore draw the conclusion that the risk and danger of river floods in Ethiopia and LARB have not been fully examined. Thus, mapping flood hazards, vulnerabilities, and dangers over the whole Awash River in LARB and evaluating them is the aim of this work.

3 MATERIALS AND METHODS

3.1 Study Area Description

3.1.1 Location

Based on variables pertaining to its climate, physical characteristics, socioeconomic standing, agricultural methods, and water resources, the Awash River Basin is split into the Upper Awash, Middle, and Lower Basins (Duguma et al., 2021). Within the Awash Basin, the Lower Awash Sub-basin is situated in the Afar National Regional State (ANRS). Its coordinates are latitude 100 33' to 120 15' N and longitude 390 51' to 410 49' E. Its borders are shared by the Amhara area to the west, the Teru sub-basin to the north, the middle Awash Sub-basin to the south, and the Republic of Djibouti to the east. The sub-basin is composed of nine districts: Zone 2-3, which include Mille, Dubti, Aysayta, Afambo, Chifra, and Ada'ar Woredas; Zone 4-Ewa woreda; and Zone 5-Telalak and Dewe Woredas (Wondim, 2016).

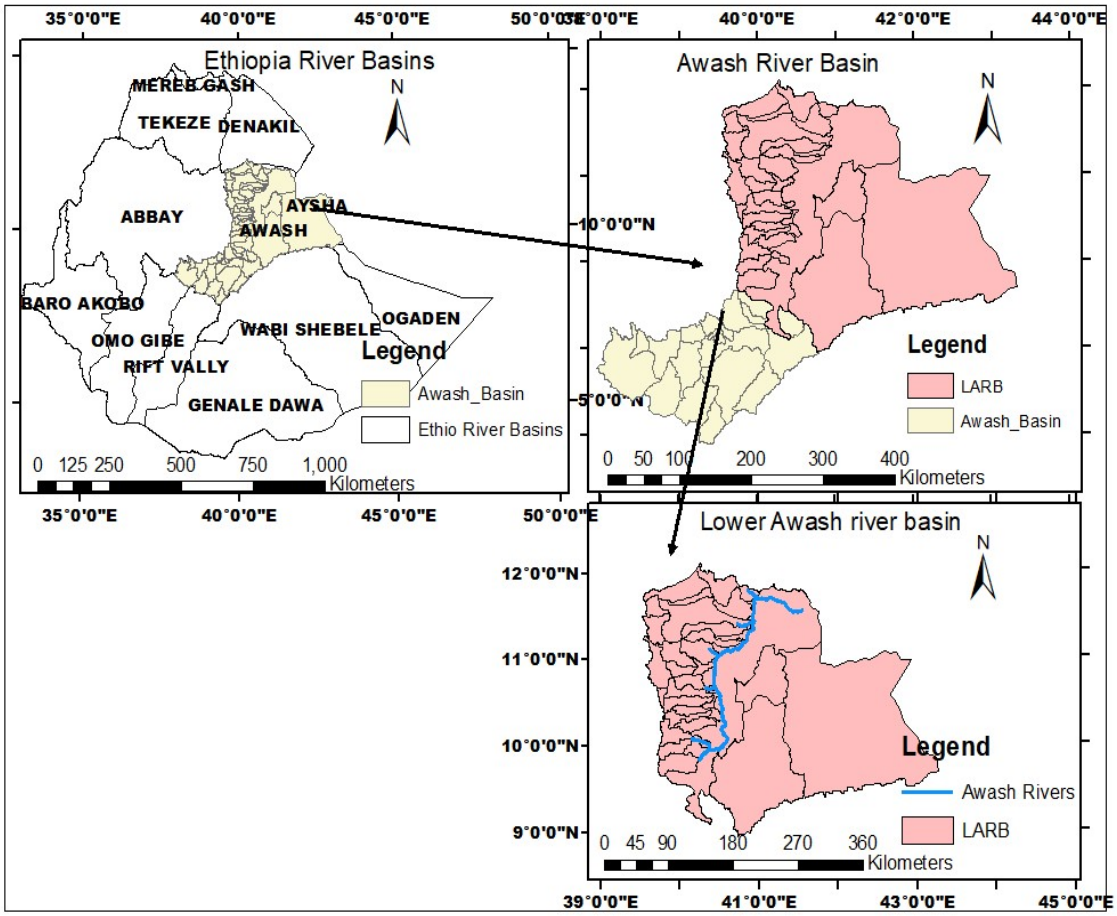

Figure 3. 1 Location Map of the Study Area.

3.1.2 Climate

The rainfall distribution is generally dual-mode in the LARB. The region has minimal rainfall in May and June and November and January, according to the sub-basins four-gauge stations' accessible rainfall data (Figure 3.2). The official rainy season runs from July to September.

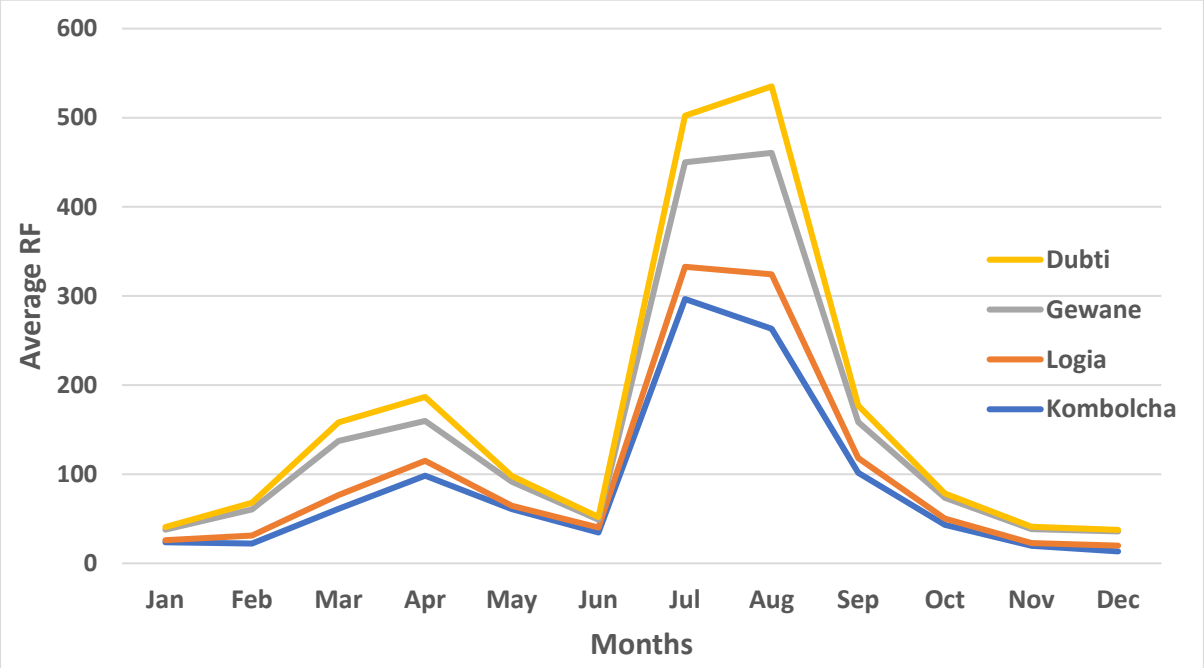

Figure 3. 2 Monthly average rainfall distribution of the station

3.1.3 Soil

In the study region, there are 22 different types of soil based on the MOA classification.

The dominant soil type is calcaric flubisols, which covers an area of 422,133.9 ha. This is a type of alluvial soil formed by the deposition of river sediments. The next largest soil type is eutric regosols, covering an area of 2,089,887.496 ha. Regosols are a type of undeveloped soil found in arid and semi-arid regions. Chromic cambisols, a type of cambisol soil, cover an area of 157,977.2636 ha. Cambisols are soils that show minimal profile development. Eutric fluvisols, a type of alluvial soil, cover 1,117,724.063 ha. These are soils that develop in areas with frequent flooding or deposition. Chromic vertisols, which are clay-rich soils that shrink and swell with changes in moisture, cover 164,072.484 ha. Chromic luvisols, which are soils with an accumulation of clay in the subsoil, cover 102,149.7073 ha. The remaining soil types each cover smaller areas, ranging from 240 ha for orthic acrisols to 961,864.3859 ha for leptosols, which are shallow soils over hard rock.

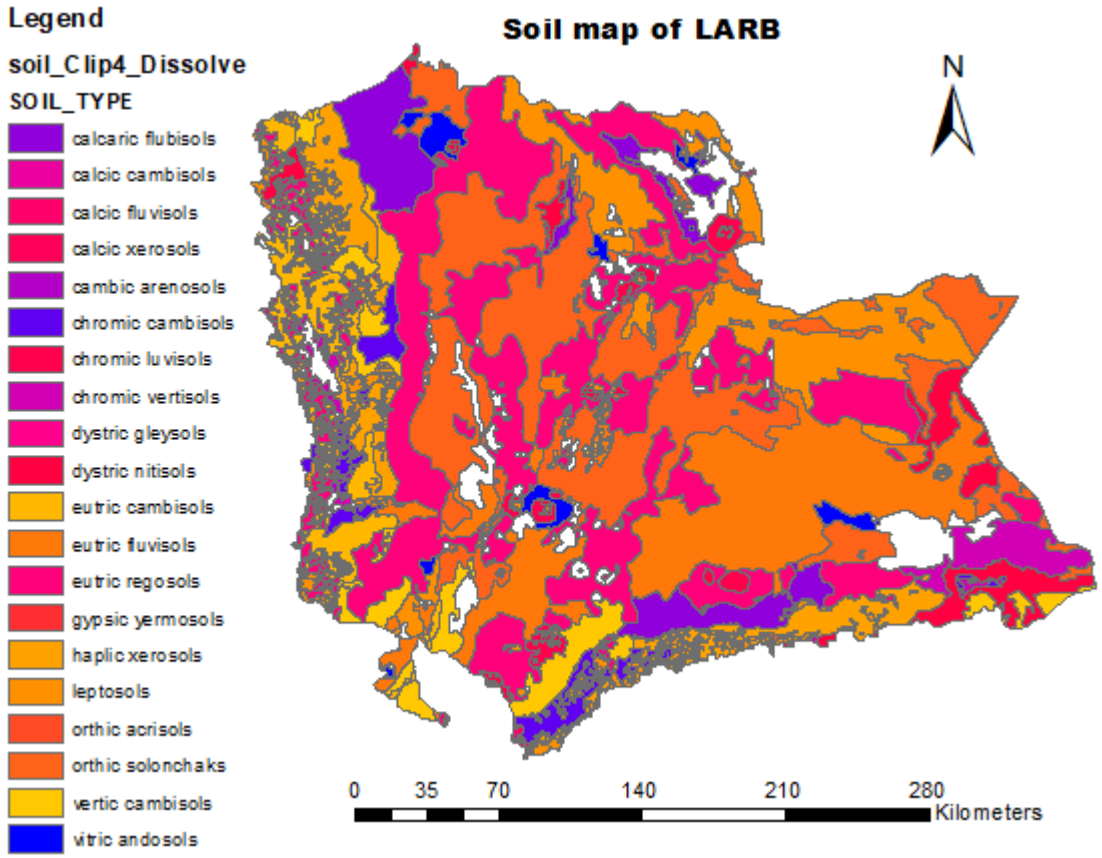

Figure 3. 3 Soil map of the study area

3.1.4 Land Use Land Cover

The largest LULC category is Range Land, which covers a total area of 6,980,900.9942 ha (6,798,127.862 ha + 182,773.1822 ha). This indicates that much of the land is used for rangeland or grazing. The second largest LULC type is Agriculture, covering an area of 765,537.9256 ha. This suggests that a substantial amount of land is dedicated to agricultural production, likely including croplands and possibly orchards or vineyards. The third largest LULC category is Bare Ground, covering 416,924.7938 ha. This could represent sparse vegetation, exposed soil, or areas undergoing development or other land use changes. Trees cover an area of 206,262.8866 ha, indicating the presence of forested or wooded areas within the region. Urban areas cover 71,986.93938 ha, representing the built-up or developed parts of the landscape. Vegetation, including grasslands, shrublands, or other non-tree vegetation, covers 28,673.62447 ha. Finally, Water bodies cover an area of 80,716.95084 ha, likely including rivers, lakes, and other surface water features.

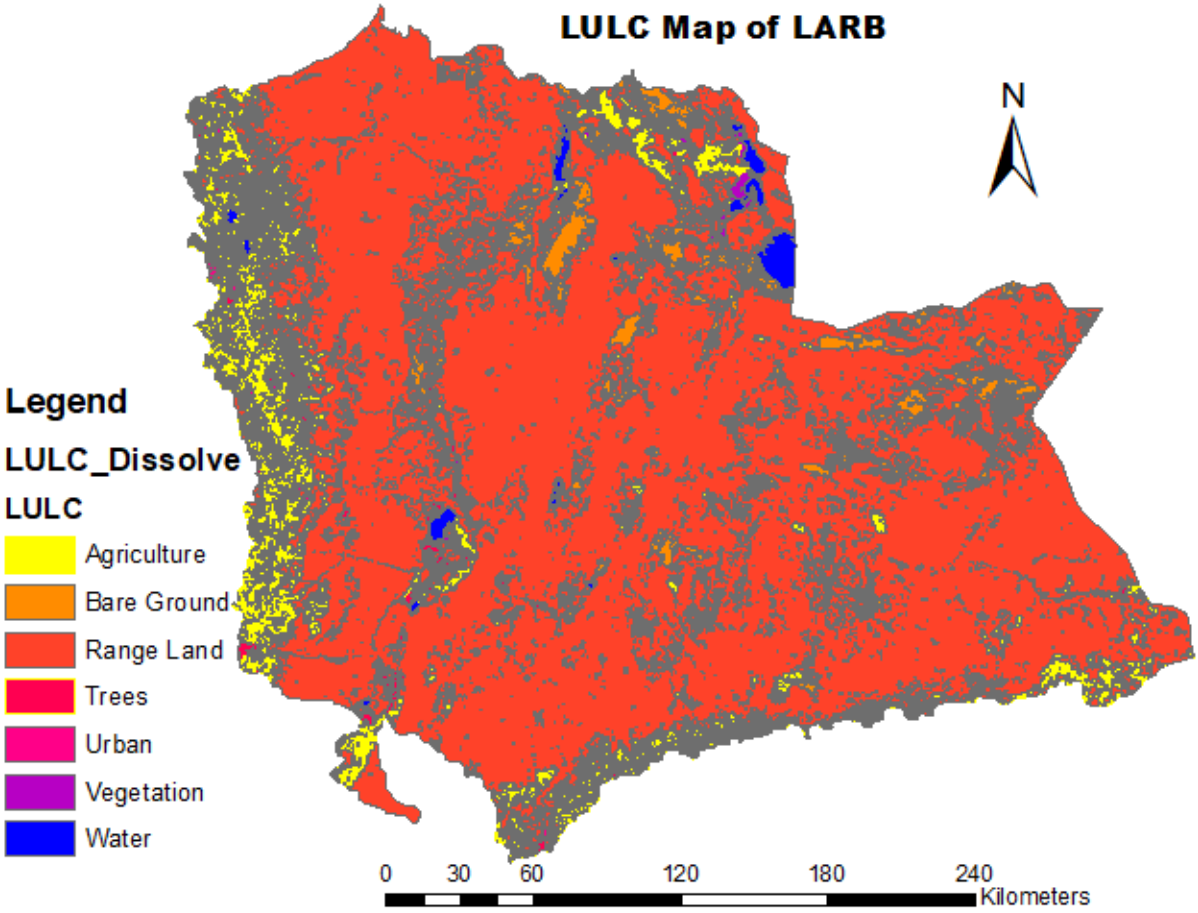

Figure 3. 4 LULC map of the study area

3.2 Datasets

For the hydraulic modeling of HEC-RAS to configure the physical parameters of the flood plain into the model, a large amount of geometric and hydrologic data is required. The genuine flood coverage area of the flood plain must be carefully transformed using topological and geometric data. Accurate mapping of flood inundation requires a high-resolution digital elevation model (DEM). In order to achieve this objective, a 12.5 m by 12.5 m high-resolution digital elevation model was acquired from the Alaska Satellite Facility.Using Arc GIS and its extension geospatial river analysis system, HEC-Geo RAS, high-resolution digital elevation modeling (DEM) was utilized to extract geometric cross-section features of rivers, including the centerline, flow route lines, bank lines, XS cut lines, and Manning's roughness coefficient (Namara et al., 2022; Tamiru & Dinka, 2021).One of the first steps in mapping flood inundation, assessing flood risk, and charting flood hazards is the determination of the extreme flood value. Flood inundation mapping, according to (Namara et al., 2022), is a process-based task that tracks the pattern of findings from an analysis of the frequency of flooding within a

certain watershed (flood plain). For the River Analysis System (RAS) to display the area of the floodplain that has been flooded, flow data (profile) is required. To accomplish these objectives, hydro-meteorological data were obtained from the Ethiopian Ministry of Water and Energy (MoWE) and the Ethiopian Meteorological Agency.

Table 3. 1 Data needed and their sources

Data needed	**Purpose**	**Sources**
Stream flow data	1D/2D simulations	Ministry of Water and Energy (MoWE)
Stream geometry	An input for HEC-RAS	Extracted from DEM
DEM 12.5m	Terrain file creation	Alaska Satellite Facility https://vertex.dac.asf.alska.edu
Historical flood Water level data	Calibration of HEC-RAS model results	Ministry of Water and Energy (MoWE)
LULC Sentinel 2 10m	Land use and Land cover classification	Copernicus RS products https://livingatlas.arcgis.com/landcoverexplorer/.
Landsat image	Pre-flood images and during-flood images for validation	Earth Explorer https://www.usgs.gov/programs/national-geospatial-program/national-map

Table 3. 2 Acquired stream flow data

SITE	**Periods**	**Length of record**	**Catchment Area (km^2)**
Borkena. COMBOLCHA	1976-2001	26	212.5
@ ROBIT VILLAGE	1987-1998	12	263
@ JEWEHA	1982-2003	22	514.4
Ataye	1985-2001	17	166.4
@ MILLE VILLAGE	1981-2008	28	4467
@ DUBTI	1972-2002	31	66308
@ TENDAHO	1969-2002	34	62088

@ LOGIA VILLAGE	1977-2008	32	3994
@ ADAITU	1999-2015	23	52836
Melka Werer	1973-2010	38	31183

Table 3. 3 Software Used in the Study

Name of Software	Purpose
HEC-RAS V 6.5	Flood inundation modeling and hazard Map Generation
QGIS 3.28.13	Overlay and Analyze HEC-RAS Results
ArcGIS 10.8	Hazard Map Analysis and HEC-RAS Result Visualization
Python (Jupyter Notebook)	Missed data filling and non-homogeneity adjustment
HEC-SSP	Statistical analyses of hydrologic data
Rainbow	Data homogeneity check

3.3 Data Quality Analysis

3.3.1 Filling of Missed Data

In hydrological research, missing data is a frequent issue that can arise from a variety of sources, including malfunctioning equipment, incorrect data entry, and malfunctioning observation stations (Gao et al., 2018).

3.3.2 Data Homogeneity Analysis

Homogeneity tests can be conducted using a variety of techniques, including the Von Neumann ratio (VNR), Pettitt's test, the standard normal homogeneity test (SNHT), and the Buishand range test (BRT). (Daba et al., 2020).

For this study, a statistical software package called RAINBOW was employed to generate the residual mass curve and compute the homogeneity statistics which uses Buishand's homogeneity test. RAINBOW provides a homogeneity test based on cumulative departures from the mean. Calculating the maximum (Q) and range (R) of the cumulative deviations from the mean allows one to evaluate the homogeneity of data in a time series. The null and alternative hypotheses were investigated with 0.1, 0.05, and 0.01 degrees of freedom represented by the 90%, 95%, and 99% confidence intervals.

3.3.3 Test for Outliers

Data points that dramatically deviate from the overall trend of the data are called outliers. Particularly for small samples, the magnitude of statistical parameters estimated from the data can be strongly impacted by the inclusion or exclusion of these outliers. If the station skew is greater than +0.4, tests looking for high outliers are given priority, and if it is less than -0.4, tests looking for low outliers are given priority. When the station skew is within ±0.4, testing for both high and low outliers should be done before deleting any outliers from the data set (Ven Chow et al., 1988).

The Grubbs and Beck (1972) test may be used to detect outliers.

$XH = exp(\bar{x}+KNs)$ (1)

$XL = exp(\bar{x}-KNs)$ (2)

Where, z and s are the mean and standard deviation of the natural logarithms of the sample, respectively

KN = -3.62201 + 6.28446N¼ - 2.491436N½ + 0.491436N¾ - 0.037911 $*$ N (3)

where KN statistic is the G-B statistic computed at 10% significant level by Grubbs and Beck (1972) for different sample sizes and significance levels.

3.4 Flood Quantile Estimation Methods

Mapping flood inundation, estimating flood risk, and displaying flood hazards depend on the extreme flood value computation. Flood inundation mapping is a process-based endeavor that tracks the trends in the results of a selected catchment's flood frequency study (flood plain). To illustrate the floodplain region that has been inundated in water, the River Analysis System (RAS) needs a flow data profile (Namara et al., 2022).

Choosing the right PDF for frequency analysis is an important step that can greatly impact the estimated peak discharge values. The authors of the study (Baky et al., 2019) examined five different PDFs: Gumbel, Pearson Type III (P3), Three-Parameter Log-Normal (LN3), Two-Parameter Log-Normal (LN2), and Log Pearson Type III (LP3) (EV1). and found that the best-fitting distribution varied for each gauge station. This makes sense considering that the catchment's characteristics, the length of the data record that is now accessible, and the anticipated return period can all affect which PDF is selected.

Understanding and managing flood risk needs an analysis of flood frequency. It comprises establishing a link between flood frequency and amplitude using statistical approaches.

Numerous probability distribution models are available for the study of flood frequency. Among the most popular models are the Gumbel distribution, the Log-Pearson Type III distribution, and the General Extreme Value distribution. The ideal model will depend on the specifics of the data and its intended application. In the study (Ukumo et al., 2022), a Gumbel distribution was used to analyze the frequency of the expected maximum stream flow.

3.4.1 Goodness of Fit Test

Chi-square test statistic

To ascertain whether a sample (observed distribution) is representative of a particular theoretical distribution, apply the chi-square test. Remember that this statistic is usually not very informative and might not be particularly strong. After computing the test statistic, a crucial value at a specified significance level is determined for the test. It is standard procedure to compare the GOF of multiple theoretical distributions using the statistical value of the test in order to assess model distributions for temperature data. The sample, or number of bins, is arranged in a frequency histogram with N class intervals for the test, which is based on binned data (Haddad, 2021).

Kolmogorov–Smirnov and Anderson–Darling test statistics

Both the KS and AD tests are used to evaluate the acceptability of a given theoretical distribution for a specific set of observed yearly maximum temperature data. When comparing the GOF of numerous theoretical distributions to the real data, the results of these tests are often used, in a fashion similar to the chi-square test, to evaluate model distributions to temperature data. KS statistics are used to compare the CDF of the empirical cumulative probability distribution with the CDF of the theoretical distribution. The largest vertical difference between the empirical and theoretical CDFs serves as the foundation for the KS test statistic (Haddad, 2021).

Expectations of specific linear combinations of order statistics are known as L-moments. They are the foundation of a general theory that encompasses the definition and summary of theoretical probability distributions, the summarization and description of observed data samples, the quantile and parameter estimation of probability distributions, and hypothesis testing for probability distributions. They can be defined as any random variable whose mean exists (Hosking, 1990).

(Hosking, 1990) was the first to introduce the L-moments approach, a suitable statistical modeling technique that makes frequency analysis and probability distribution estimates easier.

The discussion held by (Haddad, 2021), P-P plot methods (R2P-P, KS, AD): Good for the center of the distribution. AD is slightly better for tails than KS. Q-Q plot methods (R2Q-Q, $\chi 2$): Better for tails of the distribution. $\chi 2$ is less affected by single data points. KS has distribution-independent critical values.

The chi-square test statistic is given by:

$$\chi 2 = \sum_{i=1}^{N} \frac{(Oi-Ei)\text{^}2}{Ei} \quad (4)$$

where Ei represents the predicted frequency in the ith class interval and Oi represents the observed frequency. The formula for ei is F(ji) − F(ji − 1), where ji and ji represent the lower and upper bounds of the ith class interval, respectively.

The theoretical distribution's CDF and the empirical cumulative probability distribution are compared using KS statistics. The largest vertical gap between the empirical and theoretical CDFs is the basis for the KS test statistic.

The Kolmogorov–Smirnov test statistic is given by:

$$D = \max_{1 \le i \le n} \left| Fi - Fi \right| \quad (5)$$

Theory of L-moments (LM)

L-moments, which are derived from linear combinations of order statistics, are an alternative to conventional moments. Any random variable Y with a mean can have L-moments specified for it (Ul Hassan et al., 2019). The results obtained from the L-moment ratio diagrams suggest that the generalized extreme value (GEV) and normal distributions generally provide the best fit for the temperature data. However, the study also finds that other two- and three-parameter distributions can be viable fits in certain instances. The findings from the L-moment ratio diagrams are consistent with the results obtained from other approaches, including GOF statistics (Haddad, 2021). The paper emphasizes that the L-moment ratio diagram method offers a simple, effective, and efficient approach for comparing the fit of multiple pdfs across different stations. It provides valuable insights into higher-order moments (such as shape, skewness, and kurtosis) of the temperature data set. The author suggests that the L-moment ratio diagram can be used as a complementary method alongside traditional GOF criteria.

The first four L-moments in terms of the linear combination of PWM are defined as.

$\lambda 1 = \beta 0$ (6)

$\lambda 2 = 2\beta 1 - \beta 0$ (7)

$\lambda 3 = 6\beta 2 - 6\beta 1 + \beta 0$ (8)

$\lambda 4 = 20\beta 3 - 30\beta 2 + 12\beta 1 - \beta 0$ (9)

The location (mean) is represented by the first L-moment ($\lambda 1$), and the dispersion by the second L-moment. Below are the L-moment ratios as established by (Hosking, 1990).

L-Coefficient of variation ($\tau 2$) = $\lambda 2/\lambda 1$ (10)

L-Skewness ($\tau 3$) = $\lambda 3/\lambda 2$ (11)

L-Kurtosis ($\tau 4$) = $\lambda 4/\lambda 2$ (12)

For any distribution, the unbiased sample estimators of βi of the first four PWMs can be calculated in this way.

$\beta 0 = (n - 1) / n \sum (y_j / n)$ (13)

$\beta 1 = (n - 1) / n \sum (j - 1) / (n - 1)\, y_j / n$ (14)

$\beta 2 = (n - 1) / n \sum (j - 1)(j - 2) / (n - 1)(n - 2)\, y_j / n$ (15)

$\beta 3 = (n - 1) / n \sum (j - 1)(j - 2)(j - 3) / (n - 1)(n - 2)(n - 3)\, y_j / n$ (16)

Table 3. 4 L-Moments of some common distributions (Hosking, 1990)

Distribution	**F(x) or x(F)**	**L-moments**
Uniform	$x = \alpha + (\beta - \alpha)F$	$\lambda_1 = (1/2)(\alpha + \beta)$, $\lambda_2 = (1/6)(\beta - \alpha)$, $\tau_3 = 0$, $\tau_4 = 0$
Exponential	$x = \xi - \alpha \log(1 - F)$	$\lambda_1 = \xi + \alpha$, $\lambda_2 = (1/2)\alpha$, $\tau_3 = 1/2$, $\tau_4 = 1/6$
Gumbel	$x = \xi - \alpha \log(-\log F)$	$\lambda_1 = \xi + \gamma\alpha$, $\lambda_2 = \alpha \log 2$, $\tau_3 = 0$, $\tau_4 = 0.1504$
Logistic	$x = \xi + \alpha \log\{F / (1 - F)\}$	$\lambda_1 = \mu$, $\lambda_2 = \pi^{-1}\sigma$, $\tau_3 = 0$, $\tau_4 = 30\pi^{-1} \tan^{-1}\sqrt{2} - 9 = 0.1226$

Normal	$F = \Phi((x - \mu) / \sigma)$	$\lambda_1 = \mu$, $\lambda_2 = \pi^{-1}\sigma$, $\tau_3 = 0$, $\tau_4 = 30\pi^{-1} \tan^{-1}\sqrt{2} - 9 = 0.1226$
Generalized Pareto	$x = \xi + \alpha\{1 - (1 - F)^k\} / k$	$\lambda_1 = \xi + \alpha / (1 + k)$, $\lambda_2 = \alpha / (1 + k)(2 + k)$, $\tau_3 = (1 - k) / (3 + k)$, $\tau_4 = (1 - k)(2 - k) / (3 + k)(4 + k)$
Generalized extreme value	$x = \xi + \alpha\{1 - (-\log F)^k\} / k$	$\lambda_1 = \xi + \alpha\{1 - \Gamma(1 + k)\Gamma(1 - k)\} / k$, $\lambda_2 = \alpha\Gamma(1 + k)\Gamma(1 - k)$, $\tau_3 = -k$, $\tau_4 = (1 + 5k^2) / 6$
Log-normal	$F = \Phi((\log(x - \xi) - \mu) / \sigma)$	$\lambda_1 = \xi + \exp(\mu + \sigma^2 / 2)$, $\lambda_2 = \exp(\mu + \sigma^2 / 2)$ $\text{erf}(\sigma / \sqrt{2})$, $\tau_3 = (6 - 1 / 256\pi^2)$ $\text{erf}(x / \sqrt{3})\exp(-x^2)dx / \text{erf}(\sigma / \sqrt{2})$
Gamma	$F = \int_0^x t^{(\alpha - 1)}\exp(-t / \beta)dt / \Gamma(\alpha)$	$\lambda_1 = \alpha\beta$, $\lambda_2 = \pi^{(1/2)}\beta\ \Gamma(\alpha + 1/2) / \Gamma(\alpha)$, $\tau_3 =$ $6I_{(1/3)}(\alpha, 2\alpha) - 3$

3.5 HEC-RAS Modelling Approach and Inundation Mapping

The identical inputs, which included the same set of boundary conditions and geometric parameters for both models, were used to compare the 1D and 2D models. The 1D model simulates an average velocity and the elevation of the water's surface at each unique cross-section, assuming that all water flow is longitudinal. On the other hand, the 2D model permits water flow when considering the flow across and along the river sections in both longitudinal and transverse directions. The 2D model models the continuous water surface distribution and velocity throughout the grid and depicts the landscape as continuous grid cells (Ghimire et al., 2022).

This study processed input data in RAS Mapper to create the 1D and 2D models. The flood analysis was carried out in HEC-RAS in the following phase. Ultimately, inundation maps were produced by post-processing the HEC-RAS model's output. Using 2D flow area and terrain created by DEM data, a 2D model was created. The computational mesh size of 100 m × 100 m was selected to maintain a fair computational time because the calculation time and mesh size are connected.

3.5.1 1D HEC-RAS Modeling

Geometric Data

Many geometric data are needed for the hydraulic modeling of HEC-RAS to configure the physical properties of the flood plain into the model. To precisely alter the flood plain's real coverage area, it is highly recommended that appropriate geometric and topographic data be utilized (Namara et al., 2022). Accurate mapping of flood inundation requires a high-resolution digital elevation model (DEM). In order to achieve this objective, a 12.5 m × 12.5 m high-resolution digital elevation model was acquired from the Alaska Satellite Facility (https://vertex.dac.asf.alska.edu). Making precise inundation maps benefits from the use of very accurate digital elevation modeling (DEM). As a result, Ras mapper was used to create the geometric features and cross-sections that were fed into the 1D and 2D models using the DEM dataset.

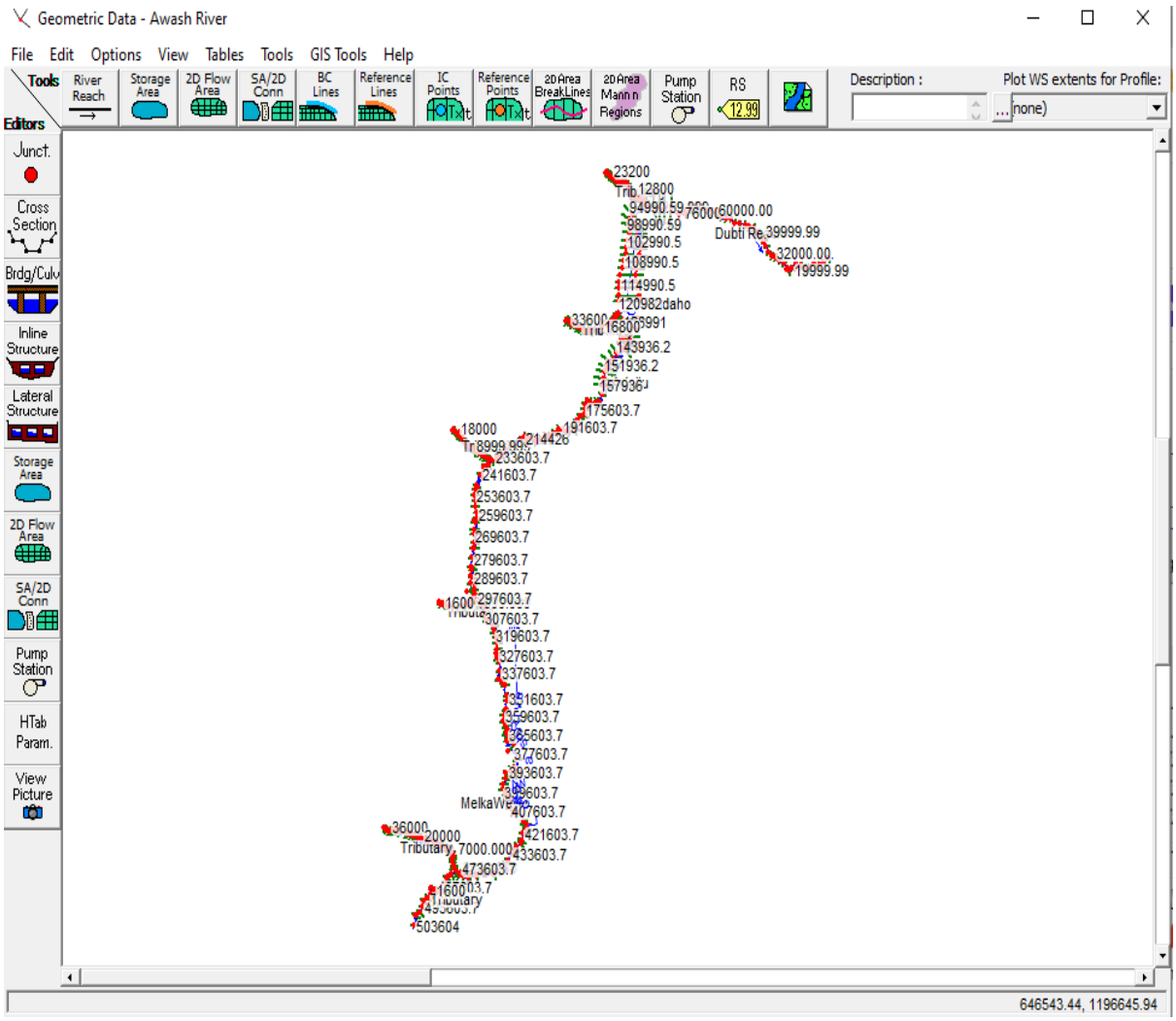

Figure 3. 5 Geometric data

Land use data

The European Space Agency provided the sentinel-2 land use data at a resolution of 10 meters (ESA). For the 2D model, Manning's roughness value was applied according to each land-use attribute.

Flow and boundary conditions

The Ethiopian Ministry of Water and Energy (MoWE) provided the flow data needed for the boundary conditions of the 1D and 2D models. While the downstream condition was used as a normal depth using the average slope of the channel at the downstream station for both models, the 1D model used estimated flood quantiles, and the 2D model used annual maximum series (AMS) flow hydrographs at the upstream boundary condition.

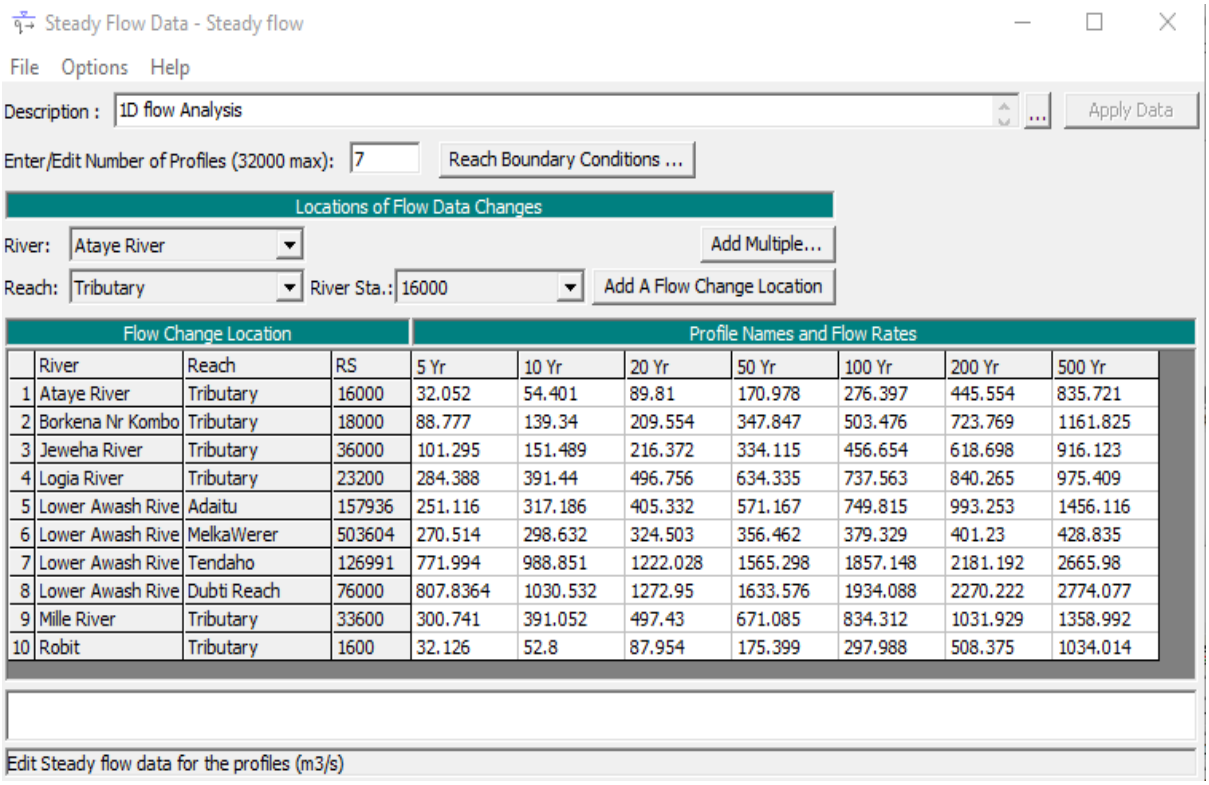

	River	Reach	RS	5 Yr	10 Yr	20 Yr	50 Yr	100 Yr	200 Yr	500 Yr
1	Ataye River	Tributary	16000	32.052	54.401	89.81	170.978	276.397	445.554	835.721
2	Borkena Nr Kombo	Tributary	18000	88.777	139.34	209.554	347.847	503.476	723.769	1161.825
3	Jeweha River	Tributary	36000	101.295	151.489	216.372	334.115	456.654	618.698	916.123
4	Logia River	Tributary	23200	284.388	391.44	496.756	634.335	737.563	840.265	975.409
5	Lower Awash Rive	Adaitu	157936	251.116	317.186	405.332	571.167	749.815	993.253	1456.116
6	Lower Awash Rive	MelkaWerer	503604	270.514	298.632	324.503	356.462	379.329	401.23	428.835
7	Lower Awash Rive	Tendaho	126991	771.994	988.851	1222.028	1565.298	1857.148	2181.192	2665.98
8	Lower Awash Rive	Dubti Reach	76000	807.8364	1030.532	1272.95	1633.576	1934.088	2270.222	2774.077
9	Mille River	Tributary	33600	300.741	391.052	497.43	671.085	834.312	1031.929	1358.992
10	Robit	Tributary	1600	32.126	52.8	87.954	175.399	297.988	508.375	1034.014

Figure 3. 6 Steady flow data for different return periods

Running Steady flow

The necessary steady flow data are entered for the HEC-RAS simulation once all geometric data have been entered. A 1D steady state is chosen for modeling in consideration of the needed model outputs, the degree of detail, and the anticipated accuracy of the outcomes. The simplest to utilize and comprehend the outcomes of are 1D steady flow models. It is necessary to enter

the flow regime to be selected, the number of profiles to be calculated, and the boundary conditions. The selected flow regime is sub-critical, characterized by comparatively deep depths and slower velocity. From the four boundary conditions of the 1D steady-state flow, normal depth is selected as the downstream boundary condition and QT is selected as the upstream boundary condition. An energy slope needs to include a boundary condition of normal depth. Manning's equation will be used by HEC-RAS to calculate depth based on that value.

The HEC-RAS output is exported as a "RASExport.sdf" file format following a successful simulation by choosing the "Water Surfaces" and "Export Velocity Distribution" choices, respectively, for the inundation depth and velocity. These options are then processed in a GIS for flood inundation and hazard mapping. Based on the velocity distribution calculated in HEC-RAS with one point at the centroid of a flow distribution location, the velocities are exported.

3.5.2 2D Modelling Process

HEC-RAS software imports a 12.5-meter resolution digital elevation model (DEM) from the Alaska satellite facility. Now, utilize the RAS-Mapper Tools menu to create terrain from a chosen Digital Elevation Model (DEM). RAS-Mapper will then use this terrain to work on the hydrodynamic properties and construct the geometry of the research area's 2-D flow region.

To calculate the flow field in the designated 2-D mesh, HEC-RAS 2-D provides two computational approaches: diffusion wave computations and complete momentum (Saint-Venant) equations (Brunner, 2016). Less computing time and increased model stability are promised by the diffusion wave solver. To finish the simulations, the 2-D full momentum equation solver needs more processing power and time because it takes into account the Coriolis and turbulence effects in the flow field.

2-D mesh area and selection of cell size

By defining a 2-D flow area, a polygon is drawn inside the bounds of the underlying topography to create a 2-D mesh. Setting the cell center spacing results in the development of a uniform hexagonal mesh over the underlying terrain (Rangari et al., 2019). The mesh cell size and model simulation time step influence the simulation run time and output mapping accuracy. The run time increases with the number of cells.

The area that is used for 2-D flow computations is designated as the 2D flow area in HEC RAS. The layer is designated as a polygon for the study area. Within a predetermined 2-D flow area,

a computational 2-D mesh is created with 100-meter cell spacing. Since it matches the DEM resolution and is appropriate for computations, a 100m mesh is used in this instance.

Time step selection

The model offers sufficient accuracy and stability, with Courant numbers as high as 3.0 for complete momentum equations and as high as 5.0 when using the diffusion wave equations. The model offers sufficient accuracy and stability, with Courant numbers as high as 3.0 for complete momentum equations and as high as 5.0 when using the diffusion wave equations (Brunner, 2016). For greater output accuracy, a model running for a small urban region should utilize a Courant number less than 1.0. The most crucial need is that the time step be large enough to yield quickly identifiable steady outcomes. In general, for a model simulation run, the time step or computation interval needs to be small enough to let water passage through computational cells. For a 60 m cell spacing, the HEC RAS manual recommends a fair time step of 30 s. However, this can be changed as long as acceptable results are obtained without significantly losing accuracy. It is best to do a rough initial run with a coarser time step (1–5 min) to balance the model stability and output accuracy. In the current work, the model simulation was first run using a time step of 1 min, then 1 s was progressively adjusted to capture higher output precision without compromising model stability.

In RAS-mapper, as stated (Brunner, 2016) manning's roughness coefficient was assigned to the 2D region that is taken into consideration for the study area. The related Manning's n value and the allotted land cover value are displayed in Figure 3.4 below. Give the area of the river its upstream and downstream boundary conditions to simulate unsteady flow in the RAS-mapper. The annual maximum series hydrograph for each station was used for simulation upstream, while the normal depth of the channel slope served as the boundary condition downstream. The generated geometric layer for the 2D river area and the boundary conditions that were applied are described in Figure 3.5 below.

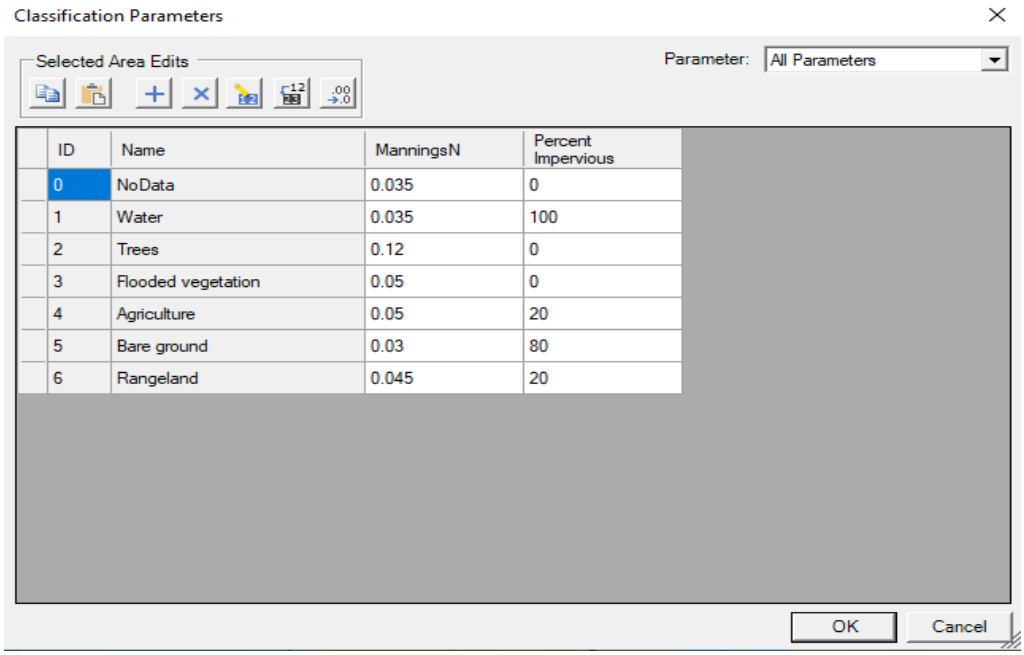

Figure 3. 7 Manning's roughness coefficient assigned to the 2D region

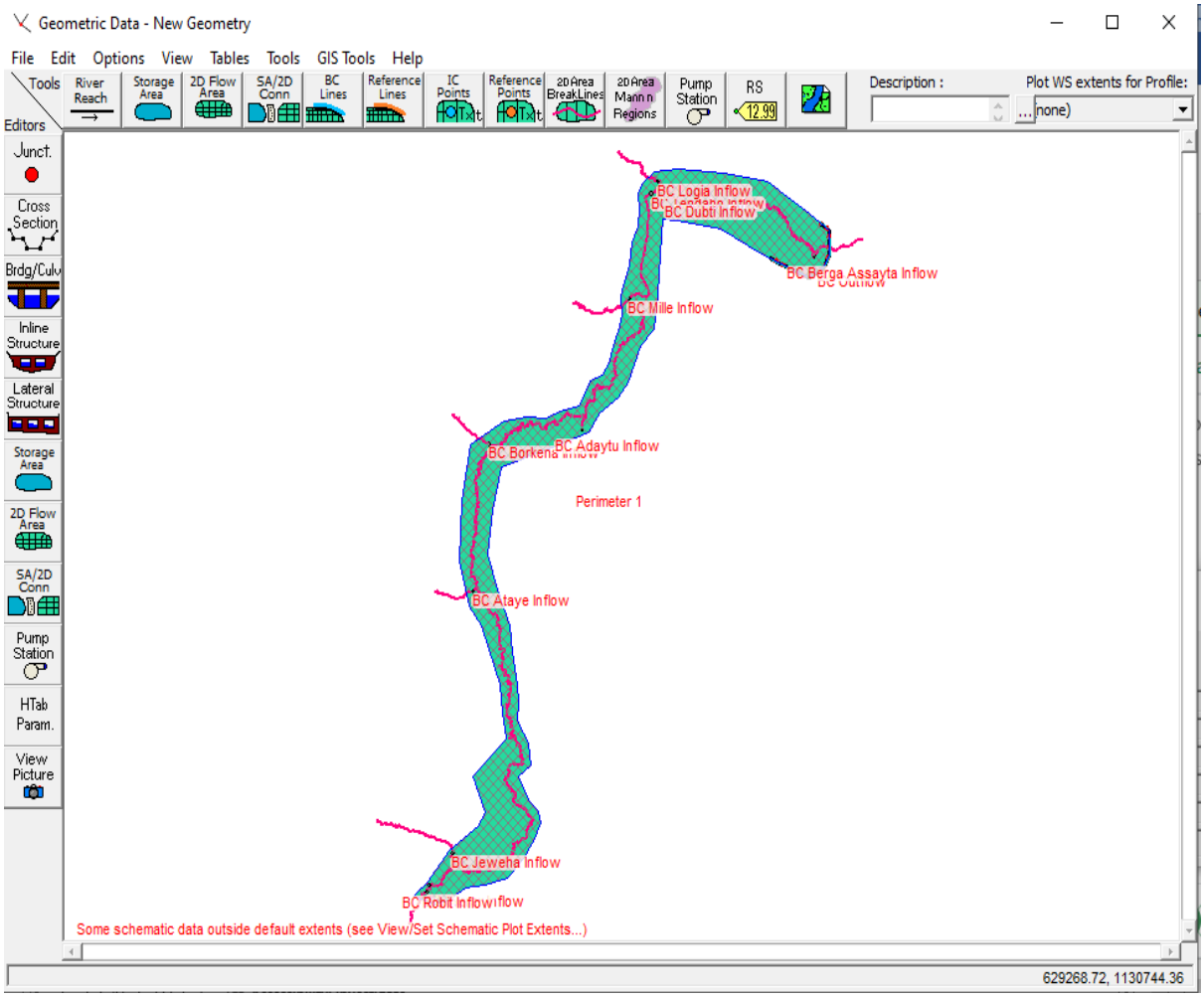

Figure 3. 8 Created a geometric layer using a two-dimensional flow area cell mesh

3.5.3 Flood Inundation Mapping

The next step after determining the design floods is to create flood inundation maps using a hydraulic model and all available main and secondary data (Baky et al., 2019). For inundation modeling, the HEC-RAS 6.5 version, a modeling software tool was used in this study.

With a return time of 5, 10, 20, 50, 100, 200, and 500 years, this part explains how to carry out the task of mapping flood inundation using a RAS mapper and HEC-RAS for the output of flood extent, depth, and velocity on the river channel and its floodplain. Three processes make up the inundation mapping process: RAS mapper processing, HEC-RAS processing, and post-RAS processing.

The GeoRAS addon is used to produce a water surface TIN for each flood occurrence before generating floodplain shape files. The original TIN layer is superimposed over the water surface TIN to enable automatic delineation of floodplains using the information present in the RAS GIS output file. The water depth is produced by the intersection of the TIN terrain model and the TIN water levels model. Using the "Flow Distribution Simulation" option, the detailed velocity data exported from the HEC-RAS is interpolated to create the velocity map.

3.6 Model Calibration and Validation of the hydrodynamic model

3.6.1 Calibration

Channel roughness is An essential factor to consider when developing a hydraulic model for flood inundation mapping and forecasting. The features of the channel roughness have an impact on river stage, discharge, and other hydraulic variables. These effects are interconnected. In studying open-channel flow, especially in hydraulic modeling, determining the channel roughness parameter is a crucial step. Numerous elements, including vegetation, abnormalities in the channel, surface roughness, and channel alignment, affect the roughness of the channel. The hydraulic model has been developed by several researchers, including (Farooq et al., 2019; Namara et al., 2022; Timbadiya et al., 2011; Trambadia et al., 2023). These researchers calibrated channel roughness for several rivers. WSE performances, both simulated and observed, will be evaluated using Nash-Sutcliffe Efficiency (NSE).

$$NSE=1-\frac{\sum_{i=1}^{n}(WSEo-WSEs)^{\wedge}2}{\sum_{i=1}^{n}(WSEo-WSEmean)^{\wedge}2} \quad (17)$$

Where WSE_O is observed water surface elevation (m), WSE_S is simulated water surface elevation (m). However, the Nash-Sutcliffe Efficiency (NSE) by itself is unable to provide us

with the model bias information. Additional statistical error index model evaluation techniques should be used to support the fitness of the simulated versus observed evaluated in the NSE. To determine if the model outcome was overpredicted or underpredicted, the PBIAS statistical error index model evaluation approach was also employed, and the equation for this model assessment was supplied (Tamiru & Dinka, 2021).

$$\text{PBIAS (\%)} = \frac{\sum_{i=1}^{n}\left(\text{Yi(Obs)-Yi(sim)}\right)*100}{\sum_{i=1}^{n}\text{(Yi(Obs)}} \quad (18)$$

Where Yi(Obs) and Yi(Sim) are observed and simulated respectively.

$$R^2 = \frac{n*(\sum XY)-(\sum X)*(\sum Y)}{[n\sum X^2-(\sum X)\text{^}2][n\sum Y^2-(\sum X)\text{^}2} \quad (19)$$

Thus, to calibrate the HEC-RAS model, the Manning roughness value of the river channel was altered in this study.

3.6.2 Validation

The main purpose of NDWI is to track and identify minute variations in the water content of water bodies. NDWI uses the green and near-infrared spectral regions to amplify the water bodies in a satellite image. MNDWI improves the extraction of open water features by utilizing the green and SWIR bands. MNDWI effectively suppresses and eliminates vegetation, soil noise, and built-up land while enhancing open water features. In the WRI approach, four spectral reflectance bands were used. It is the ratio of the combined spectral reflectance of the two visible bands, namely green and red, to the spectral reflectance of the near-infrared and middle-infrared (MIR) bands. This technique is limited to middle infrared satellite photos (Deoli et al., 2022). Nevertheless, the intended outcome of the NDWI application in water regions with a background of developed land is not met. In those areas, the gathered data on water was frequently mingled with background noise from developed land. This indicates that the NDWI image of many built-up land features also shows positive values. The MNDWI calculation will produce three results: Because soil reflects more MIR light than NIR light, built-up land will have negative values as previously said; plants and soil will also have negative values; and water will have larger positive values than in the NDWI because it absorbs more MIR light than NIR light (Xu, 2006). As a result, the MNDWI's contrast between water and built-up land will be noticeably greater than the NDWI's due to rising water feature values and declining built-up land values from positive to negative. The presence of greater water enhancement in the MNDWI image may allow for a more accurate extraction of open water

features. This is because vegetation, soil, and built-up land all have negative values, which considerably reduce, if not totally eliminate, these features.

Researchs (Farooq et al., 2019; Tamiru & Dinka, 2021), compare the accuracy of these simulations with observable water bodies that were extracted from satellite data using an indicator called the NDWI. In this study, the inundation map generated by HEC-RAS will be compared with the water body described by the Normalized Difference Water Index (NDWI). NDWI uses the green (Band-2) and near-infrared (Band-4) bands in remote sensing images to identify water bodies. The primary inputs for NDWI are short-wave infrared (SWI) and near-infrared (NIR) wavelengths. Based on overlapping areas, the HEC-RAS inundation map and the LANDSAT 7 remotely sensed imagery derived from https://earthexplorer.usgs.gov/ in NDWI were evaluated for performance for the historical flood event in awash river for the year August 09, 2005.

$$NDWI = (Green - NIR)/ (Green + NIR) \quad (20)$$

$$MNDWI = (Green - SWIR_1)/ (Green + SWIR_1) \quad (21)$$

band 2, band 4, band 5, and band 7 for Landsat 7 images, respectively.

Calculating the percentage of overlapped area between the water bodies defined in NDWI, MNDWI, and HEC-RAS software was done using the intersect tool in the Analysis toolbox of ArcGIS (ver. 10.8). After utilizing a conversion tool to transform the raster formats of the three outcomes (NDWI, MNDWI, and HEC-RAS) into vectors (Polygons), ArcGIS's geometry computation tools were utilized to ascertain the pertinent shape areas. The percentage of overlapped regions was calculated after both polygons were remapped to the same geographic coordinate system Adindan UTM Zone 37 N (Tamiru & Dinka, 2021).

$$\text{Overlapping percentage (\%)} = \frac{\text{Layer 1 (Km2)}}{\text{Layer 2 (Km2)}}$$ The area of the water body defined in NDWI by flood occurrences is known as Layer 1, while the area of the inundation map produced in HEC-RAS is known as Layer 2. Tamiru and Dinka (2021) conducted a study wherein the inundation map was assessed based on overlapping areas. A percentage of overlap exceeding 85% was deemed to be in good agreement.

3.7 Flood Hazard Assessment

The study (Farooq et al., 2019) presents a comprehensive assessment of flood hazards in the River Swat using advanced modeling techniques and high-resolution DEM data. The findings emphasize the importance of non-structural flood mitigation measures and provide valuable insights for effective flood hazard management in the study area.

Determining each flood's characteristics and likelihood of occurring is necessary for assessing flood hazards. The current study uses flood frequency analysis to calculate each flood's likelihood of occurring, and the flood factors taken into account are flood extent, depth, and flow velocity (Vojtek & Vojteková, 2016).

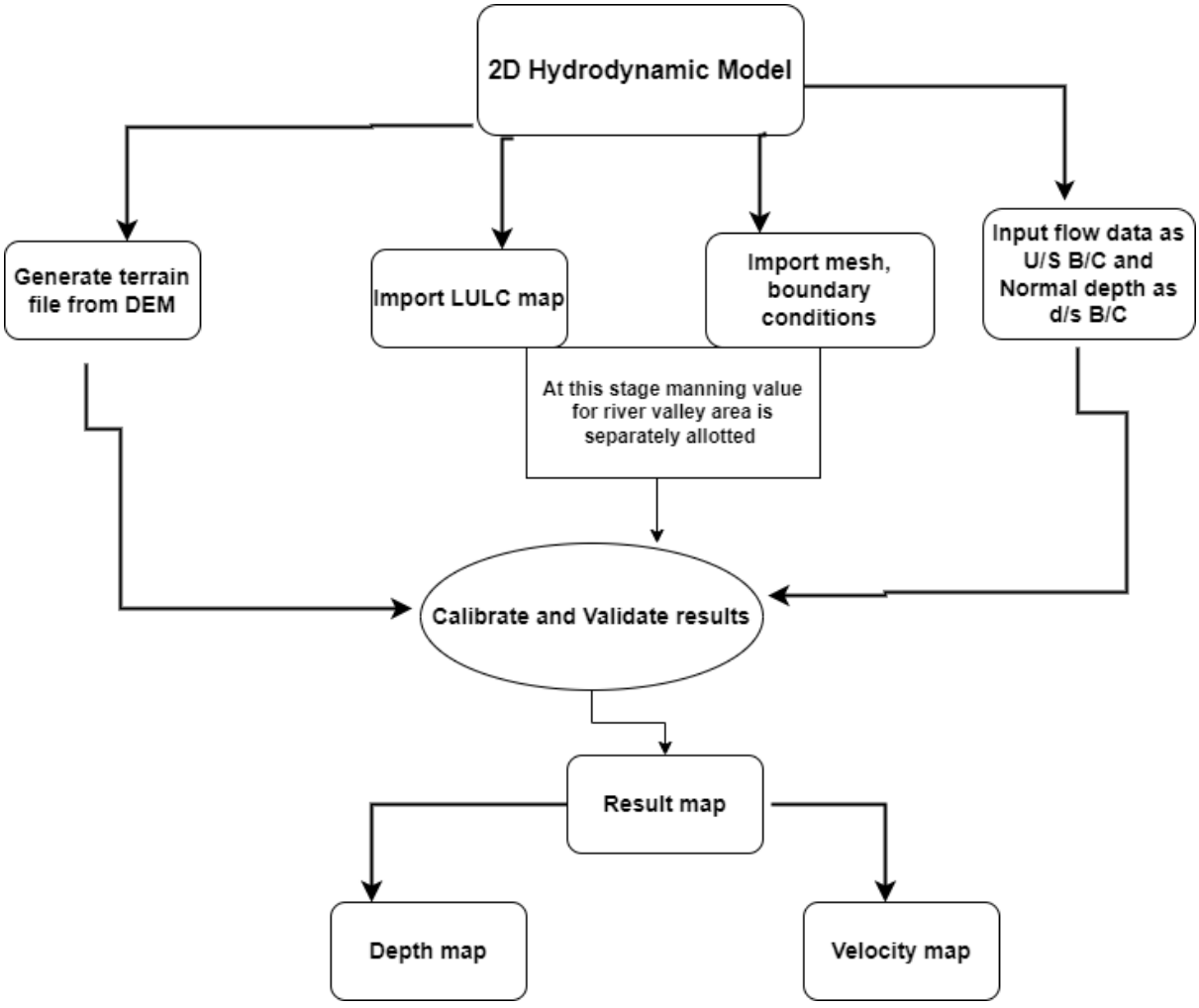

Figure 3. 9 Data process algorithm and 2D hydrodynamic model in HEC-RAS (Brunner, 2016; Trambadia et al., 2023)

3.8 Application of Google Earth Engine Cloud Platform

Scholars have recently become interested in simulations based on machine learning techniques since they save time and don't require setup equipment. The Google Earth Engine platform shows the results in a terminal and offers an interface for working using JavaScript object notation (JSON). More than 40 years' worth of data from GEE have been archived and are accessible using the platform's scripts. GEE is well-known for its atmospheric analysis, air pollution, hazard management, environmental mapping, and NDVI (normalized difference vegetation index). Because of a modern methodology, a few sections of the paper show how to use GEE for flood mapping (Trambadia et al., 2023).

In this case study, floods in the LARB were mapped using the sentinel 1-C band between July 28, 2022, and September 10, 2022. Flood mapping can benefit from this synthetic aperture radar (SAR) data, which has been available since 2017. It is best to use the Sentinel 1-C band for access in the absence of clouds. A comprehensive analysis of flooded areas must look at the actual flooded and damaged agricultural, built-up areas, barren terrain, and forest cover (Trambadia et al., 2023).

In a near-polar orbit, Sentinel-1A and Sentinel-1B form a sun-synchronous constellation. The flooded area was extracted using the Ground Range Detected (GRD) product of the Sentinel-1A satellite, which provided data in the C-band dual-polarization channels (VH and VV) with a 12-day repetition cycle. The Sentinel-1A data has a resolution of 10 m pixels. Every year, the Copernicus 100 m Global Land Cover data are updated and made available to the public on moderate-resolution maps. Strong temporal stability was seen throughout the Copernicus LULC data mapping process, with an overall mapping accuracy of over 80% (Pandey et al., 2022).

3.8.1 Methods to Flood Mapping Using Google Earth Engine Platform

Identifying the study area

The area of the shape file of the study was imported from the HEC-RAS 2D flow area perimeter. This is to include in the computation the entire region of the lower Awash flow.

Load and Filter Sentinel-1 Data

With up to nine local observations every 12-day repetition cycle, depending on the region, Sentinel-1 is the first Synthetic Aperture Radar (SAR) mission to use multiple satellites to give high spatial resolution (10 m) global coverage. Sentinel-1 is not impacted by cloud cover or

lightning when gathering backscatter imagery at the C-band in several polarizations. Unlike earlier SAR missions, Sentinel-1 satellites have a dedicated observation scenario that achieves exceptional ground coverage, allowing them to catch dynamic land surface changes and processes across large areas. This ensures that no significant event is missed. This is crucial for real-world applications as well as for improving scientific algorithms that are trained on lengthy, dense time series. Sentinel-1 gathers C-band (5.4 GHz) SAR imaging methodically to satisfy the demands of operational users. All data are processed in sequential order and made available to users within a day. When operating over land, the Sentinel-1 sensors are by default in Interferometric Wide-swath (IW) mode, which has a spatial resolution of 20 × 5 m2 and covers a 250 km wide swath at two polarizations (typically VV and VH) (Wagner et al., 2021).

Visualize RGB Composites (Red Green Blue)

Remote sensing data often comprises multiple bands capturing different wavelengths of the electromagnetic spectrum. While each band provides valuable information, visualizing them individually can be overwhelming for human interpretation. RGB (Red, Green, Blue) composites offer a powerful tool to combine multiple bands into a single image resembling the natural color view or highlighting specific features for analysis.

Apply Speckle Filter

In the picture, speckle sounds like salt and pepper noise. The image is first given a filter to smooth it out and lower the noise before any other operations are done. There are a variety of filter kinds. A more methodical way to reduce the noise in the signal is to use the refined Lee filter. The Refined Lee function needs to receive the raw picture. Thus, the toNatural function is used to convert the log image to raw. By passing it via the DB function, the output image from Refined Lee is once more transformed to log scale.

Apply a Threshold

We can make a difference image by dividing the image that comes after by the image that comes before. We are then able to choose every pixel value that is more than 1.25 by taking a 25% change into account. This 1.25 threshold is purely subjective and can be adjusted for any region through trial and error. In general, it's typical to start with a 25% change in mind.

You can apply this threshold with the boolean function gt(). The end product will be a binary image, with the flooded area represented by a pixel value of 1.

Apply Masks

The regions where there is a chance of waterlogging are all indicated on the initial flooded map. However, this has persistent water and noise in it as well. Depending on our requirement to obtain the precise flooded region, we can filter out the other pixels. In this practice, the following topics were covered; Isolated pixels, a high-slope area, and permanent water.

Permanent water: is found by employing the GSW water collection. For the sake of this analysis, permanent water is defined as the pixel with a seasonality band larger than 5. This value can fluctuate based on information from the ground. The update mask function allows us to remove the permanent water pixels from the image.

Slope mask: is made using the DEM dataset hydroSheds. Using ee.Algorithms, the terrain slope may be computed from the DEM.Ground. A mask is applied to the sections that have a slope of more than five degrees. The majority of the water found in this region is the result of image noise.

Isolated pixel mask: is carried out to lessen noise. In the middle of nowhere, a single pixel that is recognized as a deluge is most likely noise. As a result, any pixel having fewer than eight connected neighbors may be regarded as noise and hidden. The connectedPixelCount function can be used to determine which pixels are linked by examining a pixel's connection in every direction. The function in question will yield an image containing the connected pixel counts of each pixel in the input image. Next, choose every associated pixel count more than 8 using the Boolean function gt().

Calculate Flooded Area

Sentinel image backscatter values in the microwave domain are influenced by various elements, including terrain, vegetation characteristics, land cover, soil moisture, and acquisition aspects. Because specular reflection causes the majority of the radar radiation to be reflected away from the sensor, water has little backscatter and appears dark in tone. Smooth terrain, low soil moisture, sparse flora on the surface, and standing water in fields can all contribute to reduced backscatter. The water and no-water pixels were extracted from the resulting maps using the backscatter values, and statistical metrics were then computed. Peak floods are observed to have a lower backscatter value of water class than pre-flood conditions.

Maps showing the inundation of water are made for the pre-, peak-, and post-flood phases. The entire region covered by floodwater was discovered. In this study post-flood period (final

flooded) area was calculated for flood inundation analysis and flood-affected land use land cover assessment.

Export the results to the GIS for further analysis

Ultimately, the flooded results were transferred to the GIS for additional examination. Here is the detailed code that was used: Appendice I, J, K, L, M, and N.

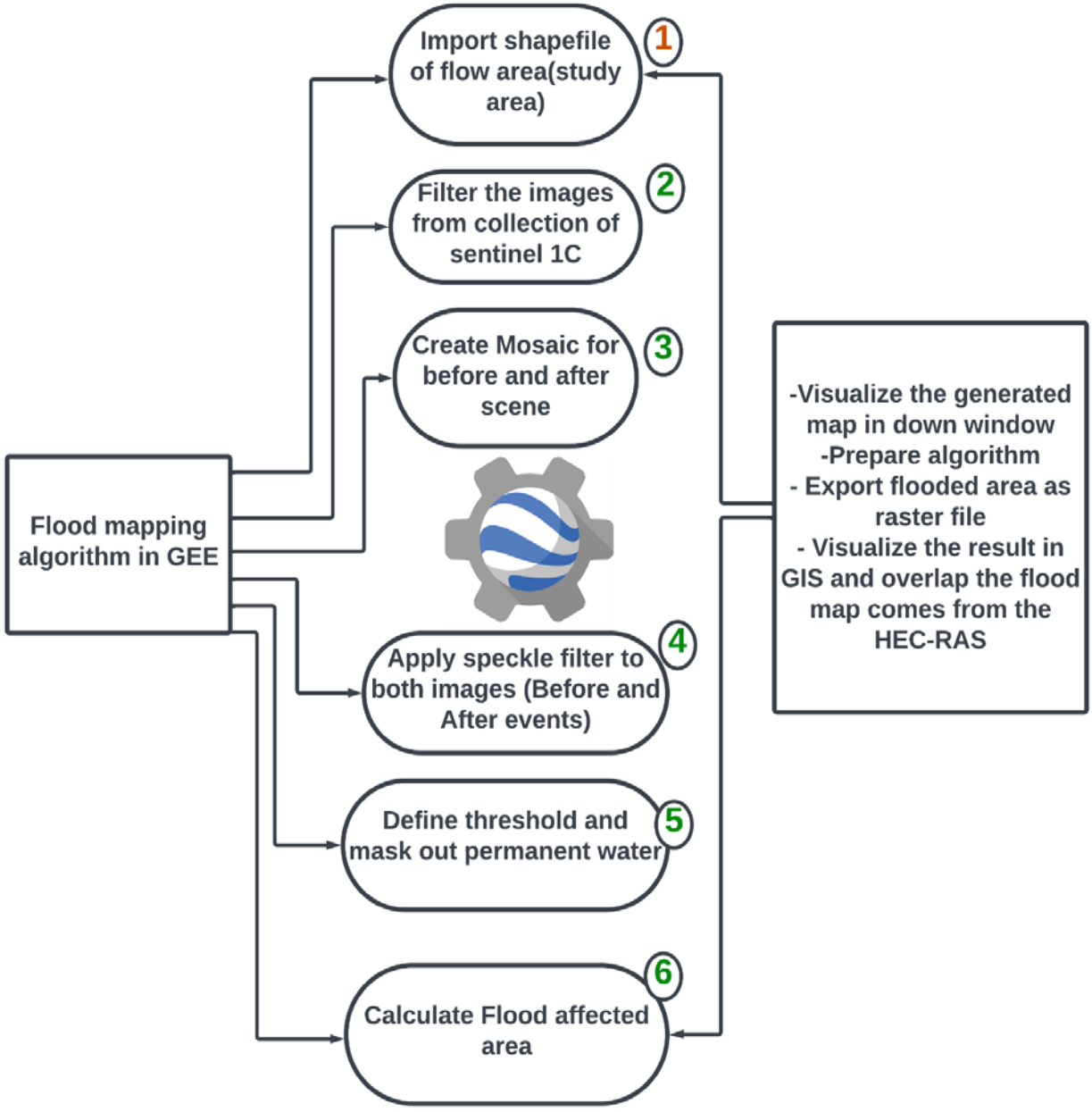

Figure 3. 10 Process algorithm showing the flood inundation mapping via the GEE platform.

4 RESULTS AND DISCUSSIONS

4.1 Hydrological Data Analysis

4.1.1 Filling of Missed Data

In the context of hydrological studies, continuous and complete stream flow data is crucial for accurate analysis and modeling. However, there were significant gaps in the hydrological stream flow data for the following periods: as an example, the Figure 4.1 for Mille station, there were missed data from October 6, 1983, to May 1, 1984; from October 25, 1988, to February 24, 1989; from August 29, 2003, to September 5, 2003; and from March 10, 2007, to October 20, 2007. These missing data periods posed a challenge for comprehensive hydrological analysis and accurate flood risk assessment.

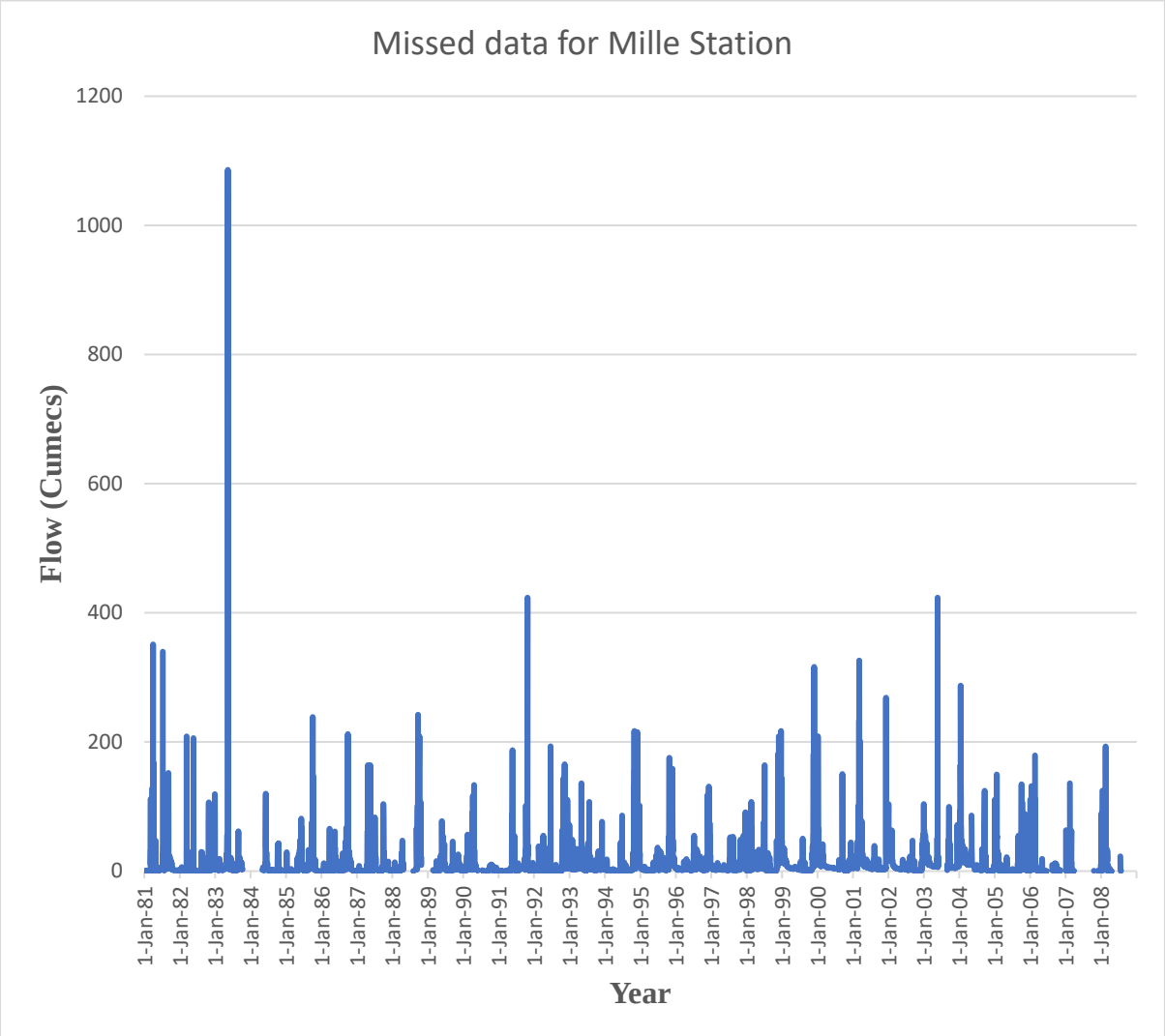

Figure 4. 1 Missed data graphical plot for Mille station

To address this issue, the missing data was filled using the Multiple Imputation methods with the IterativeImputer package from the scikit-learn library in Python as Table 4.1 shows below. This method enabled the reconstruction of the missing stream flow data, thus restoring the continuity of the dataset and improving the reliability of subsequent hydrological analyses as plotted below in Figure 4.2 for Mille station.

The application of IterativeImputer for multiple imputation ensured that the dataset was effectively completed, improving the reliability and accuracy of subsequent hydrological analyses. This approach was consistently applied to fill in missing data across all hydrological stations, ensuring uniformity and reliability in the dataset. This was a critical step to ensure the validity of flood inundation mapping and hazard assessment, as continuous and complete data is vital for the development of robust hydrodynamic models and for making informed decisions in flood risk management.

Table 4. 1 Python code used to fill missed data

```
# Import the necessary libraries

import pandas as pd

from fancyimpute import IterativeImputer

import numpy as np

import matplotlib.pyplot as plt

from sklearn.experimental import enable_iterative_imputer

from sklearn.impute import IterativeImputer


# Import the data

data = pd.read_csv(r"C:\Users\user\Documents\Python data filling Practice\Arranged LARB flow\Aw_mile@mile.csv")

df=pd.DataFrame(data)
print(df)
# Check for missing values before imputation

print(data.isnull().sum().sum())
```

```
# Define the strings representing missing values and their replacements
missing_replacements = {
    ' ': np.nan,
    '-   ': np.nan,
    '-': np.nan,
    '         ': np.nan  # Adjust this string according to the specific representation in your data
}
# Define the value representing 0
zero_replacement = 0


# Replace 0 values with NaN
data.replace(zero_replacement, np.nan, inplace=True)


# Replace string values with NaN
for missing_string, replacement in missing_replacements.items():
    data.replace(missing_string, replacement, inplace=True)


# Fill missing data using the Multiple inputation method
imputer = IterativeImputer(max_iter=10, random_state=0)
filled_data = imputer.fit_transform(data)
# Convert the imputed array back to a DataFrame
filled_data_df = pd.DataFrame(filled_data, columns=data.columns)
# Check for missing values after imputation
print(filled_data_df.isnull().sum().sum())
```

```
# Print the results

print(filled_data_df)

filled_data_df

# Save the filled data

filled_data_df.to_excel(r'C:\Users\user\Desktop\Data\Data Analysis\From
WoWE\Logia_WL1.xlsx', index=False)
```

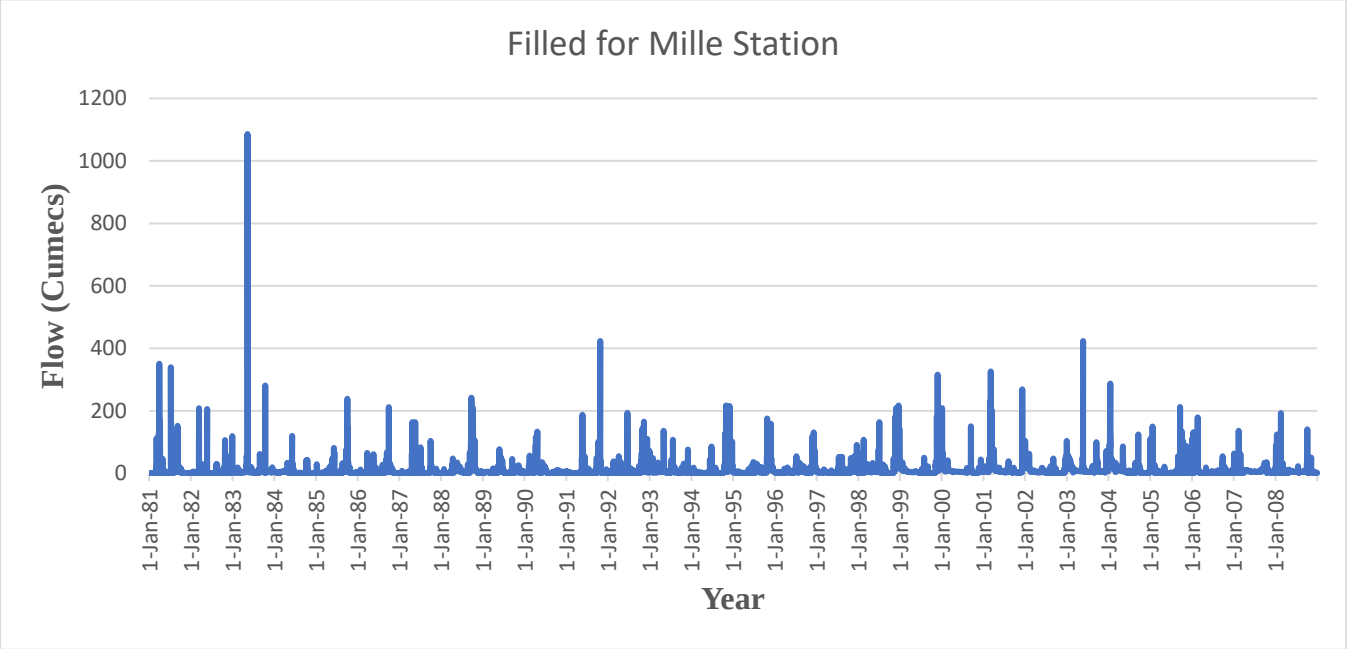

Figure 4. 2 Filled data graphical plot for Mille station

4.1.2 Homogeneity Analysis

The homogeneity of flow data was finally checked by using the Rainbow software tool. And non-homogeneity of the change point for the streamflow data was adjusted by using python code. Since the non-homogeneit Table 4. 2 can distort the actual trends in the streamflow data, it's important to adjust for it it's important to adjust for it. This can be done using statistical methods. Python, a popular programming language, offers various libraries for data analysis and statistics. These libraries in Table 4.2 provide functions to identify change points and potentially adjust the data to account for them.

Table 4. 2 Python code used to check non-homogeneity

```
# Import necessary Libraries

import numpy as np

import pandas as pd

import pyhomogeneity as hg

import matplotlib.pyplot as plt

import statsmodels.api as sm

%matplotlib inline

# read all datasets

data = pd.read_csv(r"C:\Users\user\Desktop\Data\Data
Analysis\Homogenization\Logia_Hom6.csv")

data.index = pd.to_datetime(data['Year'], format='%Y-%m-%d')

data.drop('Year', axis=1, inplace=True)

# Now your data should be indexed by the year

print(data.head())

data

# Plotting

plt.figure(figsize=(16, 6))

data.plot(figsize=(16, 6))

plt.xlabel('Year')

plt.ylabel('Flow')

plt.grid(True)

plt.show()

# Performs the Pettitt test on the 'data' to detect a change point

pettitt_res = hg.pettitt_test(data, alpha=0.05)

pettitt_res
```

```
# Performs the Buishand U test on the 'data' to detect a shift in the mean

buishand_res = hg.buishand_u_test(data)

buishand_res

# Extracting results and data information

result = pettitt_res

mn = data.index[0]

mx = data.index[-1]

loc = pd.to_datetime(result.cp)

mu1 = result.avg.mu1

mu2 = result.avg.mu2

# Setting up plot parameters

plt.figure(figsize=(15,10))

plt.plot(data, label="Observation")

plt.hlines(mu1, xmin=mn, xmax=loc, linestyles='--', colors='orange', lw=1.5, label='mu1 : ' +
str(round(mu1, 2)))

plt.hlines(mu2, xmin=loc, xmax=mx, linestyles='--', colors='g', lw=1.5, label='mu2 : ' +
str(round(mu2, 2)))

plt.axvline(x=loc, linestyle='-.', color='red', lw=1.5, label='Change point : ' + loc.strftime('%Y-
%m-%d') + '\n p-value : ' + str(result.p))

# Customizing plot appearance

plt.title('')

plt.xlabel('Year', fontweight='bold', fontsize=12)

plt.ylabel('Flow', fontweight='bold', fontsize=12)

# Enhancing axis and legend appearance

plt.xticks(fontweight='bold', fontsize=10)

plt.yticks(fontweight='bold', fontsize=10)

legend = plt.legend(loc='upper right')
```

```
for text in legend.get_texts():
    text.set_fontweight('bold')
    text.set_fontsize(10)
# Final plot adjustments and display
plt.grid(True)
plt.show()
```

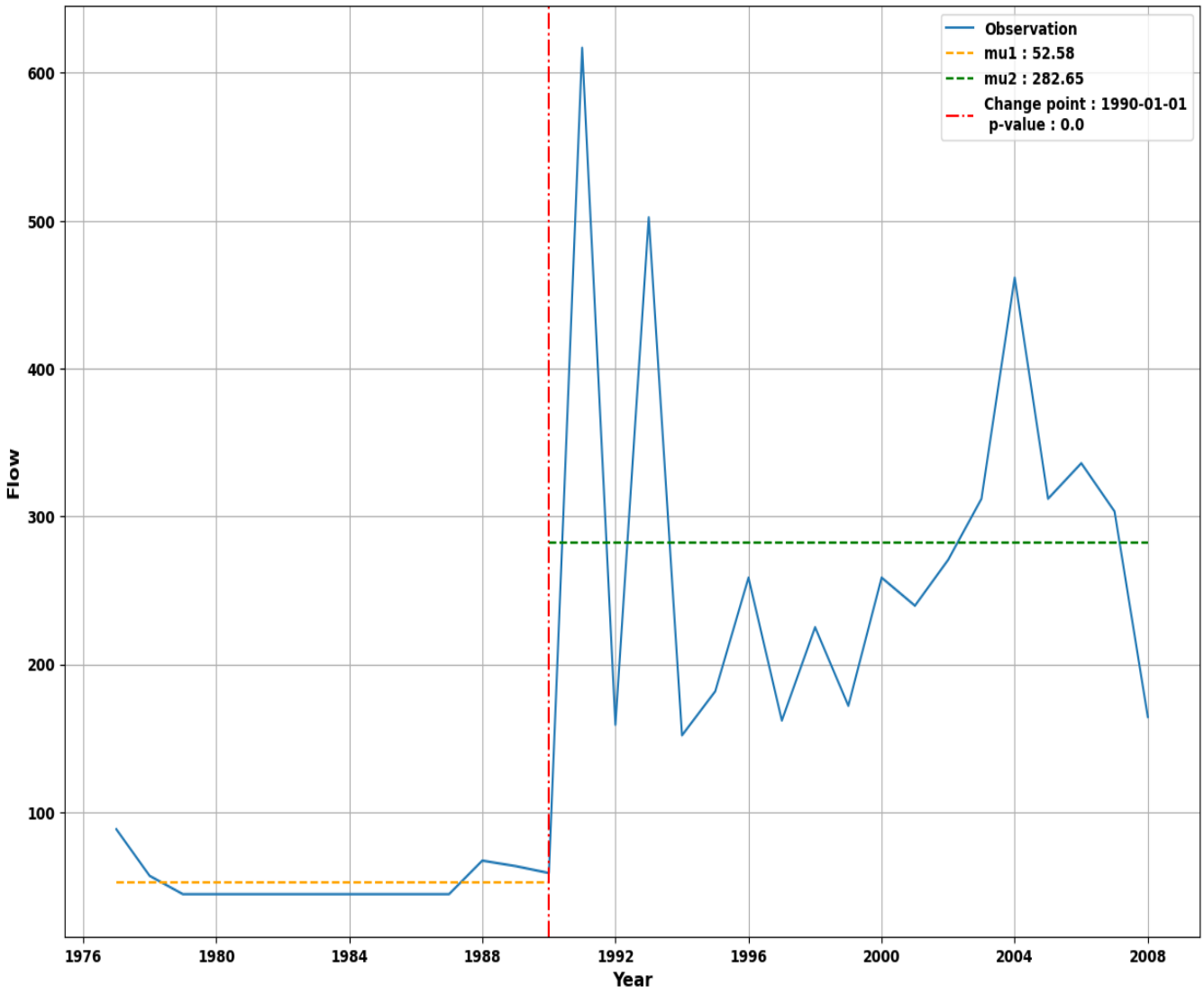

Figure 4. 3 Before Homogenization

The above Figure 4. 3 identifies the change point for the given station at the year 1990-01-01 from the beginning of the length of data with a P-value of 0.0. after knowing the change point

of heterogeneity of stream flow data; the code below Table 4.3 was applied to adjust the change point to assure the homogeneity of data using the Pettit statistical test.

Table 4. 3 Python code used to treat non-homogeneity by identifying the change point

```
# Now to detect change points and treat the data we can use the following codes.

# Step 1: Identify the change point detected by the test

change_point_index = data.index.get_loc(loc)


# Step 2: Split the dataset into two parts based on the change point

data_before_change = data.iloc[:change_point_index]

data_after_change = data.iloc[change_point_index:].copy()  # Make a copy to avoid modifying the original data


# Step 3: Apply some transformation to homogenize the data starting from the change point

# Here, you can apply any transformation method you prefer to homogenize the data

# For example, you can apply a simple mean adjustment to make the two segments continuous

mean_adjustment = mu2 - mu1

data_after_change -= mean_adjustment


# Step 4: Adjust the data after the change point to ensure non-negative values

data_after_change[data_after_change < 0] = 0


# Step 5: Concatenate the original data before the change point with the adjusted data after the change point

homogenized_data = pd.concat([data_before_change, data_after_change])

# Step 6: Save the modified dataset to a CSV file

homogenized_data.to_csv(r"C:\Users\user\Desktop\Data\Data Analysis\Homogenization\Logia_Hom6.csv")
```

The plot in Figure 4.4 shows the heterogenous data was homogenized after several processes of homogenization. The change point was minimized and the data is 95% homogeneous. This process was held for all stations to treat and test the homogeneity of stream flow data.

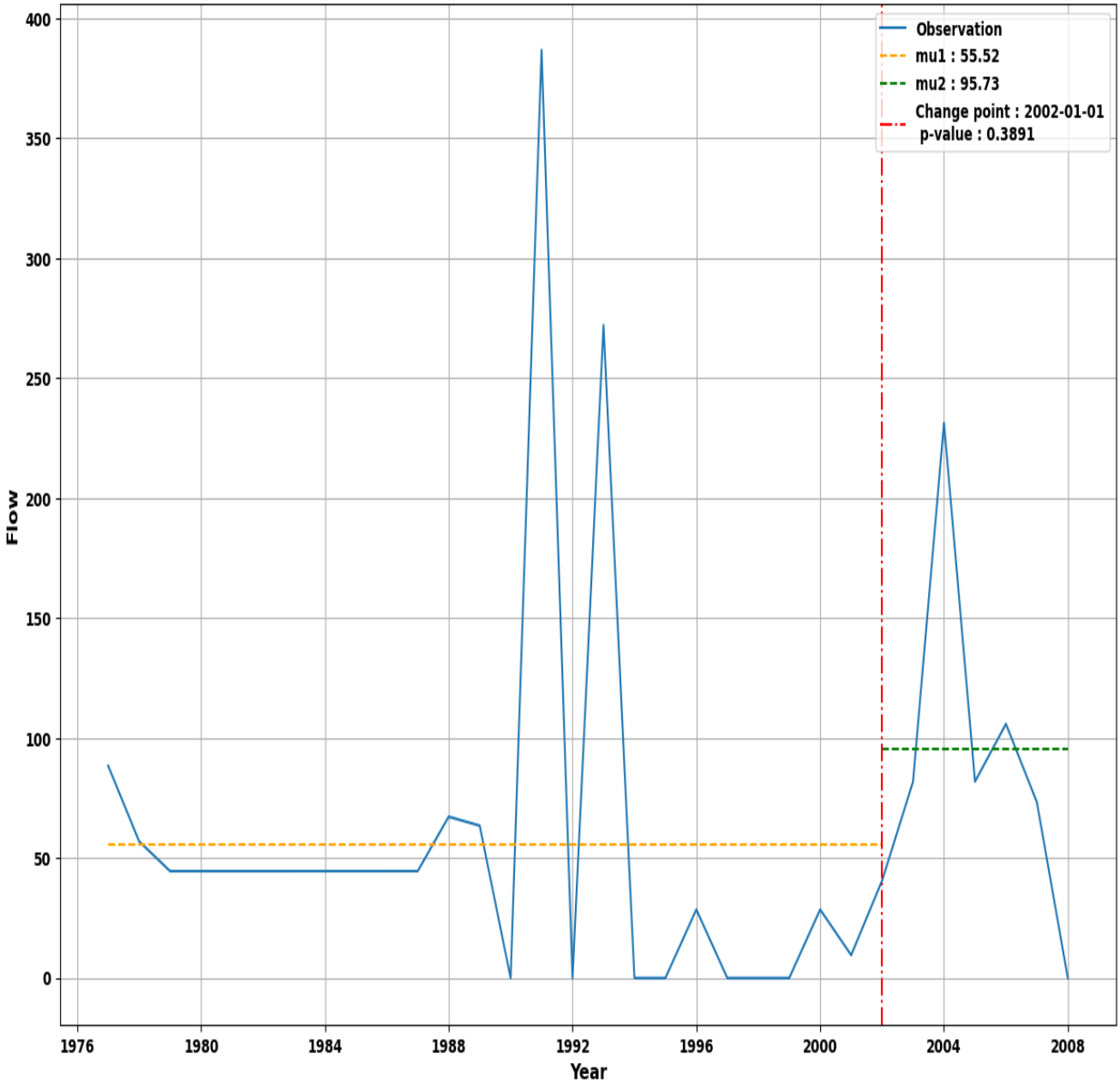

Figure 4. 4 After Homogenization

As stated by (Raes et al., 2016), data that are to be analyzed using frequency must be independent and homogeneous. The observations are guaranteed to come from the same population by the homogeneity restriction. A homogeneity test based on cumulative departures from the mean is conducted (Buishand, 1982). Buishand's homogeneity test was used to

determine the homogeneity of AMS in each station. Since there is no discernible pattern in the Xi's deviations from their average value $\overline{X}$, one may anticipate that the Sk's will oscillate around zero for a homogenous record. With 0.1, 0.05, and 0.01 degrees of freedom represented by the 90%, 95%, and 99% confidence intervals, the null and alternative hypotheses were investigated. For illustration, the result of the homogeneity test for one representative station is presented in (Figure 4.5). This figure demonstrates the application of the Rainbow software tool in assessing the consistency of the stream flow data. The test results indicate that the data for this station is homogeneous, confirming the reliability of the data for further analysis. According to the results, every station has a 95% confidence interval that indicates homogeneity.

To provide comprehensive coverage, the homogeneity test results for the remaining hydrological stations are included in Appendix A. These results similarly show that the data from the other stations have been checked for homogeneity, ensuring that all data sets used in this study are reliable and suitable for subsequent hydrological modeling and flood risk assessment. By including these detailed homogeneity test results, we underscore the robustness of our data validation process, reinforcing the credibility of our study's findings and conclusions regarding flood inundation mapping and hazard assessment in the Lower Awash River Basin, Ethiopia.

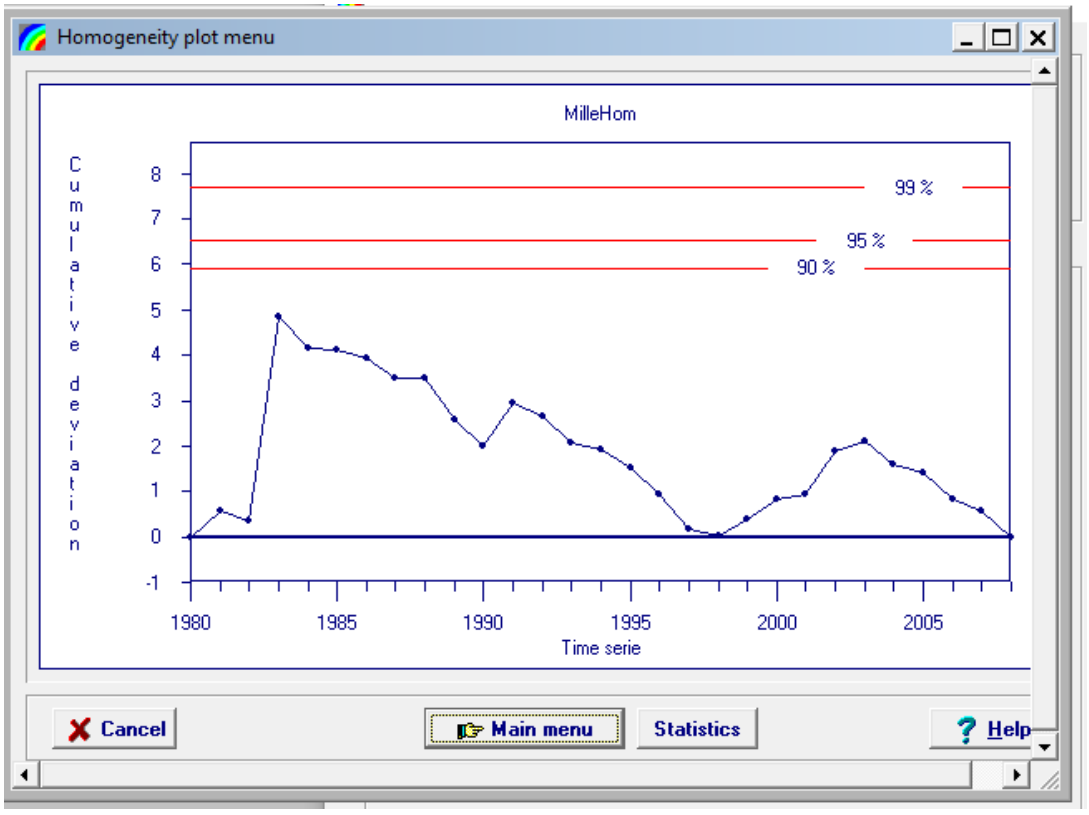

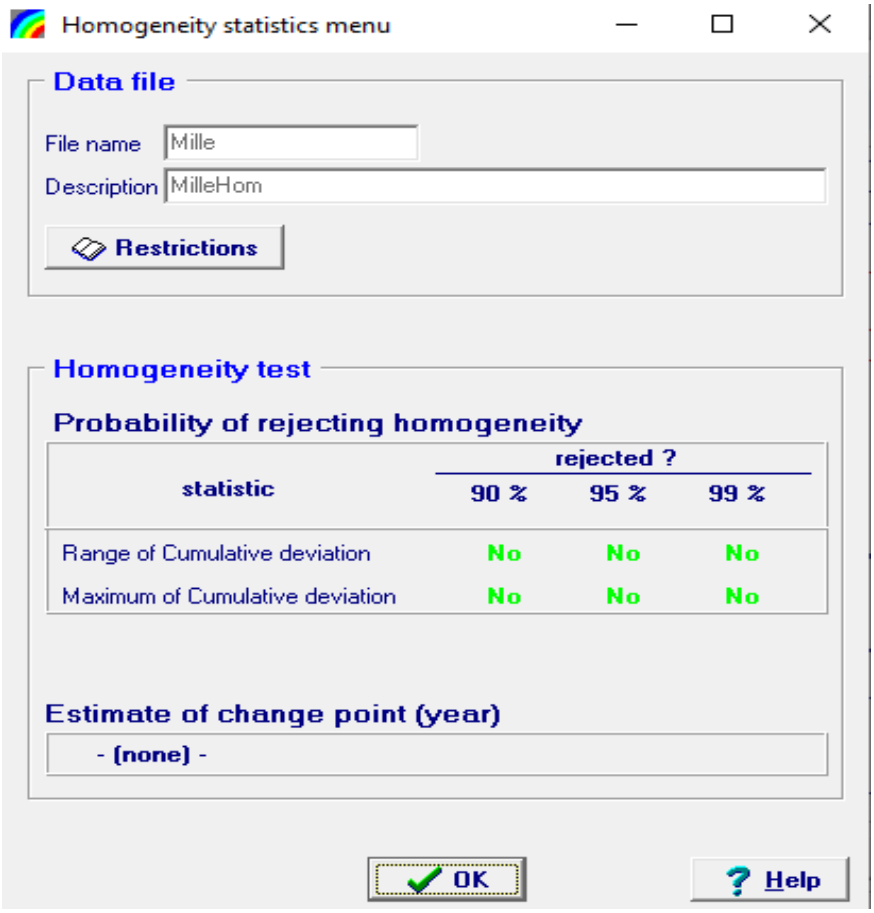

Figure 4. 5 Homogeneity test using Rainbow software tool for Mille Station

4.1.3 Outlier Detection and Treatment

The Grubbs and Beck (1972) test was used to detect outliers. The outlier was detected and treated for the stations of Tendaho, Mille, Borkena, and Ataye. For these stations, the higher outlier was adjusted to the second-largest event for each station. The details of the analysis are stated in the Table 4.4.

Table 4. 4 Outlier detection and treatment

Stations	N	KN	QH	QL	Outlier	Remark
Melka Werer	38	2.703144723	405.4726004	10.318	-	Accepted
Robit	22	2.46025594	755.7865388	0.028834654	-	Accepted
Tendaho	34	2.655782893	2136.154215	2.565008653	1.505	Rejected (Lower Outlier)
Mille	28	2.570679278	809.6862025	0.09881933	1086	Reduced to second largest event

Logia	32	2.62955249	1305.172361	1.345437309	-	Accepted
Jeweha	22	2.46025594	505.4309811	0.041447915	-	Accepted
Borkena Kombolcha	26	2.537323661	505.7485658	0.088742443	597.238	Reduced to second largest event
Ataye	17	2.335966682	221.5046821	0.022645189	343.275	Reduced to second largest event
Adaitu	23	2.481022625	1267.083223	7.360757598	-	Accepted

4.2 Goodness of Fit and Flood Quantile Estimation

4.2.1 Goodness of Fit Analysis

Kolmogrov-Smirnov (KS statistics test) and the L-moment ratio diagram were used to evaluate the goodness of fit. Below is an explanation of the mathematical basis for the L-moment ratio diagrams. The notion of L-moments, or linear combinations of probability-weighted moments (PWM), was initially introduced by Hosking (1990). The nearest close margin of the dispersion from the distributions was used to determine the best-fit pdf to suit the station's sample data (Haddad, 2021).

As a study conducted by (Drissia et al., 2019), LMRD Provides a visual approach to compare multiple probability distributions, focuses on higher-order moments (skewness and kurtosis), useful for selecting candidate distributions. However, Smaller sensitivity to data variations, may not be as responsive as other methods and requires a finite mean but not higher moments.

The Kolmogorov-Smirnov (KS) test uses the statistical method for comparing observed data to theoretical distributions, quantifies the maximum vertical distance between empirical and hypothesized CDFs, widely used and robust. Hence for this study, the KS test was applied to fix the fitted distribution for each stream flow station for the sake of rigorous statistical assessment. The KS statistics were analyzed using the HEC-SSP software tool for the L-moments (LM) distribution fitting method. Distribution has the lowest KS statistic suggesting the best fit among the listed distributions. The result is stated under the following Table 4.5.

Table 4. 5 HEC-SSP statistical software output KS test

SITE	Kolmogorov-Smirnov (KS statistics test)	Best fitted distribution
Borkena. COMBOLCHA	0.156	Generalized Pareto (LM)
@ Robit Village	0.192	Generalized Extreme Value (LM)
@ Jeweha	0.108	Generalized Extreme Value (LM)
Ataye	0.094	Generalized Pareto (LM)
@ Mille Village	0.086	Generalized Logistic (LM)
@ Tendaho	0.07	Generalized Logistic (LM)
@ Logia Village	0.156	Pearson III (LM)
@ Adaitu	0.11	Generalized Logistic (LM)
Melka Werer	0.11	Generalized Logistic (LM)

4.2.2 Flood Quantiles Estimation

For ungauged catchments, regional flood frequency analysis (RFFA) is used; for gauged catchments, flood frequency analysis (FFA) can be used to forecast design floods. This study compares two popular RFFA techniques: the quantile regression technique (QRT) and the index flood method (IFM). Predicting flood quantiles involves several parameters, one of which is the area of catchment (extent). Almost all prior RFFA studies have made use of AREA. AREA is highly correlated with many other catchment variables, including slope, stream order, and stream length. Among the various morphometric variables, the area is the most commonly employed and is recognized as the primary scaling factor in statistical hydrology (Zalnezhad et al., 2023).

The Dubti Station faced significant gaps in its data records, particularly concerning its catchment area. To address this, we employed a regression technique, utilizing data from neighboring stations such as Mille, Tendaho, and Logia as shown in Table 4.6.

Table 4. 6 Stations near the Dubti station with their catchment area and flood quantiles

Stations	Area (km^2)	5 Yr	10 Yr	20 Yr	50 Yr	100 Yr	200 Yr	500 Yr
Tendaho	62088	771.994	988.851	1222.03	1565.3	1857.15	2181.19	2665.98
Logia	3994	284.388	391.44	496.756	634.335	737.563	840.265	975.409

Mille	4467	300.741	391.052	497.43	671.085	834.312	1031.93	1358.99

Through a process of regression, we developed an equation that accurately estimates flood quantiles for the Dubti Station, thereby filling in the missing data and enhancing our understanding of flood patterns in the region.

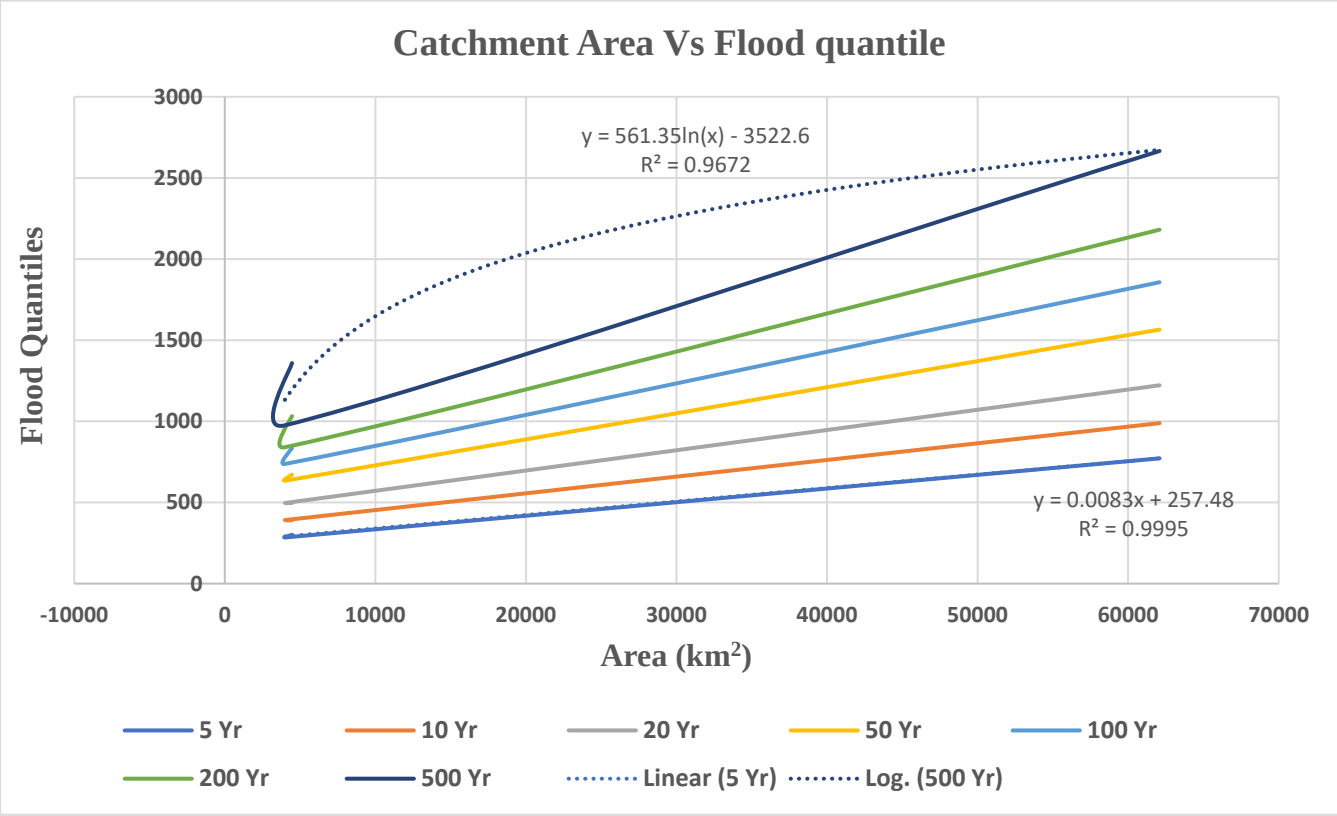

Figure 4. 6 Catchment Area Vs flood quantiles Mille, Tendaho, and Logia stations

Using the quantile regression technique shown in Figure 4. 6; the equation to estimate the quantile flood for Dubti station was generated under Table 4. 7 based on its area of the catchment. The area catchment Dubti station was explained above in Table 3. 2 was 66308 km^2. So, regression was analyzed using stations of Mille, Tendaho, and Logia then, the following equation was developed.

Table 4. 7 Developed equations to estimate flood quantiles for Dubti Station

Return Periods	R^2	Developed Equations	Flood quantiles (m^3/s)
5 Year	0.995	QT = 0.0083A + 257.48	807.8364
10 Year	0.999	QT = 0.0103A + 347.56	1030.5324
20 Year	0.9999	QT = 0.0125A + 444.1	1272.95

50 year	0.9992	QT = 0.0158A + 585.91	1633.5764
100 Year	0.9982	QT = 399.15ln(A) - 2546.9	1884.489577
200 Year	0.9907	QT = 464.86ln(A) - 2946.3	2214.606323
500 years	0.9672	QT = 561.35ln(A) - 3522.6	2709.544655

After successfully testing the best-fitted distribution by Kolmogrov-Smirnov (KS statistics test) and making regression analysis for the ungauged station; the flood quantiles were estimated for the return periods of 5,10,20,50,100,200,500 years as shown in table 4.8.

Table 4. 8 Flood quantiles for different return periods for the hydrological stations

Return Period	**Borkena. COMBOLCHA**	**@ Robit Village**	**@ Jeweha**	**Ataye**
500	1161.825	1034.014	916.123	835.721
200	723.769	508.375	618.698	445.554
100	503.476	297.988	456.654	276.397
50	347.847	175.399	334.115	170.978
20	209.554	87.954	216.372	89.810
10	139.340	52.800	151.489	54.401
5	88.777	32.126	101.295	32.052
Return Period	**@ Tendaho**	**@ Logia Village**	**@ Adaitu**	**Melka Werer**
500	2665.980	975.409	1456.116	428.835
200	2181.192	840.265	993.253	401.230
100	1857.148	737.563	749.815	379.329
50	1565.298	634.335	571.167	356.462
20	1222.028	496.756	405.332	324.503
10	988.851	391.44	317.186	298.632
5	771.994	284.388	251.116	270.514
Return Period	**@ Mille Village**	**@ Dubti**		
500	1358.992	2709.54		
200	1031.929	2214.61		
100	834.312	1884.49		
50	671.085	1633.58		
20	497.430	1272.95		

10	391.052	1030.53
5	300.741	807.836

4.3 HEC-RAS Model Computation

Geometric data

Using the RAS Geometry menu in the Ras Mapper inside the HEC-RAS model, river geometry parameters such as stream centerline, bank line, flow route line, and XS cut lines were recovered from the topographic terrain model or from the TIN. While the river geometries were drawn from upstream to downstream along the river centerline, the XS cut line was drawn across the river centerline at an arbitrary distance from upstream to downstream. Delineating the river cross-section in the model requires careful attention to detail and is a hard process that takes time. It is highly advised to consider the appropriate value of Manning's roughness coefficient n while measuring the precise water surface elevation, due to its remarkable significance. One of the best criteria for value consideration is the description of the river channel. This includes canals that are dug, lined, and formed naturally (Namara et al., 2022). Accordingly, the manning's roughness coefficient for was assigned 0.06, 0.03, and 0.04 for the left channel, river bottom channel, and right channel.

Flow Data

For this investigation, a 1-D steady-state flow condition was used. The maximum flood quantile for return times of 5, 10, 20, 50, 100, 200, and 500 has previously been developed above. The necessary steady flow data are entered for the HEC-RAS simulation once all geometric data have been entered. A 1D steady state is chosen for modeling in consideration of the needed model outputs, the degree of detail, and the anticipated accuracy of the outcomes. The simplest to utilize and comprehend the outcomes of are 1D steady flow models. It is necessary to enter the flow regime to be selected, the number of profiles to be calculated, and the boundary conditions. The selected flow regime is sub-critical, characterized by comparatively deep depths and slower velocity.

4.4 Calibration and Validation of HEC-RAS Model

After the successful simulation of the HEC-RAS 1D steady flow model, the model was calibrated using the two tributary river water level data namely; Mille River and Logia River.

4.4.1 Calibration

Quantile Water level for Mille River

In accordance with Chow's (1959) advice, the river channel Manning's roughness coefficient (n) was adjusted to range from 0.03 to 0.043 to calibrate the Mille and Logia stations' water surface elevation. To evaluate the impact, NSE, PBIAS, and R2 were used. As shown in Appendix B, Appendix C1, and C2 n value was varied as 0.03, 0.035, 0.040, and 0.043 for Mille and Logia station.

When creating a hydraulic model for mapping flood inundation and flood forecasting, channel roughness is a crucial component to consider. The features of the channel roughness affect the discharge, river stage, and other hydraulic qualities, which are all related. When studying open-channel flow, especially in hydraulic modeling, the estimation of the channel roughness parameter is crucial. A lot of variables, including surface roughness, vegetation, abnormalities in the channel, and channel alignment, affect channel roughness. Several researchers including (Farooq et al., 2019; Namara et al., 2022; Tamiru & Dinka, 2021; Trambadia et al., 2023) have adjusted the roughness of the channels in several rivers in order to construct the hydraulic model.

Table 4. 9 Calibration result of both Mille and Logia River Water Surface Elevation (Water level)

Calibrated Results for Mille River station 22400				
Manning's N	**R^2**	**NSE**	**PBIAS (%)**	
0.03	0.8785	0.714273	-7.200516629	
0.035	0.8552	0.469832	-11.03487246	
0.04	0.8588	0.222961	-14.1830804	
0.043	0.8576	0.044537	-16.03971585	
Calibrated Results for Logia River station 21600				
Manning's N	**R^2**	**NSE**	**PBIAS (%)**	

0.03	0.8576	0.755333	1.384083045	
0.035	0.8583	0.753423	-0.787749393	
0.04	0.8588	0.686941	-2.554663918	
0.043	0.8562	0.620311	-3.511742619	

Table 4. 10 performance criteria for model calibration and validation (Tamiru & Dinka, 2021)

Goodness of fit	**NSE**	**PBIAS**	**R2**
Very good	$0.65 < NSE \leq 1.00$	$PBIAS < \pm 15$	$0.65 < R2 \leq 1.00$
Good	$0.55 < NSE \leq 0.65$	$\pm 15 \leq PBIAS < \pm 20$	$0.55 < R2 \leq 0.65$
Satisfactory	$0.40 < NSE \leq 0.55$	$\pm 20 \leq PBIAS < \pm 30$	$0.40 < R2 \leq 0.55$
Unsatisfactory	$NSE \leq 0.40$	$PBIAS \geq \pm 30$	$R2 \leq 0.40$

Based on the aforementioned parameters, the manning coefficient for the Mille and Logia River major channels has been determined to be "n" = 0.03. Additionally, water level quantiles for the return periods of 5, 10, 20, 50, 100, 200, and 500 years have been computed using the observed water level data for the Mille River daily data from the years 1999–2018 and Logia River (2000–2019). And the water level simulated in HEC-RAS for the flood quantiles of both rivers calibrated with the ground based observed data. Finally, the Performance of the model examined NSE, PBIAS, R2 give of values 0.714273 (Very Good), -7.200516629 (Very Good), 0.8785 (Very Good) respectively for Mille river. And NSE, PBIAS, R2 give of values 0.755333 (Very Good), 1.384083045 (Very Good), 0.8576 (Very Good) respectively for Logia River.

A shape file depiction of the flood plain was made using the river geometries that run along it. These river geometries were extracted from the high-resolution DEM using RAS mapper. The HEC-RAS model integrated flow data with the flood plain shape file to produce a plan view of the flood plain. As shown in Figures 4. 7, 4. 8, and 22400 for Mille River Station and 21600 for Logia River Station, respectively, the rating curve for different flood quantiles discharge was developed.

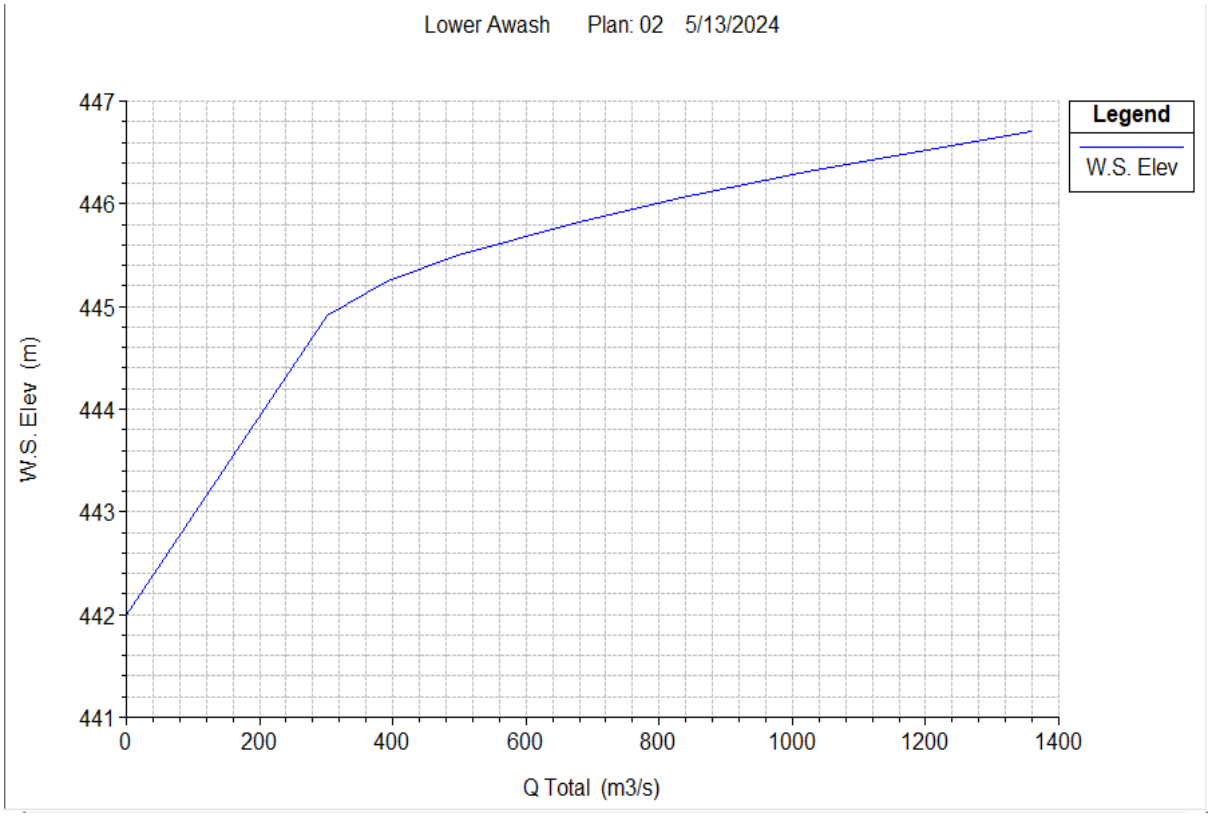

Figure 4. 7 Rating curve of Mille River Station 22400

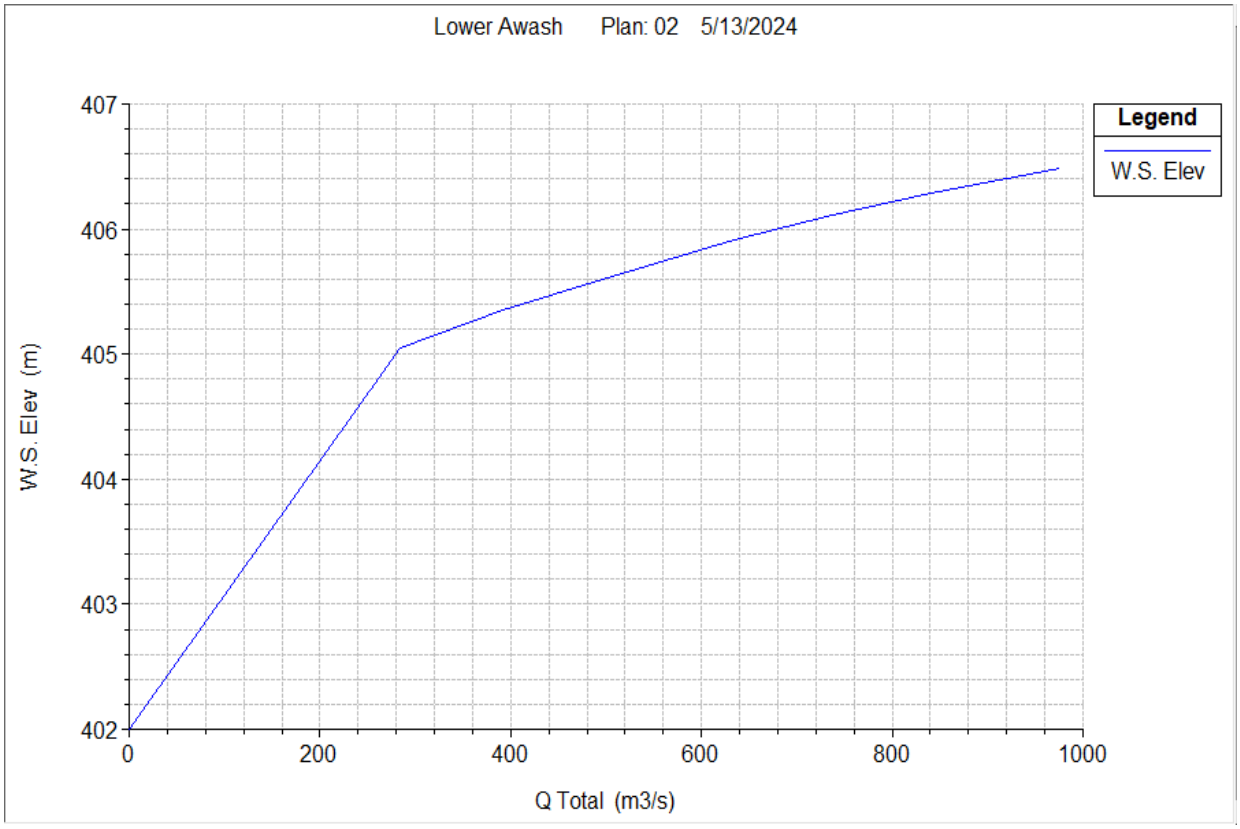

Figure 4. 8 Rating curve of Logia River station 21600

4.4.2 Validation

Calculating the percentage of overlapped area between the water bodies defined in NDWI, MNDWI, and HEC-RAS software was done using the intersect tool in the Analysis toolbox of ArcGIS (ver. 10.8). After converting the raster formats of the three results (NDWI, MNDWI, and HEC-RAS) into vectors (polygons) using a conversion tool, the pertinent shape areas were calculated using ArcGIS's geometry computation features. The percentage of overlapped regions was calculated after both polygons were remapped to the same geographic coordinate system Adindan UTM Zone 37 N (Tamiru & Dinka, 2021).

Overlapping percentage (%) = $\frac{\text{Layer 1 (Km2)}}{\text{Layer 2 (Km2)}}$ Layer 1 is the area of the water body delineated in NDWI from flood events and Layer 2 is the area of the inundation map generated in HEC-RAS.

Table 4. 11 Specification of Landsat 7 (Deoli et al., 2022)

Band Name	**Band Number**	**Resolution (m)**
Blue	1	30
Green	2	30
Red	3	30
Near Infrared (NIR)	5	30
Short-wave Infrared 1 (SWIR 1)	5	30
Short-wave Infrared 2 (SWIR 2)	7	30

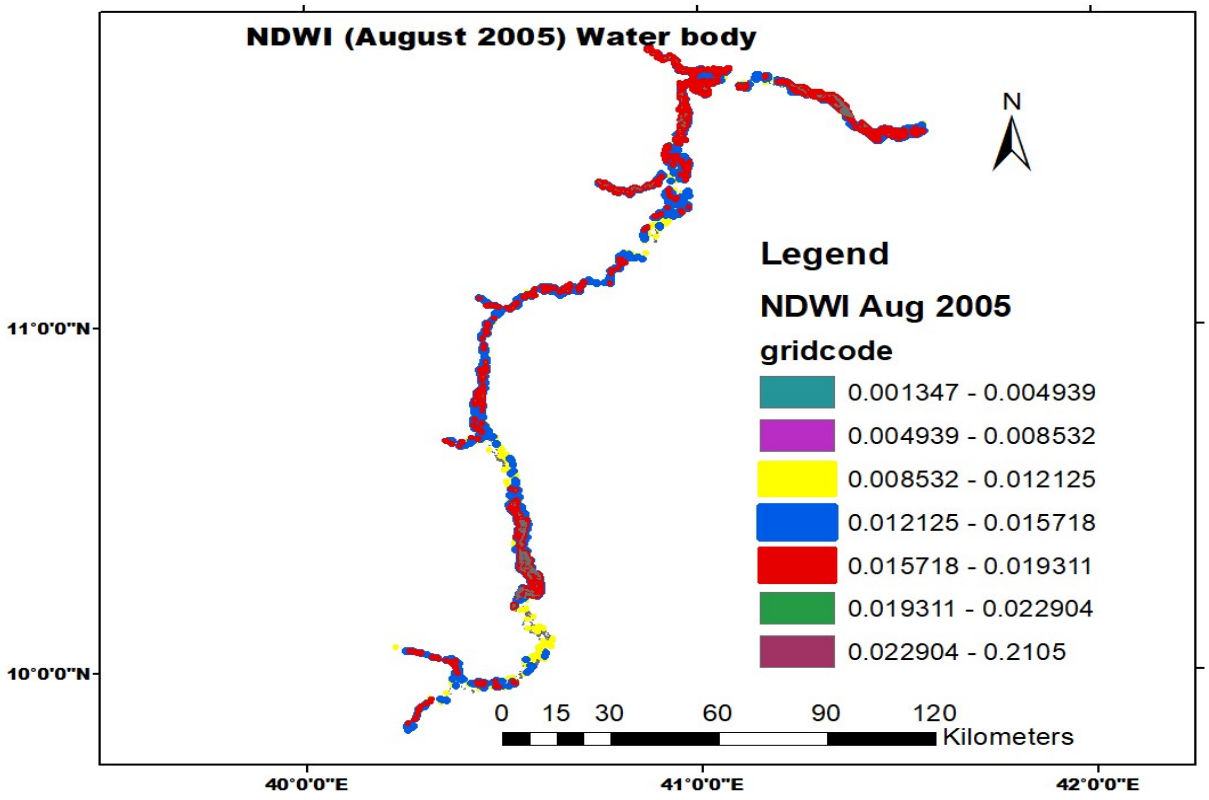

Figure 4. 9 NDWI calculated from satellite image in August 2005

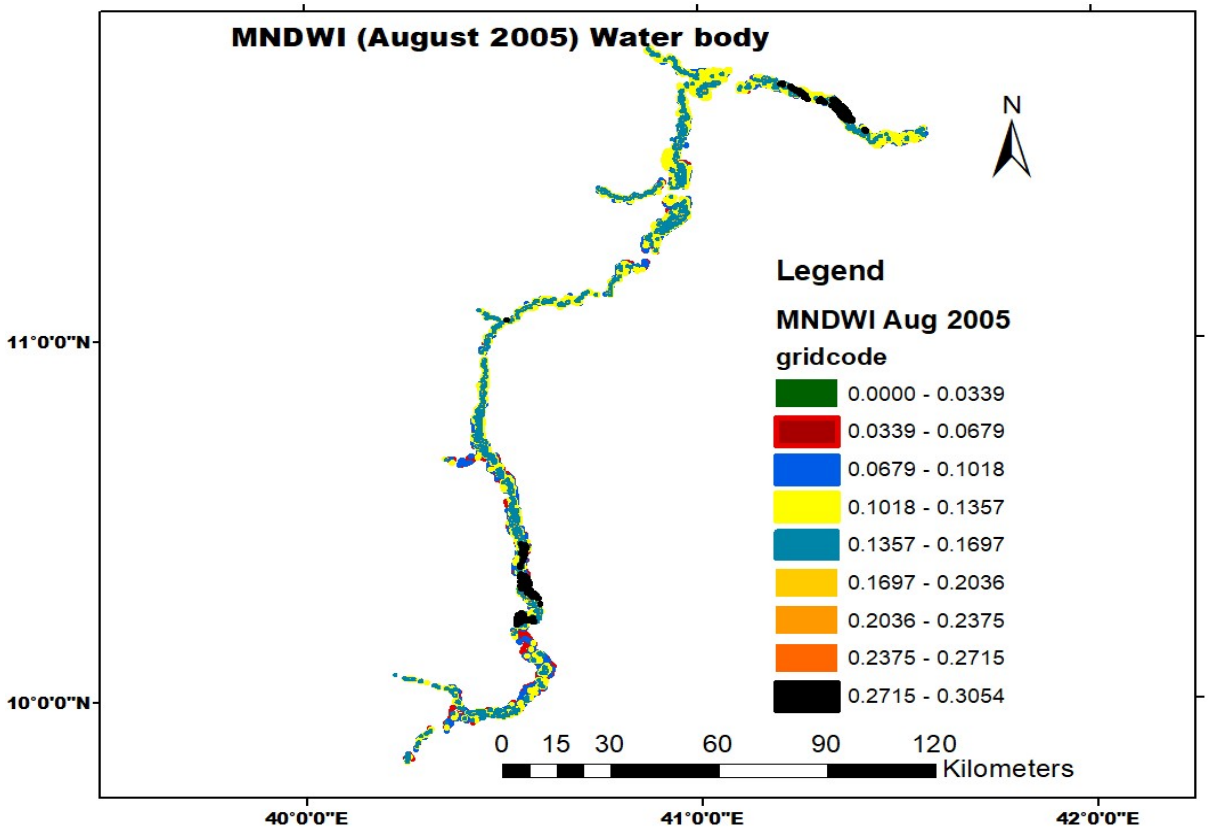

Figure 4. 10 MNDWI calculated from satellite image in August 2005

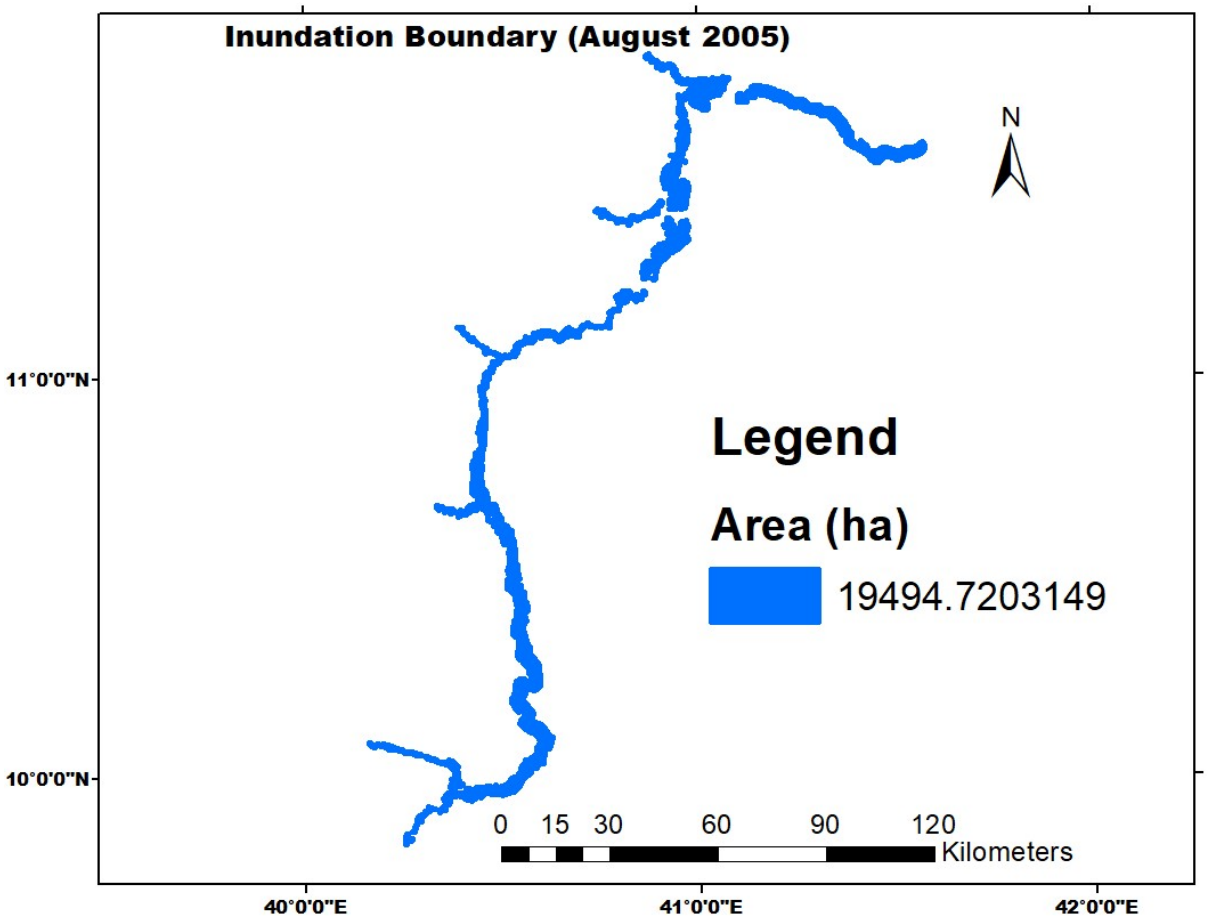

Figure 4. 11 Inundation boundary for the year August 2005

Table 4. 12 Validation Results

	Layers	**Areas (ha)**	**Overlapping Percentage (%)**	**Goodness of fit**
1	Inundation boundary	19494.72031		
2	NDWI	15202.62	77.98326806	Not good
3	MNDWI	17295.48	88.71879012	Good Agreement

Tamiru and Dinka (2021) conducted a study wherein the inundation map was assessed on the basis of overlapping areas. A percentage of overlap exceeding 85% was deemed to be in good agreement. Therefore, the validation result of MNDWI has agreement with model results of overlapping percentage 88.71879% as shown in above table 4. 12.

4.5 Flood Hazard Assessment

When determining the flood hazard in the model region, the severity of the flood for each flood scenario was taken into account. We reasoned that a higher flood hazard would follow a higher flood intensity in the inundated. Identification of regions with a chance of flooding for a specified return period is known as flood hazard mapping. Flood velocity and inundated depths are two hydrological parameters that affect the degree of flood hazard. Based on inundation depth classes corresponding to flooded depths, the degree of flood hazard was divided into hazard categories (Ongdas et al., 2020; Ukumo et al., 2022; Vojtek & Vojteková, 2016).

4.5.1 1D HEC-RAS Model Flood Inundation and Hazard Assessment

Two processes were utilized to construct flood danger maps: post-RAS processing and HEC-RAS. A simulation that examined the extent, depth, and velocity of the inundation during a flow with return periods of 5, 10, 20, 50, 100, 200, and 500 years was conducted using the calibrated and verified model. As shown in Figures 4.12 and 4.13, the 1D HEC-RAS model for flood inundation and hazard assessment uses the results of inundation depth and flow velocity to determine the danger levels. The flood inundation area grows linearly with an increase in flood return times, as shown in Fig. 4.14, after the flood extents for 2, 5, 10, 25, 50, and 100-year return periods were analyzed. As seen in Table 4.13, these hazard levels are divided into five different groups. A Very Low hazard level is identified when the flood depth is less than 0.5 meters and the flow velocity is below 1 meter per second. A Low hazard level is defined by flood depths ranging from 0.5 to 1 meter and flow velocities between 1 and 2 meters per second. Medium hazard levels occur when flood depths are between 1 and 2 meters, accompanied by flow velocities of 2 to 3.8 meters per second. High hazard levels are characterized by flood depths of 2 to 5 meters and flow velocities ranging from 3.8 to 5.8 meters per second. Finally, an Extreme hazard level is indicated by flood depths exceeding 5 meters and flow velocities greater than 5.8 meters per second.

In addition, potential landcover damages for 2, 5, 10, 25, 50, and 100-year return periods were compared to the predicted flood extents in the model study region (Figure 4.19). Appendix D and E provided a detailed explanation and assessment of the flood-affected areas. The fact that range and agricultural land are frequently among the most impacted land uses emphasizes how susceptible these industries are to flooding. Additionally, the aforementioned landcover's vulnerability rises linearly in response to flood episodes.

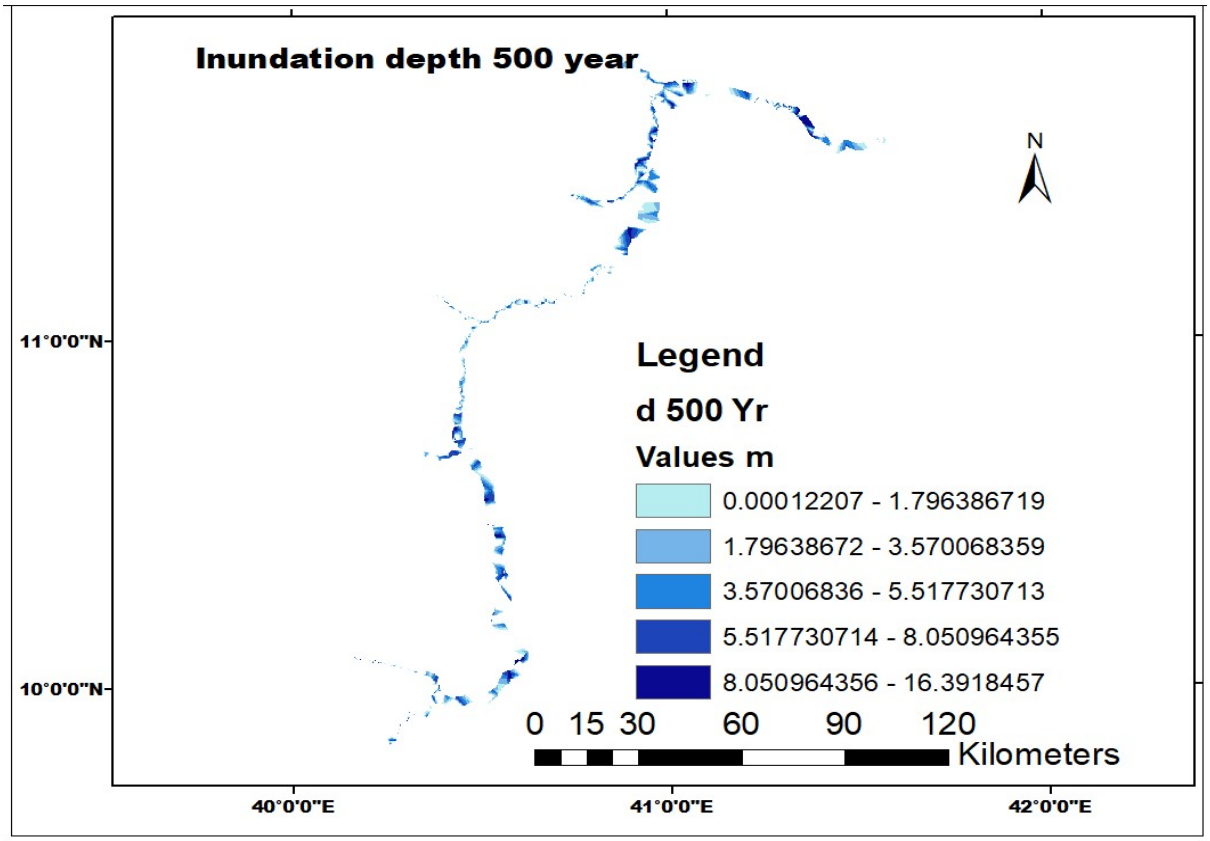

Figure 4. 12 Inundation depth 500 Yr.

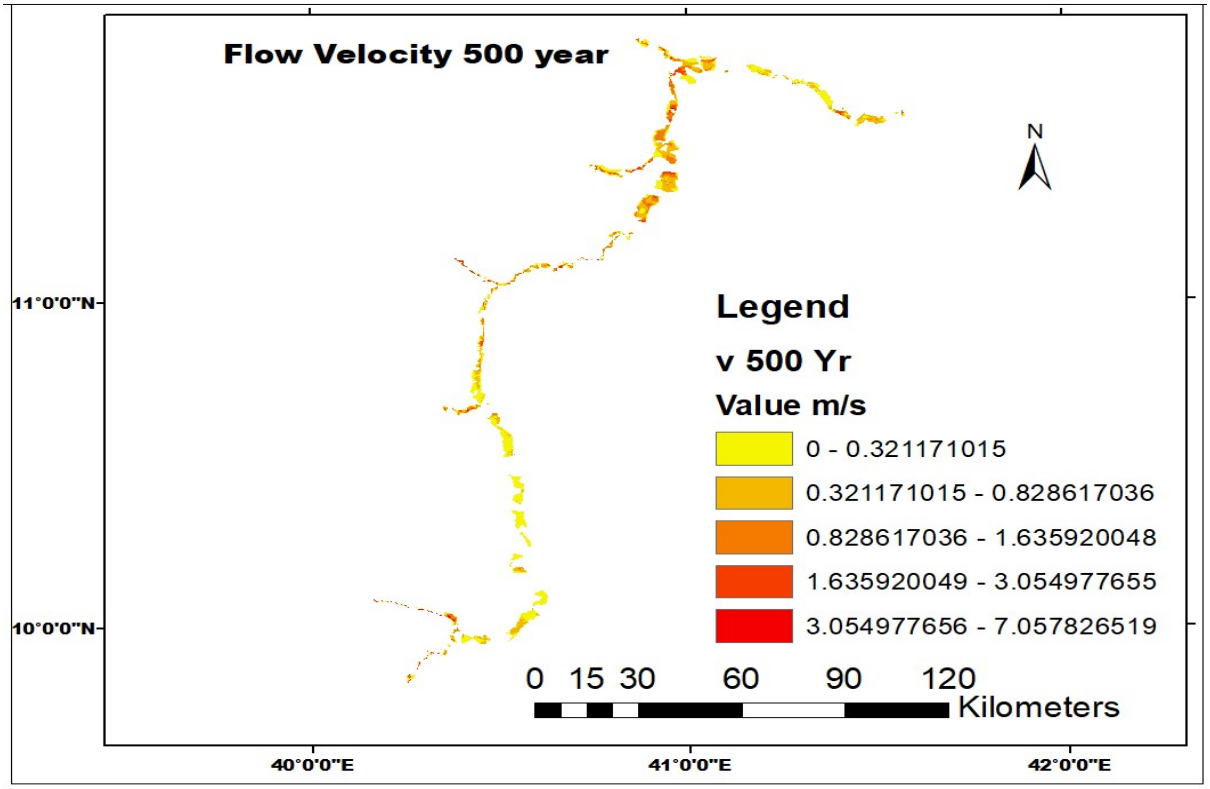

Figure 4. 13 Velocity map 500 Yr

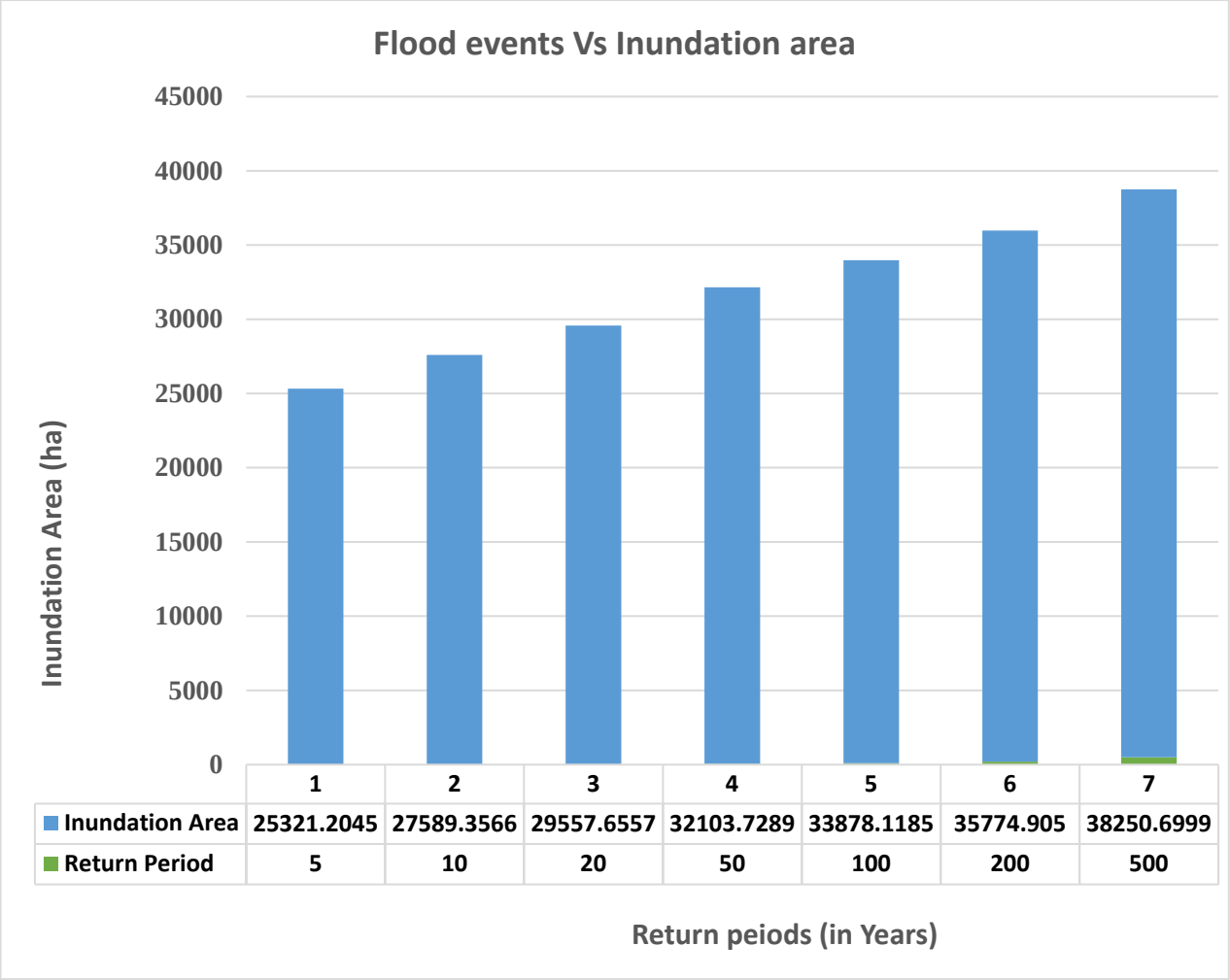

Figure 4. 14 Flood events Vs Inundation area

Table 4. 13 Flood hazard classification based on flood depth and velocity (Ahmad et al., 2022; Ongdas et al., 2020)

Hazard Level	Flood Depth (m)	Flow Velocity (m/s)
Very Low	<0.5	<1
Low	0.5 - 1	1- 2
Medium	1 - 2	2 -3.8
High	2 - 5	3.8 – 5.8
Extreme	>5	>5.8

After flood hazard classification identified, the hazard level map for all return periods (5, 10, 20, 50, 100, 200, 500) years were developed after post process of HEC-RAS 1D results and the generated maps were uploaded on Appendix H.

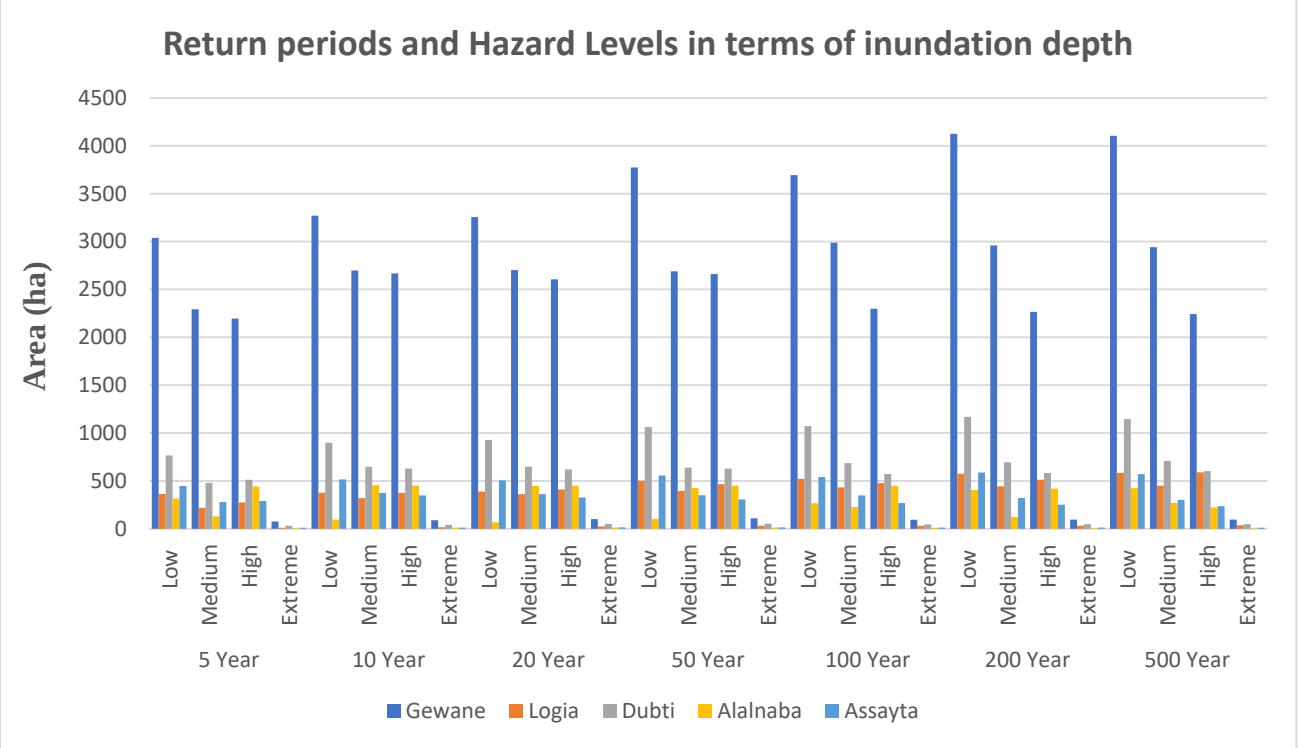

Figure 4. 15 Flood affected areas and Hazard Levels for different return periods in case of inundation depth

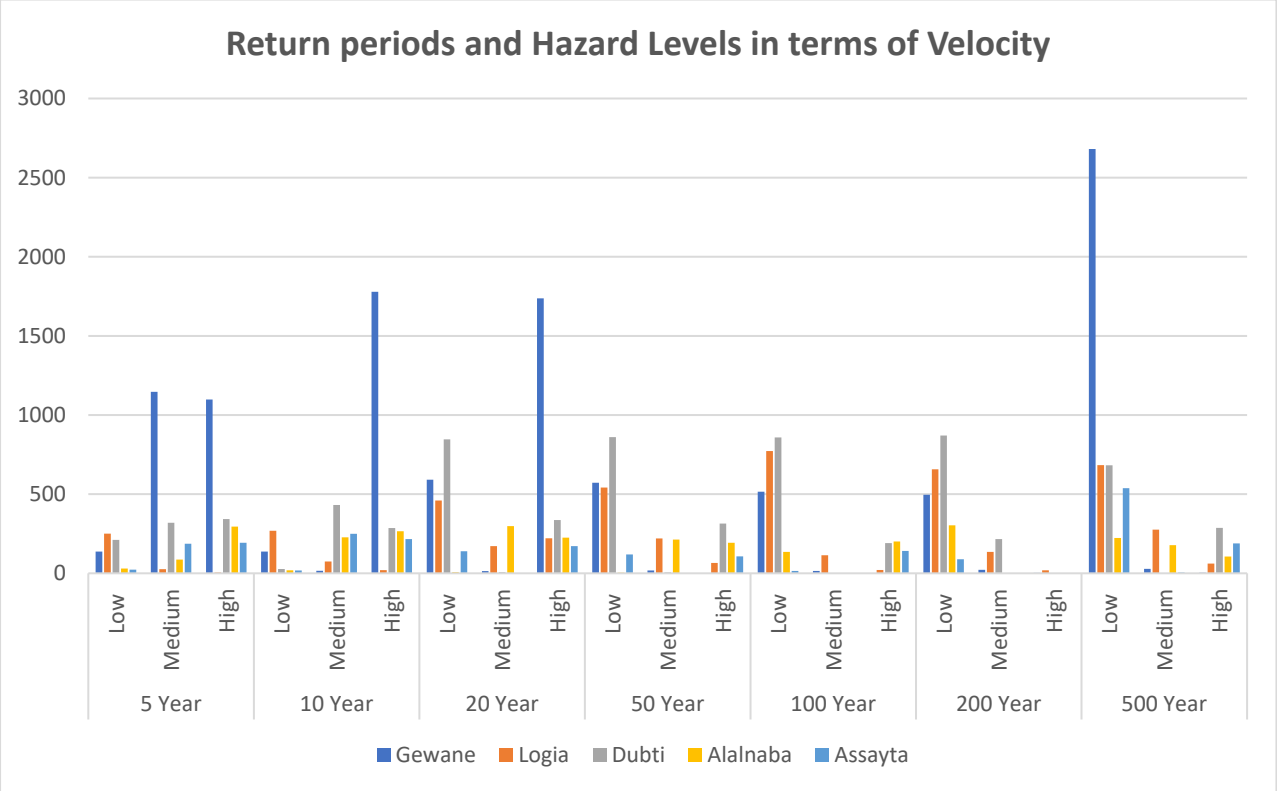

Figure 4. 16 Flood affected areas and Hazard Levels for different return periods in case of Velocity map

After identifying the inundation depth and velocity of the flood in bar graph shown in Figure 4.17, 4.18, we compared these flood hazard factors (depth and velocity) across different hazard levels: low, medium, and high. We then analyzed the area impacted by each hazard level and calculated the percentage change in these areas. Hazard impacts in terms of depth by passed the hazard level of Velocity of impacts in area (hectares). Finally, we assessed the affected land use and land cover based on the area coverage of the inundation depth, expressed in hectares.

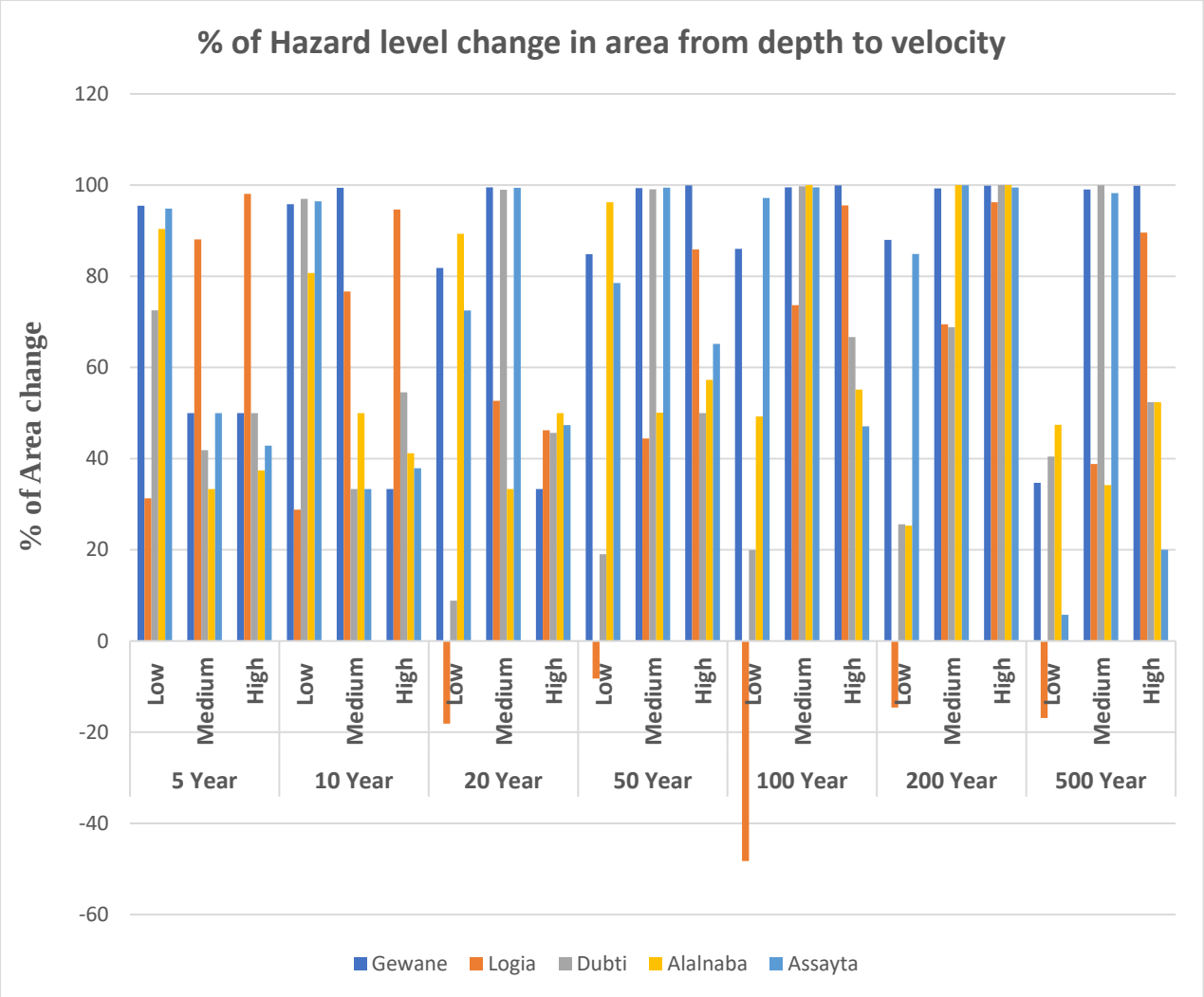

Figure 4. 17 Percent of Hazard level change in area from depth to velocity.

From the Figure 4.19 shown above the percent area change for all hazard levels (Low, Medium, High) shows; the hazard impact from hazard factor depth is highly advanced than velocity factor for all hazard levels except 20-year, 50-year, 100-year, 200-years, and 500-year low hazard level. Therefore, using this baseline decision; the hazard affected land use land cover was assessed using area of inundation depth as stated below in the Figure 4.20. Moreover this, tabular explanation of affected LULC was explained on **Appendix F**.

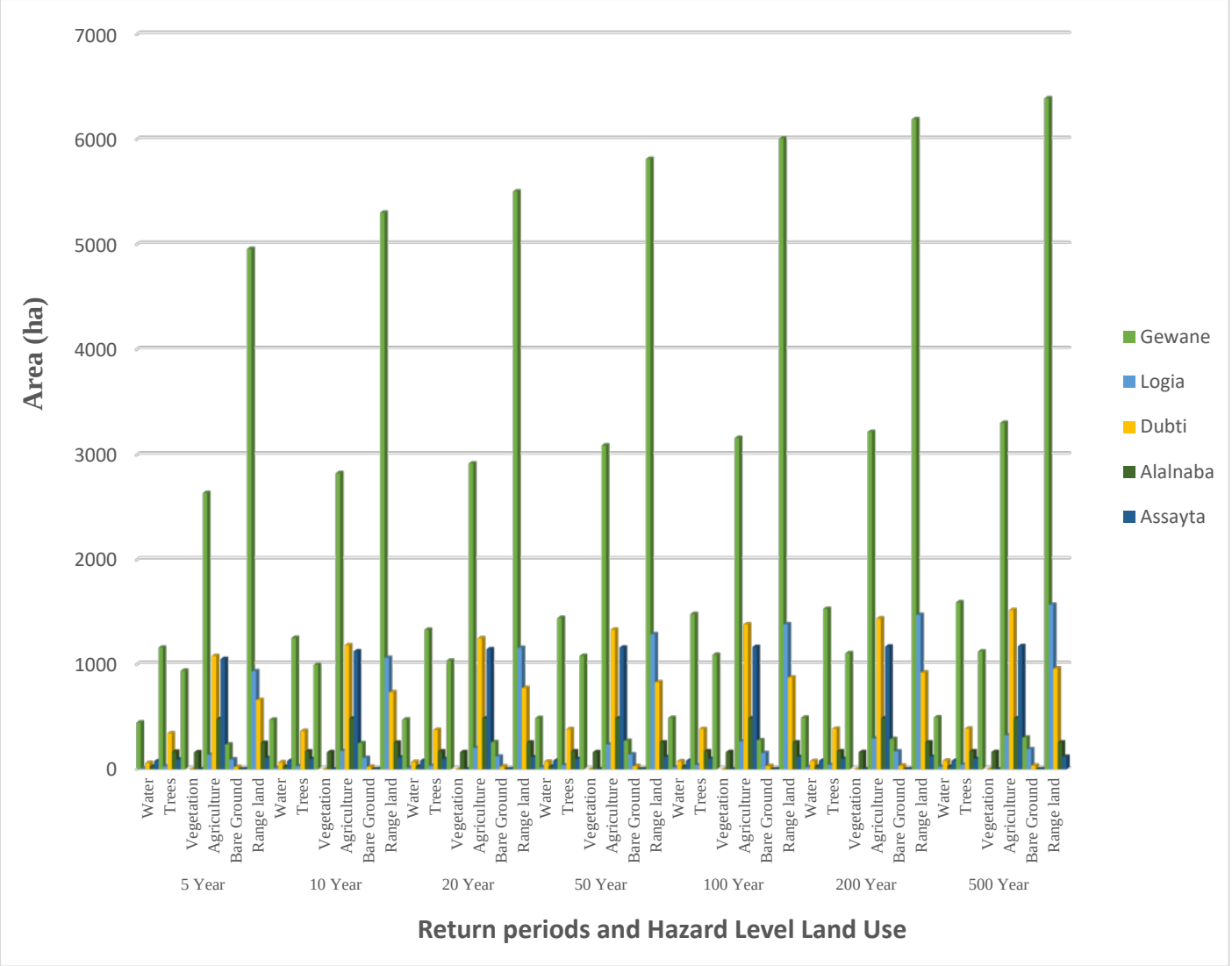

Figure 4. 18 Flood affected areas and Hazard Levels for different return periods in terms of Land use Land cover

4.5.2 2D HEC-RAS Model Flood Inundation and Hazard Assessment

In this study for 2D analysis; a total of 339309 cells were constructed over the 2D river flow region within the river reaching a length of 504.53 km for the main Awash River and 635.5 km including tributaries. Using imported topography data, the geometry editor was used to generate the 2D flow region. 100 m × 100 m cells with a calculation time interval of 10 s and an output interval of 24 hours were employed for the analysis. Smaller time intervals and cell sizes yield better results, even though the simulation takes longer to complete. for the unstable flow analysis of HEC-RAS. Based on these hypotheses, HEC-RAS will fill the mesh until the warmup phase and then use the full river cells and diffusion wave equation to simulate open channel flow while accounting for the finite volume approximation. It is necessary to assign the hydraulic attributes of each cell before performing analysis in HEC-RAS. Every calculated

cell mesh can have its hydraulic properties created by HECRAS. These hydraulic values are derived from manning's n-value land cover grid and the given geometric topography data (Bhandari et al., 2017). Figure 4. 12 displays the given cell attributes represented. The shown cell number is 241881, and 0.045 is Manning's n value assigned to that cell. For that cell, the figure also displays the correlations between area, perimeter, manning, face conveyance, elevation, and face profiles.

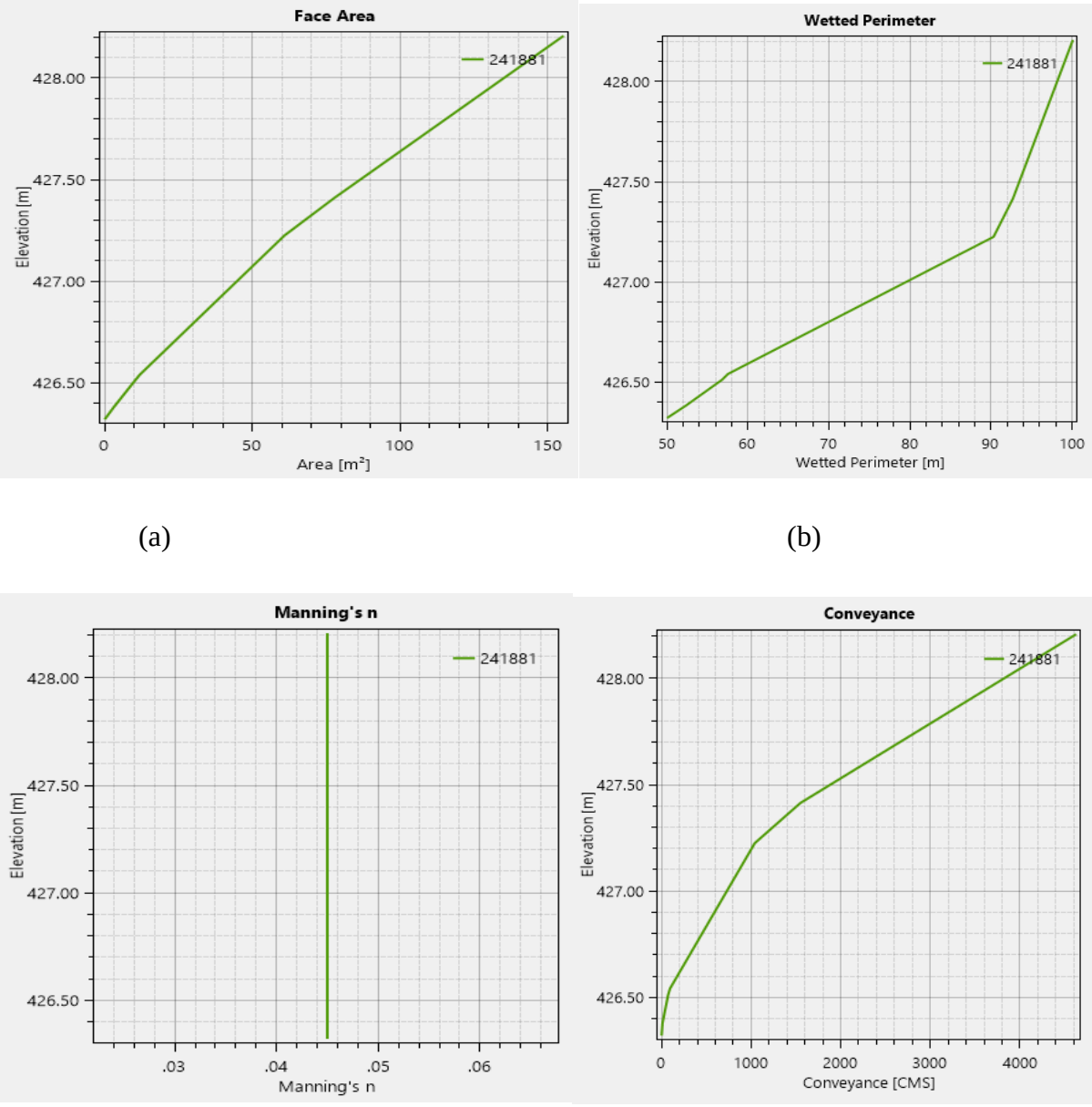

(a) (b)

(c) (d)

Table 4. 14 Representation of hydraulic properties created within HEC-RAS. Elevation vs. Area (a), Elevation vs. wetted perimeter (b). elevation vs. manning's coefficient (c). elevation vs conveyance (d).

The time variation of the unsteady flow analysis result was derived from the HEC-RAS study. Although the location of each result's maximum value varied across the reach of time, it was discovered that the water depth, water velocity, and water surface elevation within the time series were all at their highest when there was maximum flow. The HEC-RAS 2D simulations for the Mille River profile indicate a maximum depth of 5.75 meters at river station 1331.543 meters, based on the annual maximum series flow hydrograph (Figure 4. 12). Similarly, for the Logia River profile, the simulations show a maximum depth of 4.82 meters at river station 2211.872 meters (Figure 4. 13).

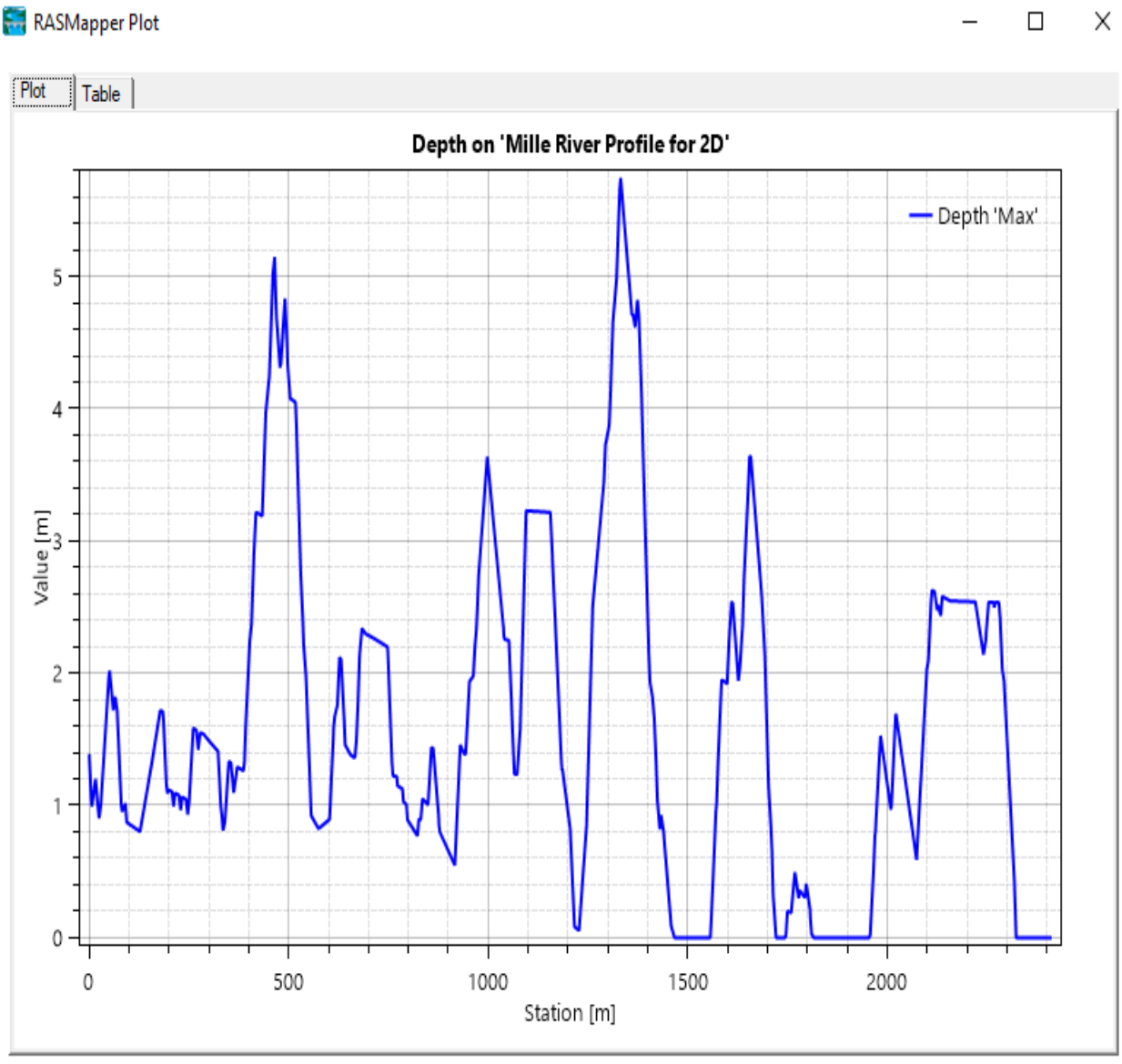

Figure 4. 19 Maximum depth on 2D Mille river profile

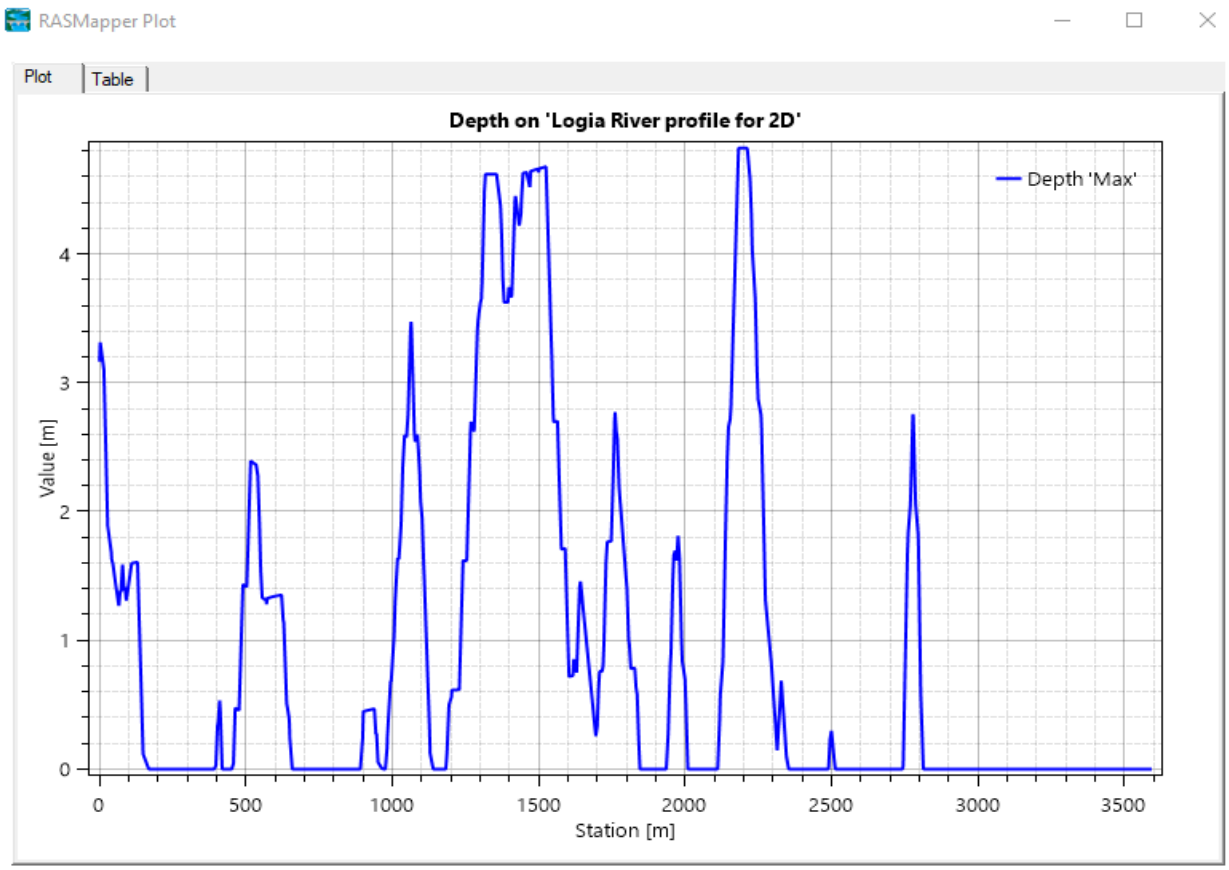

Figure 4. 20 Maximum depth on 2D Logia river profile.

After successful run of 2D HEC-RAS model, the flood inundation mapping was developed. Then hazard map and hazard level were developed as per land use land cover of the inundated area. Here also in 2D results the same process was held as stated in Table 4.16, 4.17 below. For this both hazard factors (depth and velocity) were assessed to determine hazard level for the flood affected areas.

Table 4. 15 Affected areas and Hazard level from 2D inundation depth

Affected Area	**2D Hazard Level in Area (ha)**			
	Low	**Medium**	**High**	**Extreme**
Gewane	783.125	399.1719	233.5625	9.953125
Saa	67.3594	50.42188	57.71875	17.45313
Adaytu	549.031	478.8281	638.1094	80.14063
Logia	762.922	685.8594	853.7344	67.8125
Dubti	783.125	399.1719	233.5625	9.953125
Asayta	140.234	48.76563	17.95313	0.125

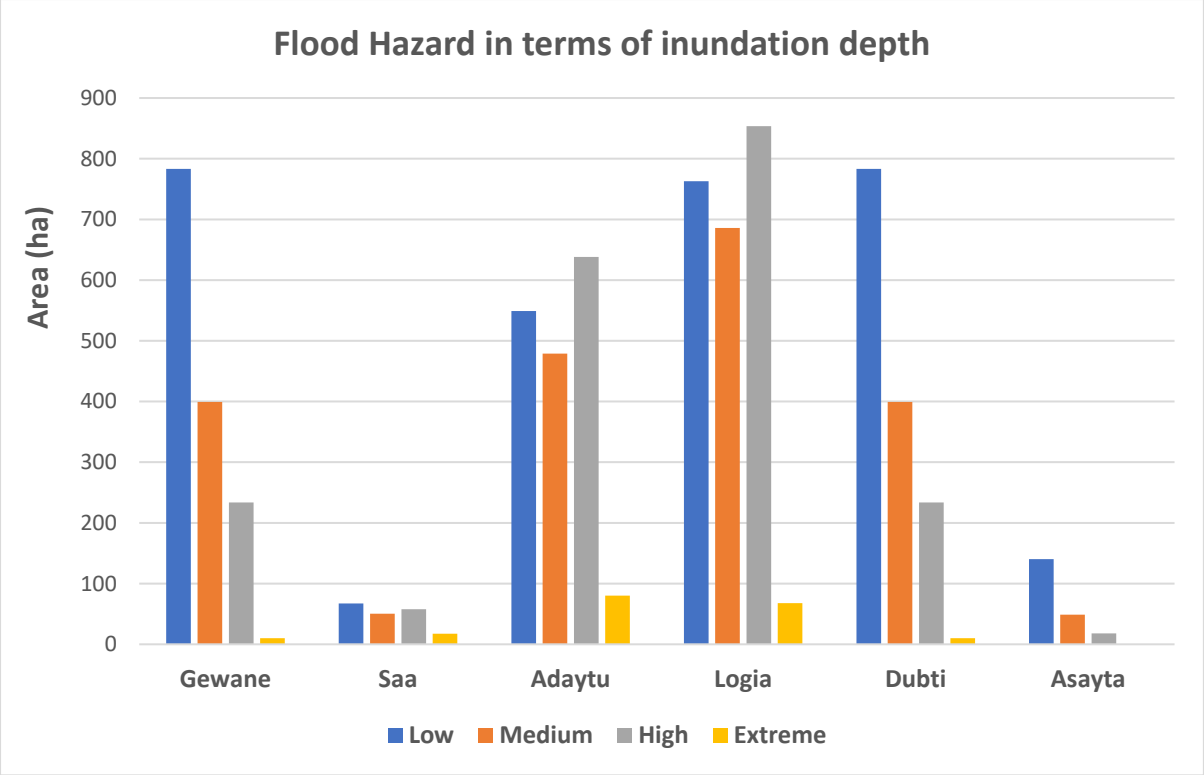

Figure 4. 21 2D flood hazard level of affected areas in bar graph in terms of inundation depth.

Table 4. 16 Affected areas and Hazard level from 2D flow velocity

Affected Area	**2D Hazard Level in Area (ha)**		
	Low	**Medium**	**High**
Gewane	474.621	324.53	141.5530303
Saa	28.5156	5.234375	38.47916667
Adaytu	747.266	94.82813	303.8616071
Logia	571.578	20.96875	652.1038611
Dubti	219.766	6.046875	129.0400552
Asayta	81.5316	25.39876	10.43786337

After flood hazard level was separated for affected areas, the land use land cover for the areas were assessed.

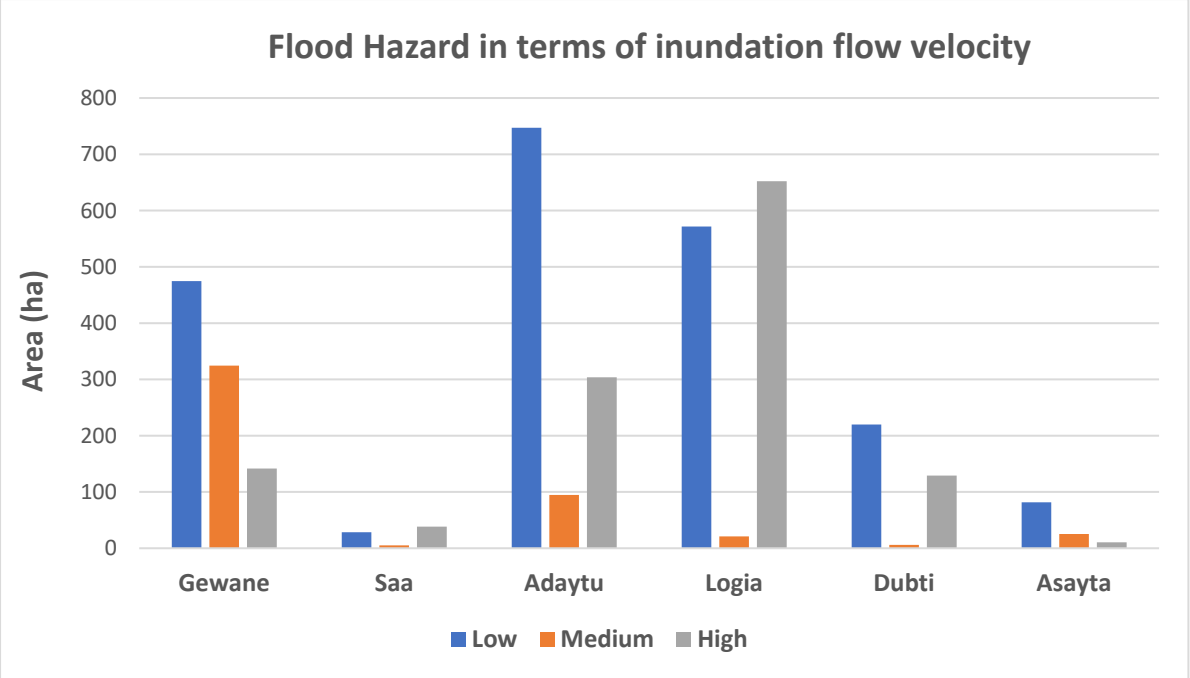

Figure 4. 22 2D flood hazard level of affected areas in bar graph in terms of flow velocity.

From Table 4.15, 4.16 and Figure 4.21, 4.22 the area change was analyzed. During the analysis, the area of hazard level obtained from the inundation depth surpasses the hazard level of flow velocity as shown in Figure 4.23. Moreover, hazard map was provided and availed for post process of 2D HEC-RAS results on Appendix H

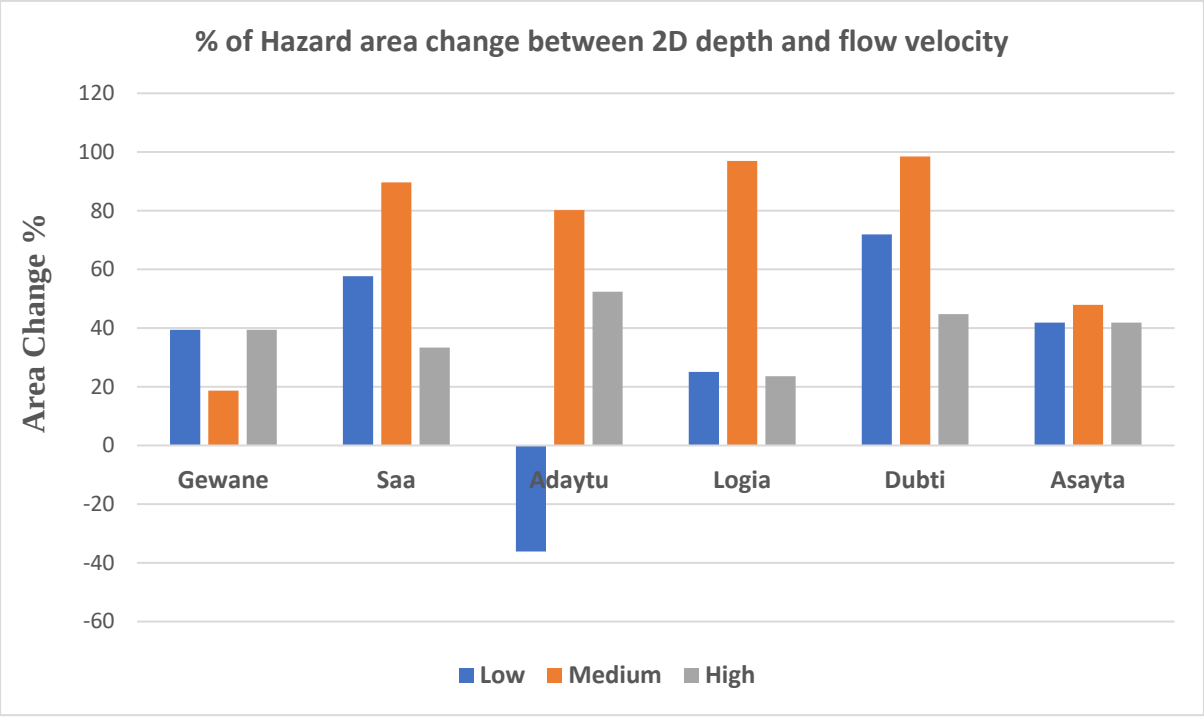

Figure 4. 23 Percent of area change bar graph between 2D depth and velocity.

Table 4. 17 Flood Affected Land Use Land Cover from 2D inundation depth results

Affected Area	2D Area of Hazard Level in Land Use land Cover (ha)					
	Water	Trees	Vegetation	Agriculture	Bare Ground	Range land
Gewane	819.0937045	695.1736141	4.382295896	140.4467515	1.044426299	255.7258158
Logia	50.205135	32.89095387	-	922.3345695	123.825349	1699.006378
Dubti	41.7988536	9.398498017	-	1743.766306	21.224031	560.4741766
Adaytu	90.9210423	384.2308585	-	194.6437919	178.014578	1409.036377
Assayta	-	-	20.3903432	408.3363193	0.20979815	0.109893926
Sa'a	22.63252399	8.459829374	0.467778132	-	57.36758104	115.1830261

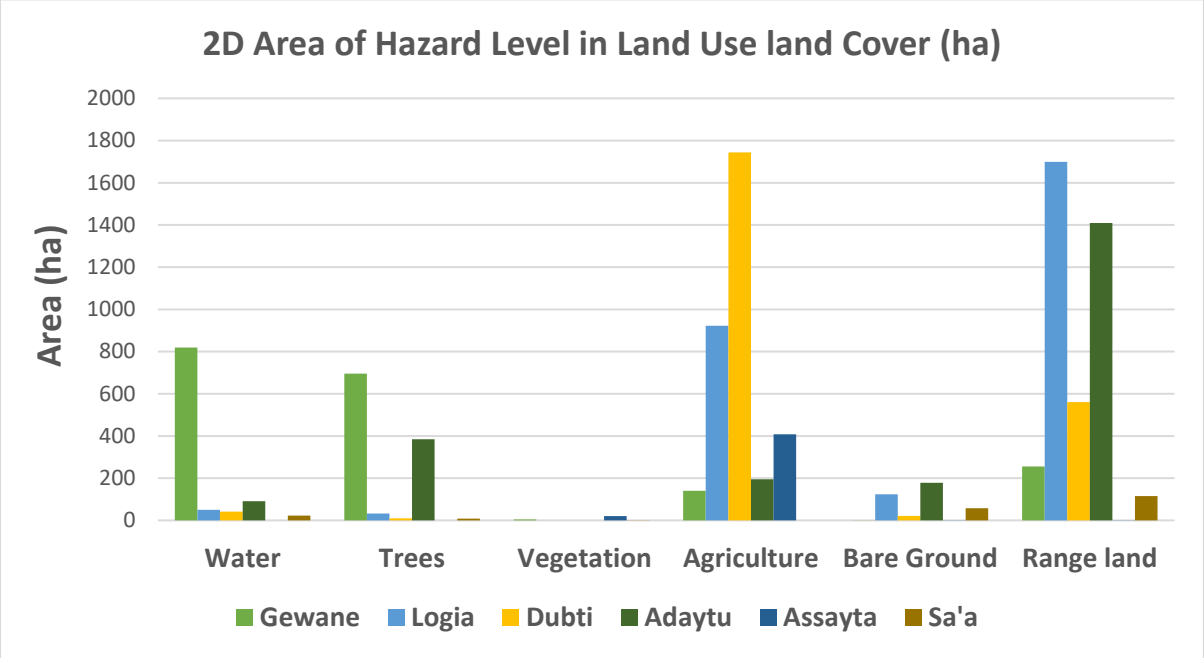

Figure 4. 24 Flood Affected Land Use Land Cover from 2D inundation results in bar graph

4.6 Flood Inundation mapping Using Google Earth Engine and Hazard Assessment

This flood mapping project utilized Google Earth Engine (GEE) to identify flooded areas. The first step involved defining the study area using a shapefile from 2D perimeter of HEC-RAS. Next, Sentinel-1 data for the desired timeframe (pre-flood and post-flood) was loaded and filtered by specific characteristics. These scenes were then visualized as an RGB composite to highlight potential flood extent based on visual differences as shown in Figure 4.25 (a) and (b).

To improve data quality for further analysis, a speckle filter was applied to both scenes shown in Figure 4.26 (a) and (b).

Following this, a threshold value was determined based on the backscatter intensity distribution. Pixels exceeding this threshold in the post-flood scene, likely representing flooded areas, were identified in Figure 4.27. Additionally, geospatial data layers like water body masks were incorporated to exclude permanent water bodies from the flood area calculation shown in Figure 4.28 (a) and (b). Finally, the area covered by the identified flooded pixels was calculated, providing valuable insights into the extent of the flood event. It's important to note that this report offers a general overview. Specific details and accuracy assessments using reference data would be necessary for real-world applications. Figure 4.29 shows in console of the code; the final flooded area calculated. The code utilized for GEE analysis is available under the Appendix I, J, K, L, M, and N.

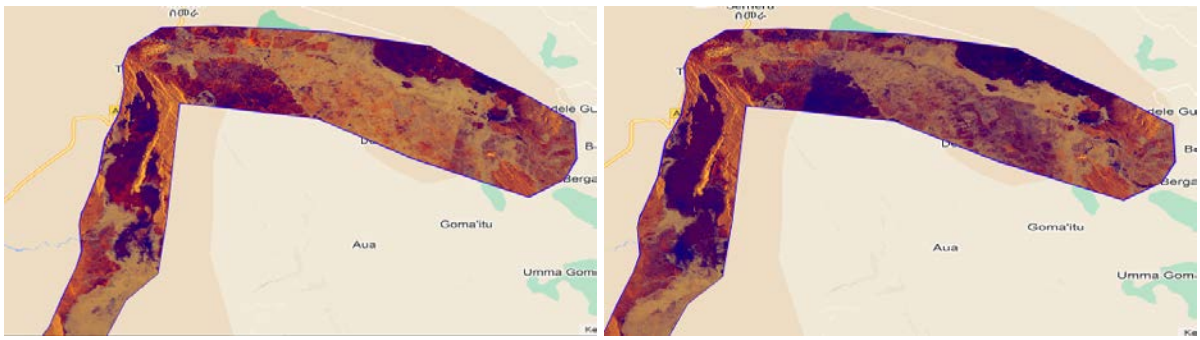

a) Before flood b) After Flood

Figure 4. 25 Before flood (a) and After flood (b)

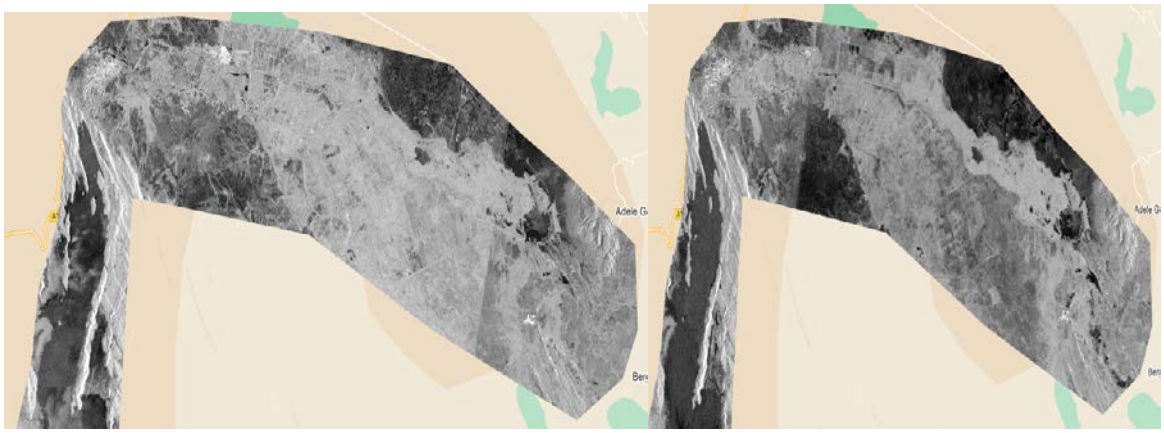

a) Before filter b) After filter

Figure 4. 26 Speckle filter

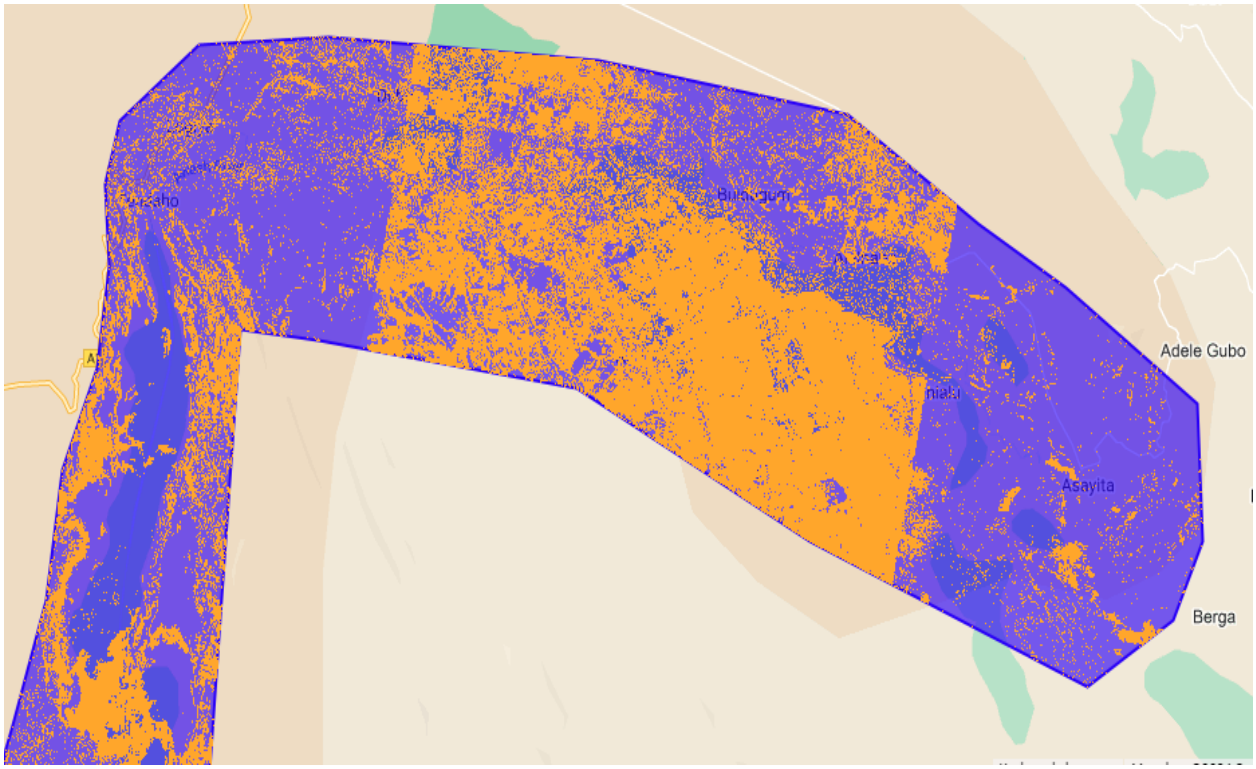

Figure 4. 27 Initial flooded area

a) Initial Flooded b) Final Flooded

Figure 4. 28 Apply Masks

Additionally, the complete codes which have been utilized in this study is available on GitHub repository for all codes that have been utilized in this study including Filling of missed hydrological data, Heterogeneity check and homogenization of hydrological data, and Flood mapping in GEE. Here is the link https://github.com/Eyoba94/Eyob-Repository/tree/main

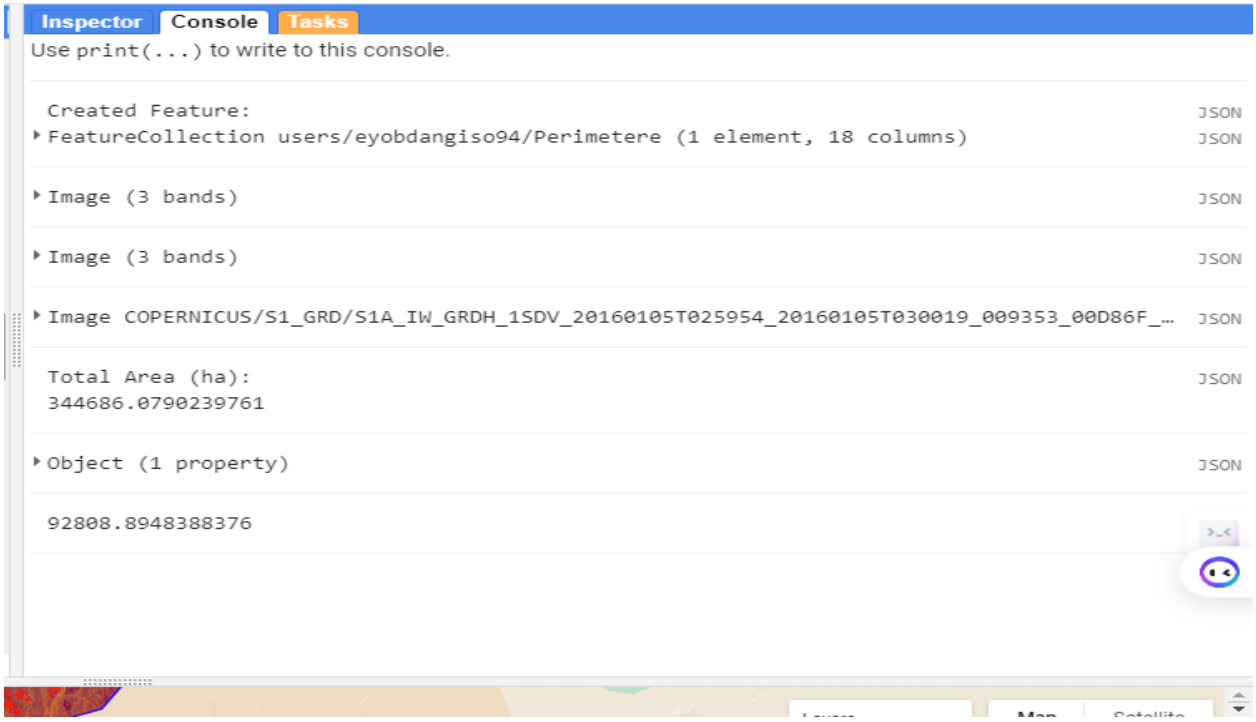

Figure 4. 29 Flooded Area in ha

4.6.1 Hazard Assessment From Google Earth Engine Flood Inundation Results

After successfully calculating final flooded area; hazard level was analyzed as per land use land cover of the areas. Table 4.18 below shows, the GEE inundation results and affected LULC for the flood affected areas according to their area of impacts. For detail explanation; the result map developed and processed in GIS after export of the inundation results was availed on Appendix O.

Table 4. 18 GEE Flood Affected Land Use Land Cover

Affected Area	GEE Hazard Level in Land Use land Cover (ha)					
	Water	Trees	Vegetation	Agriculture	Bare Ground	Range land
Gewane	55.083642	1260.624369	445.508567	1588.116281	175.293738	5283.945564
Logia	33.495861	45.822145	32.539471	2194.53099	1658.13309	3107.075452
Alalnaba	17.09978	338.373484	51.542915	3560.538478	919.292812	5659.627134
Dubti	42.260311	422.28874	-	7996.800625	1002.662594	5657.869069
Adaytu	45.477357	748.459828	55.129003	283.63443	1044.940367	7562.666474
Saa	43.594573	245.51286	29.916102	98.63406	5305.933992	12856.75246
Assayta	13.324327	597.63447	254.02886	1832.67687	47.874041	2673.794913

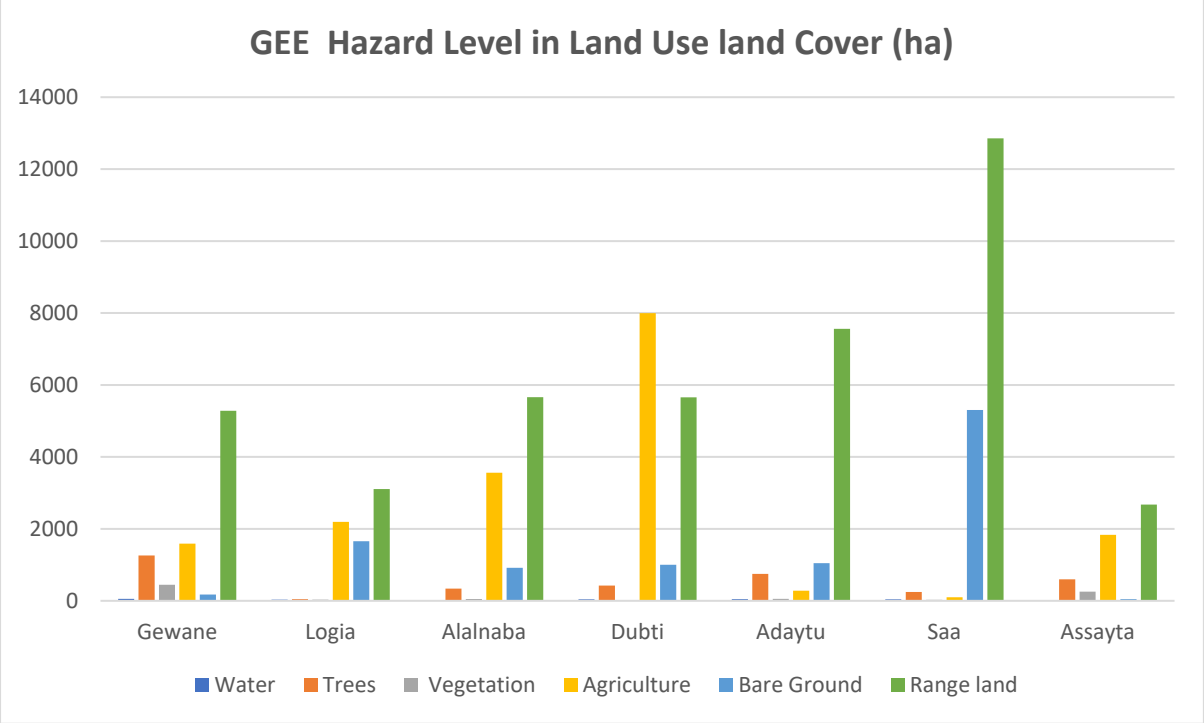

Figure 4. 30 GEE final Flood Affected Land Use Land Cover

4.7 Discussions

4.7.1 From 1D HEC-RAS Simulation Results

The inundation area (hectares) for different return periods is displayed in the chart found in Figure 4.14. The inundation area grows by 43% from a 5-year return period to a 500-year return period based on the data presented. The numbers for the inundation area for the 500-year return period are 38,250.6999126 hectares, and for the 5-year return period, they are 25,321.2044561 hectares.

Increase = (38,250.6999126 hectares - 25,321.2044561 hectares) / 23,773.2446 hectares * 100% = 51%

From the Appendix D shows 100-year return period the hazard level ranges from very low to extreme. Gewane is the most affected area with 2299 hectares under high hazard and 94.67 hectares under extreme hazard. Alalnaba is the least affected area with only 7.91 hectares under extreme hazard. 200-year return period, Similar to the 100-year return period, the hazard level ranges from very low to extreme. Gewane remains the most affected area, with 2266 hectares under high hazard and 95.61 hectares under extreme hazard. Alalnaba is again the least affected, with 5.77 hectares under extreme hazard. 500-year return period, the hazard level also ranges from very low to extreme in this return period. Gewane is still the most affected area, with 2243 hectares under high hazard and 96.31 hectares under extreme hazard. Alalnaba has the least extreme hazard area, at 4.70 hectares.

Return Period Impact: Generally, for all locations, the total area affected by flooding increases with a higher return period (5-year to 500-year). This indicates a larger area potentially experiencing flooding in more severe events.

Location Vulnerability: Gewane consistently has the largest total area affected across all return periods and hazard levels. This suggests Gewane might be the most flood-prone location.

Hazard Level Distribution: The data reveals variations in the dominance of different hazard levels across locations:

Gewane: Exhibits a significant area under high and extreme hazard throughout all return periods. Logia, Dubti, and Assayta Show a dominance of very low, low, and medium hazard areas compared to Gewane. This suggests they might be less susceptible to severe flooding events. Alalnaba Similar to the above three locations, Alalnaba might be less prone to severe flooding based on the data. However, further investigation into the reasons behind the specific distribution of hazard levels across return periods for Alalnaba might be helpful.

From Appendix F shows In Gewane, the affected areas for various land uses generally increase with longer return periods. For instance, the affected area of agriculture increases from 3163.16 hectares (100-year return period) to 3306.99 hectares (500-year return period), indicating a growing risk to agricultural land over time. Similarly, the affected areas of other land uses such as trees, vegetation, bare ground, and range land also demonstrate increasing trends across

different return periods. In Logia, Dubti, Alalnaba, and Assayta, similar patterns are observed, with the affected areas of different land uses showing upward trends as the return period extends. For example, in Logia, the affected area of trees increases from 39.86 hectares (100-year return period) to 43.15 hectares (500-year return period), indicating potential ecological impacts due to flooding over time.

Across all areas, agriculture and range land are consistently among the most affected land uses, highlighting the vulnerability of these sectors to flood damage. For instance, in Assayta, the affected area of agriculture increases from 1169.61 hectares (100-year return period) to 1176.71 hectares (500-year return period), indicating a growing risk to agricultural activities over longer return periods. Additionally, the affected areas of water bodies, trees, vegetation, and bare ground also show varying degrees of impact across different areas and return periods, reflecting the complex interactions between flood hazards and land vulnerability.

4.7.2 From 2D HEC-RAS Simulation Results

As shown above Table 4-15 Hazard Level Distribution A significant variation exists in the distribution of hazard levels across locations.

- **Gewane and Dubti:** Share a similar pattern with a dominance of very low and low hazard areas, followed by medium and high hazard. They also have the smallest areas under extreme hazard.
- **Saa:** Exhibits the highest area under extreme hazard (17.45 hectares) compared to other locations. However, the total area affected by flooding seems relatively low.
- **Adaytu:** Has the largest area under high hazard (638.11 hectares) and a significant area under very low hazard.
- **Logia:** Shows a more balanced distribution across hazard levels with a considerable area under high hazard (853.73 hectares) and medium hazard (685.86 hectares).
- **Asayta:** Has the lowest total area affected by flooding across all hazard levels.

Key Findings:

Significant Variation in Hazard Level Distribution: The distribution of flood hazard levels varies considerably across locations.

- **Gewane and Dubti (Potential Duplicate):** Share a similar pattern with dominance in very low and low hazard areas, followed by medium and high hazard. They also have the smallest areas under extreme hazard.
- **Saa:** Exhibits the highest area under extreme hazard (17.45 hectares) compared to other locations. However, the total area affected by flooding seems relatively low. Further investigation is recommended to understand the specific context of this high extreme hazard zone.
- **Adaytu:** Has the largest area under high hazard (638.11 hectares) and a significant area under very low hazard. This contrasting distribution warrants further exploration.
- **Logia:** Shows a more balanced distribution across hazard levels with considerable areas under high (853.73 hectares) and medium hazard (685.86 hectares).
- **Asayta:** Has the lowest total area affected by flooding across all hazard levels.

The provided data in Table 4- 17 presents the affected areas and land uses for different regions.

In Gewane, agriculture is the most significantly affected land use, with 140.45 hectares classified as being under hazard level, indicating a high vulnerability to flooding in these areas. Other land uses, such as water bodies, trees, and rangeland, also show notable affected areas, though these are smaller compared to the agricultural lands. Interestingly, the affected areas for vegetation and bare ground are relatively small, suggesting that these land covers are less impacted by hazards compared to agriculture.

In Logia, agriculture is the predominant affected land use, with 922.33 hectares under hazard level, highlighting the significant vulnerability of these areas to flooding. Additionally, rangeland exhibits a considerable affected area, indicating potential risks to grazing areas and natural habitats. Water bodies, trees, and bare ground also show affected areas, although these are smaller compared to the extensive impact on agriculture and rangeland.

In Dubti, agriculture is the most affected land use, with 1743.77 hectares classified as being under hazard level, underscoring the high susceptibility of these areas to flooding. Rangeland and water bodies also show notable affected areas, indicating potential risks to grazing areas

and aquatic ecosystems. Interestingly, there are no reported affected areas for trees and vegetation in Dubti, suggesting potential differences in land cover composition compared to other regions.

In Adaytu, agriculture and rangeland are the primary affected land uses, with substantial areas under hazard level for both. Trees and bare ground also show affected areas, though these are smaller compared to the extensive impact on agriculture and rangeland. Interestingly, there is no reported affected area for vegetation, suggesting potential differences in land cover In Assayta, agriculture is the most affected land use, with 408.34 hectares under hazard level, highlighting the significant vulnerability of these areas to flooding. There is also a small affected area for vegetation, indicating potential impacts on natural habitats. Notably, there is no reported affected area for water bodies, trees, and bare ground, suggesting potential differences in land cover composition or data availability.

In Sa'a, agriculture and rangeland are the primary affected land uses, with notable areas under hazard level for both. Water bodies and bare ground also show affected areas, although these are smaller compared to the impact on agriculture and rangeland. Interestingly, there is no reported affected area for trees and vegetation, suggesting potential differences in land cover composition or data availability.

4.7.3 From the results GEE

In Gewane, agriculture dominates the affected land use, with 1588.12 hectares under hazard level, indicating a significant vulnerability to flooding in these areas. Rangeland also shows a substantial affected area, highlighting potential risks to grazing areas and natural habitats. Trees, vegetation, and water bodies exhibit smaller affected areas compared to agriculture and rangeland, suggesting relatively lower impacts on these land covers.

In Logia, agriculture stands out as the most affected land use, with 2194.53 hectares under hazard level, underscoring the susceptibility of these areas to flooding. Bare ground also exhibits a substantial affected area, indicating potential impacts on soil surfaces and infrastructure. Trees, vegetation, and water bodies show smaller affected areas compared to agriculture and bare ground, suggesting relatively lower impacts on these land covers.

In Alalnaba, agriculture dominates the affected land use, with 3560.54 hectares under hazard level, highlighting the significant vulnerability of these areas to flooding. Rangeland also exhibits a notable affected area, indicating potential risks to grazing areas and natural habitats.

Trees, vegetation, and water bodies show smaller affected areas compared to agriculture and rangeland, suggesting relatively lower impacts on these land covers.

In Dubti, agriculture stands out as the most affected land use, with 7996.80 hectares under hazard level, underscoring the high susceptibility of these areas to flooding. Rangeland also exhibits a significant affected area, highlighting potential risks to grazing areas and natural habitats. Water bodies, trees, and bare ground show smaller affected areas compared to agriculture and rangeland, suggesting relatively lower impacts on these land covers.

In Adaytu, rangeland dominates the affected land use, with a substantial area of 7562.67 hectares under hazard level, indicating vulnerability to flooding in grazing areas and natural habitats. Agriculture also exhibits a significant affected area, highlighting risks to agricultural activities. Trees, vegetation, and water bodies show smaller affected areas compared to agriculture and rangeland, suggesting relatively lower impacts on these land covers.

In Saa, rangeland stands out as the most affected land use, with a large area of 12856.75 hectares under hazard level, underscoring the vulnerability of grazing areas and natural habitats to flooding in the region. Bare ground also exhibits a substantial affected area, indicating

potential impacts on bare soil surfaces and infrastructure. Trees, vegetation, and water bodies show smaller affected areas compared to rangeland and bare ground, suggesting relatively lower impacts on these land covers.

In Assayta, agriculture dominates the affected land use, with a significant area of 1832.68 hectares under hazard level, highlighting the vulnerability of agricultural areas to flooding in the region. Trees, vegetation, and rangeland also exhibit notable affected areas, indicating potential risks to natural habitats and grazing areas. Water bodies and bare ground show smaller affected areas compared to agriculture, trees, vegetation, and

4.7.4 Overall Discussions Regarding on the Results of 1D, 2D, and GEE

Flood hazard assessments are critical for effective disaster management and mitigation strategies. Hydrodynamic models, such as 1D and 2D HEC-RAS simulations, provide detailed insights into flood dynamics, including water depth, flow velocity, and the spatial extent of flooding. On the other hand, Google Earth Engine (GEE) offers a powerful platform for large-scale spatial analysis using remote sensing data, which can enhance the understanding of flood impacts on various land uses over time.

From the results of specific area comparison of hazard affected LULC; at Gewane the 1D model shows significantly larger areas affected, increasing with higher return periods. GEE also shows a large area affected, but less detailed compared to the 1D and 2D results. At Logia, 1D model shows smaller areas affected for lower return periods, but the area increases with higher return periods. GEE shows a larger extent, possibly capturing a more extensive flood impact. At Dubti, 1D and 2D models show similar areas affected, increasing slightly with higher return periods. GEE shows a much larger extent, likely indicating a more comprehensive impact assessment. Around Assayta, 1D model shows an increase in affected areas with higher return periods, while GEE shows a much larger area affected overall. Around Sa'a, GEE shows an exceptionally large area affected, indicating potential overestimation compared to the precise 2D model results.

According to the comparative results of HEC-RAS 1D, 2D, and GEE; 1D Models is Suitable for riverine flood assessments, providing insights into flood extent along river channels for various return periods. It Offers detailed flood predictions based on historical data but may not capture lateral flood spread as effectively as 2D models. 2D model is Ideal for detailed, local assessments, capturing complex flow patterns and providing precise flood extents. However, High-resolution data provides accurate boundary definitions and detailed flood behavior analysis. According to the study conducted by (Costabile et al., 2015; Dasallas et al., 2019; Ongdas et al., 2020), 2D models that solve complete shallow water equations are said to be highly computationally demanding and data-intensive, but they are also said to be able to accurately predict the date and length of flooding. Their applicability to real-time flood forecasting is limited by these drawbacks. It was said that if a resolution of less than 10 m and/or several model runs are needed, they are not practical for areas larger than 1000 km2.

According to the study by (Pandey et al., 2022) Ganga-Brahmaputra basin faces a growing threat from floods due to climate change. Warmer temperatures and altered monsoon patterns are leading to more frequent and severe flooding events, especially in the lower regions. The 2020 floods caused significant damage across several states in India and Bangladesh, inundating vast areas of farmland and heavily populated zones. This study demonstrates the effectiveness of using satellite data, particularly Sentinel-1A, to map flood extent and identify vulnerable areas. These detailed and timely maps are crucial for disaster management efforts. The high population density in the basin makes it especially risky during floods. The research underscores the need for improved flood risk assessments that consider factors like elevation and building density. Additionally, information on floodwater depth would be invaluable for

targeted disaster response. By utilizing advanced technologies and fostering collaboration between governments and aid agencies, we can better protect communities from the devastating impacts of flooding.

This research (Dasallas et al., 2019) examined a levee breach event in Korea using a flood modeling software called HEC-RAS. Specifically, it tested the 1D-2D modeling capability of HEC-RAS to simulate the real-world flood that happened in Baeksan, Korea in August 2002. The model simulates flooding using a sub-grid bathymetry approach and a hybrid discretization method. The researchers compared the HEC-RAS results to observed flood data and simulations from other flood models (Gerris and FLUMEN). They looked at factors like how far the flood reached, water depth, flow speed, water elevation, and how the flooded area changed over time. Overall, the HEC-RAS results were similar to the other models, with some minor differences. There was a slight variation in the initial flooding extent, likely due to how HEC-RAS models the levee breach in more detail. A bigger difference was seen in how the flooded area increased over time. The HEC-RAS model showed a jump in flooded area that the other models didn't capture. The researchers believe this difference is due to how HEC-RAS handles calculations and how the 1D and 2D elements of the model interact. They argue that HEC-RAS's flooded area is actually more realistic because it better reflects how floods behave in real life.

Another study (Farooq et al., 2019) assessed flood risks along the Swat River in Pakistan using a sophisticated modeling approach. The standard 1D HEC-RAS model wasn't ideal due to limitations in past studies, likely caused by coarse terrain data. Instead, they opted for the 2D HEC-RAS model, specifically designed for simulating flood flows across two dimensions. This method offers a more detailed picture compared to 1D models. The study employed a high-resolution digital elevation model (DEM) with 12-meter spacing to represent the floodplain. To further enhance accuracy, they incorporated data from satellite imagery to refine the DEM. The model's performance was evaluated by comparing its simulations of flood extent and depth with data from a major flood event in 2010. The model successfully replicated the flood, with a simulated maximum depth of 7 meters, aligning well with the observed depth of 6.25 meters (though official records were unavailable due to flood damage). Similarly, the simulated flood extent matched 80% of the area observed in satellite images. Finally, flood hazard maps were generated using the simulated flood depth and extent. The study acknowledges some limitations. Flood gauges were damaged during the 2010 flood, making it difficult to obtain observed flood depth data. Additionally, the lack of post-flood river cross-section information

could have further improved the model's accuracy. Despite these limitations, the study demonstrates the effectiveness of combining 2D HEC-RAS modeling with high-resolution DEMs and satellite data for flood hazard assessment.

While many studies have shown the effectiveness of 2D hydrodynamic models for flood hazard and risk assessment, data scarcity remains a major challenge, especially in regions like Ethiopia. Limited access to high-quality ground-based streamflow data, even with high-resolution satellite imagery, hinders researchers' ability to make reliable flood predictions. This study proposes a unique approach to address this challenge by combining the rich spatial data capabilities of Google Earth Engine with a hydrodynamic model.

Generally, by leveraging Google Earth Engine's extensive geospatial datasets and cloud computing power, researchers can overcome limitations in traditional data collection methods. This approach can unlock the potential for more accurate and efficient flood hazard and risk assessments in data-scarce regions. This innovative combination has the potential to significantly improve flood risk warning and management practices in Ethiopia and other countries facing similar data constraints.

5 CONCLUSION AND RECOMMENDATION

5.1 Conclusion

The study presented a comprehensive analysis of flood inundation mapping and hazard assessment in the Lower Awash River Basin, Ethiopia, utilizing an integrated hydrodynamic model and Google Earth Engine (GEE). The study made use of several datasets, including a high-resolution digital elevation model (DEM) obtained from the Alaska Satellite Facility, hydrological data from the Ethiopian Ministry of Water and Energy (MoWE), and land use and land cover classification data from Copernicus RS products and Landsat images.

To conduct flood modeling and analyze the data, the study utilized various software tools such as HEC-RAS, QGIS, ArcGIS, Python (Jupyter Notebook), HEC-SSP, and Rainbow. These tools facilitated tasks such as flood inundation modeling, hazard map generation, data analysis, and statistical analyses of hydrologic data. Data quality analysis was an integral part of the study, involving the filling of missed data and conducting data homogeneity analysis using statistical techniques like the Pettitt's test, the standard normal homogeneity test, and the Buishand range test.

Additionally, employed outlier detection methods, including the Grubbs and Beck test, to identify and assess data points that significantly deviated from the overall data trend. The document also discussed flood quantile estimation methods, which are crucial for mapping flood inundation, assessing flood hazard, and visualizing flood hazards. The best-fitting distribution for each gauge station was found by analyzing probability distribution functions such as Gumbel, Pearson Type III, Three-Parameter Log-Normal, Two-Parameter Log-Normal, and Log Pearson Type III. The Kolmogorov-Smirnov test statistic and the l-moment ratio diagram (LMRD) are two examples of goodness-of-fit tests that were used to assess how well the chosen theoretical distributions match the observed data.

Through the examination of stream flow data and the application of regional flood frequency analysis, accurate flood quantiles were estimated for various return periods. Calibration and validation of the HEC-RAS simulation demonstrated good agreement with historical flood extents, validating the accuracy of the developed inundation maps. The findings underscored the increasing risk and vulnerability of different areas to flooding events, with agriculture and rangeland consistently identified as highly affected land uses. Gewane and Dubti were identified as the most flood-prone locations, emphasizing the importance of effective flood

management strategies in these areas. The results also highlighted the utility of GEE for flood mapping, particularly in data-scarce regions. Overall, this research provides valuable insights to support decision-making and disaster preparedness efforts in mitigating the adverse impacts of flooding in Ethiopia's Lower Awash River Basin.

5.2 Recommendation

- DEM resolution is crucial, particularly for mapping floods and accurately quantifying the impact of flooding on various land cover classifications. In this study, the 12.5m resolution DEM is used. However, a resolution of less than 1 meter is preferred for constructing the high-resolution DEM for realistic danger maps.
- The Awash River is a perennial waterway, and numerous hydraulic structures and bridges were built to supply water from its source to its mouths during the dry season. Unfortunately, these structures are not measured for hydrodynamic flow study because of a lack of funding and personnel for field surveys. The geometry data of these structures can be measured and imported using HEC-RAS hydraulic simulations.
- It is recommended to address the inaccuracies in daily flow discharge values recorded by many gauge stations in the LARB. These inaccuracies, stemming from missed values (especially at tributary stations), flow regulation, and limited record duration, hinder the effectiveness of Flood Frequency Analysis and further hydrological tasks analysis. To rectify this issue, it is advised to enhance quantile estimation for ungauged sites by incorporating additional catchment characteristics such as slope, elevation, infiltration capacity, stream length, drainage density, and land cover alongside catchment area. This adjustment will improve the accuracy and reliability of the analysis results.
- Based on the analysis conducted, it is evident that utilizing both 1D and 2D HEC-RAS models separately for flood inundation and hazard assessment has been beneficial. However, it has been observed that employing the 2D model for areas exceeding 1000 km^2 with a DEM resolution of less than 10m is not as feasible as the 1D model. Therefore, it is recommended to integrate both 1D/2D models for a combined approach. This combined approach will capitalize on the strengths of each model type while compensating for their respective limitations, ultimately enhancing the accuracy and reliability of flood inundation and hazard assessments across a wider range of scenarios and geographical conditions.

- It is recommended that scholars and decision-makers investigate Google Earth Engine's (GEE) flood mapping capabilities. Using GEE will make it easier to map flood hazards and extents accurately and quickly. This will help achieve the Sustainable Development Goals (SDGs) related to land management, water, and climate change.
- In areas where data scarcity poses a challenge to flood mapping efforts, it is strongly recommended to harness the capabilities of Google Earth Engine (GEE). GEE offers a wealth of remote sensing data and advanced processing tools that can be leveraged to overcome data limitations and generate comprehensive flood maps. Using GEE, researchers and policymakers can access timely and accurate information for effective flood risk assessment and disaster preparedness planning in data-scarce regions.
- Based on the findings and analysis presented in this research study, it is strongly recommended that stakeholders take immediate action to construct river training works to protect society and properties from potential damage. Implementing erosion control measures, such as Levees, embankments, and retaining walls, is essential to stabilize riverbanks and prevent erosion. Enhancing flood management strategies by developing levees, floodwalls, and diversion channels will effectively control and direct water flow, preventing overflow into inhabited areas.

REFERENCES

Achamyeleh, K. (2003). Ethiopia: Integrated flood management. *Integrated Flood Management Case Study*, 1–15.

Afzal, M. A., Ali, S., Nazeer, A., Khan, M. I., Waqas, M. M., Aslam, R. A., Cheema, M. J. M., Nadeem, M., Saddique, N., Muzammil, M., & Shah, A. N. (2022). Flood Inundation Modeling by Integrating HEC–RAS and Satellite Imagery: A Case Study of the Indus River Basin. *Water*, *14*(19), 2984. https://doi.org/10.3390/w14192984

Ahmad, I., Wang, X., Waseem, M., Zaman, M., Aziz, F., Khan, R. Z. N., & Ashraf, M. (2022). Flood Management, Characterization and Vulnerability Analysis Using an Integrated RS-GIS and 2D Hydrodynamic Modelling Approach: The Case of Deg Nullah, Pakistan. *Remote Sensing*, *14*(9), Article 9. https://doi.org/10.3390/rs14092138

Albu, L.-M., Enea, A., Iosub, M., & Breabăn, I.-G. (2020). Dam Breach Size Comparison for Flood Simulations. A HEC-RAS Based, GIS Approach for Drăcșani Lake, Sitna River, Romania. *Water*, *12*(4), 1090. https://doi.org/10.3390/w12041090

Asare-Kyei, D., Forkuor, G., & Venus, V. (2015). Modeling Flood Hazard Zones at the Sub-District Level with the Rational Model Integrated with GIS and Remote Sensing Approaches. *Water*, *7*(12), Article 12. https://doi.org/10.3390/w7073531

Baky, M. A. A., Islam, M., & Paul, S. (2019). Flood Hazard, Vulnerability and Risk Assessment for Different Land Use Classes Using a Flow Model. *Earth Systems and Environment*, *4*(1), 225–244. https://doi.org/10.1007/s41748-019-00141-w

Benameur, S., Benkhaled, A., Meraghni, D., Chebana, F., & Necir, A. (2017). Complete flood frequency analysis in Abiod watershed, Biskra (Algeria). *Natural Hazards*, *86*(2), 519–534. https://doi.org/10.1007/s11069-016-2703-4

Bhandari, M., Nyaupane, N., Mote, S. R., Kalra, A., & Ahmad, S. (2017). 2D Unsteady Flow Routing and Flood Inundation Mapping for Lower Region of Brazos River Watershed.

World Environmental and Water Resources Congress 2017, 292–303. https://doi.org/10.1061/9780784480625.027

Brunner, G. W. (2016). HEC-RAS River Analysis System: Hydraulic Reference Manual, Version 5.0. *US Army Corps of Engineers–Hydrologic Engineering Center*, *547*.

Chen, Y.-W., Tsai, J.-P., Chang, L.-C., Ho, C.-C., & Chen, Y.-C. (2014). The development of a real-time flooding operation model in the Tseng-Wen Reservoir. *Hydrology Research*, *45*(3), Article 3. https://doi.org/10.2166/nh.2013.301

Cirella, G., & Iyalomhe, F. (2018). Flooding Conceptual Review: Sustainability-Focalized Best Practices in Nigeria. *Applied Sciences*, *8*(9), Article 9. https://doi.org/10.3390/app8091558

Costabile, P., Macchione, F., Natale, L., & Petaccia, G. (2015). Flood mapping using LIDAR DEM. Limitations of the 1-D modeling highlighted by the 2-D approach. *Natural Hazards*, *77*(1), 181–204. https://doi.org/10.1007/s11069-015-1606-0

Daba, M. H., Ayele, G. T., & You, S. (2020). Long-Term Homogeneity and Trends of Hydroclimatic Variables in Upper Awash River Basin, Ethiopia. *Advances in Meteorology*, *2020*, 1–21. https://doi.org/10.1155/2020/8861959

Dasallas, L., Kim, Y., & An, H. (2019). Case Study of HEC-RAS 1D–2D Coupling Simulation: 2002 Baeksan Flood Event in Korea. *Water*, *11*(10), 2048. https://doi.org/10.3390/w11102048

Deoli, V., Kumar, D., & Kuriqi, A. (2022). Detection of Water Spread Area Changes in Eutrophic Lake Using Landsat Data. *Sensors*, *22*(18), 6827. https://doi.org/10.3390/s22186827

Desalegn, H., & Mulu, A. (2021). Mapping flood inundation areas using GIS and HEC-RAS model at Fetam River, Upper Abbay Basin, Ethiopia. *Scientific African*, *12*, e00834. https://doi.org/10.1016/j.sciaf.2021.e00834

Dewan, T. H. (2015). Societal impacts and vulnerability to floods in Bangladesh and Nepal. *Weather and Climate Extremes*, *7*, 36–42. https://doi.org/10.1016/j.wace.2014.11.001

Drissia, T. K., Jothiprakash, V., & Anitha, A. B. (2019). Flood Frequency Analysis Using L Moments: A Comparison between At-Site and Regional Approach. *Water Resources Management*, *33*(3), 1013–1037. https://doi.org/10.1007/s11269-018-2162-7

Duguma, F. A., Feyessa, F. F., Demissie, T. A., & Januszkiewicz, K. (2021). Hydroclimate Trend Analysis of Upper Awash Basin, Ethiopia. *Water*, *13*(12), Article 12. https://doi.org/10.3390/w13121680

Edamo, M. L., Hatiye, S. D., Minda, T. T., & Ukumo, T. Y. (2023). Flood inundation and risk mapping under climate change scenarios in the lower Bilate catchment, Ethiopia. *Natural Hazards*, *118*(3), 2199–2226. https://doi.org/10.1007/s11069-023-06101-y

Erena, S. H., Worku, H., & De Paola, F. (2018). Flood hazard mapping using FLO-2D and local management strategies of Dire Dawa city, Ethiopia. *Journal of Hydrology: Regional Studies*, *19*, 224–239. https://doi.org/10.1016/j.ejrh.2018.09.005

Fana FBC. (2021, August 8). Three localties in Afar region hit by heavy flooding as Awash River overflows its banks. *Welcome to Fana Broadcasting Corporate S.C.* https://www.fanabc.com/english/three-localties-in-afar-region-hit-by-heavy-flooding-as-awash-river-overflows-its-banks/

Fana FBC, F. (2020, August 5). Floods displace 32,000 in Afar regional state. *Welcome to Fana Broadcasting Corporate S.C.* https://www.fanabc.com/english/floods-displace-32000-in-afar-regional-state/

Farooq, M., Shafique, M., & Khattak, M. S. (2019). Flood hazard assessment and mapping of River Swat using HEC-RAS 2D model and high-resolution 12-m TanDEM-X DEM (WorldDEM). *Natural Hazards*, *97*(2), Article 2. https://doi.org/10.1007/s11069-019-03638-9

Fenglin, W., Ahmad, I., Zelenakova, M., Fenta, A., Dar, M. A., Teka, A. H., Belew, A. Z., Damtie, M., Berhan, M., & Shafi, S. N. (2023). Exploratory regression modeling for flood susceptibility mapping in the GIS environment. *Scientific Reports*, *13*(1), Article 1. https://doi.org/10.1038/s41598-023-27447-0

FloodList. (2020, September 11). *Ethiopia – 300,000 Displaced by Floods, Says UN – FloodList*. https://floodlist.com/africa/ethiopia-floods-update-september-2020

FloodList. (2021, May 14). *Ethiopia – Thousands Displaced by Floods in Afar, SNNP and Somali Regions – FloodList*. https://floodlist.com/africa/ethiopia-floods-afar-snnp-somali-may-2021

Gao, Y., Merz, C., Lischeid, G., & Schneider, M. (2018). A review on missing hydrological data processing. *Environmental Earth Sciences*, *77*(2), 47. https://doi.org/10.1007/s12665-018-7228-6

Getahun YS, G. S. (2015) G. (2015). Flood Hazard Assessment and Mapping of Flood Inundation Area of the Awash River Basin in Ethiopia using GIS and HEC-GeoRAS/HEC-RAS Model. *Journal of Civil & Environmental Engineering*, *05*(04). https://doi.org/10.4172/2165-784X.1000179

Getaneh, A. G. (2023). *Flood Risk Mapping and Assessment in Middle Awash Sub-Basin, Ethiopia ASTU M.Sc. Thesis*.

Ghimire, E., Sharma, S., & Lamichhane, N. (2022). Evaluation of one-dimensional and two-dimensional HEC-RAS models to predict flood travel time and inundation area for flood warning system. *ISH Journal of Hydraulic Engineering*, *28*(1), 110–126. https://doi.org/10.1080/09715010.2020.1824621

Ghosh, S., Kumar, D., & Kumari, R. (2022). Cloud-based large-scale data retrieval, mapping, and analysis for land monitoring applications with Google Earth Engine (GEE). *Environmental Challenges*, *9*, 100605. https://doi.org/10.1016/j.envc.2022.100605

Haddad, K. (2021). Selection of the best fit probability distributions for temperature data and the use of L-moment ratio diagram method: A case study for NSW in Australia. *Theoretical and Applied Climatology*, *143*(3–4), 1261–1284. https://doi.org/10.1007/s00704-020-03455-2

Hagen, E., & Lu, X. X. (2011). Let us create flood hazard maps for developing countries. *Natural Hazards*, *58*(3), 841–843. https://doi.org/10.1007/s11069-011-9750-7

Hagos, Y. G., Andualem, T. G., Yibeltal, M., & Mengie, M. A. (2022). Flood hazard assessment and mapping using GIS integrated with multi-criteria decision analysis in upper Awash River basin, Ethiopia. *Applied Water Science*, *12*(7), 148. https://doi.org/10.1007/s13201-022-01674-8

Hosking, J. R. (1990). L-moments: Analysis and estimation of distributions using linear combinations of order statistics. *Journal of the Royal Statistical Society Series B: Statistical Methodology*, *52*(1), 105–124.

Koriche, S. A., & Rientjes, T. H. M. (2016). Application of satellite products and hydrological modelling for flood early warning. *Physics and Chemistry of the Earth, Parts A/B/C*, *93*, 12–23. https://doi.org/10.1016/j.pce.2016.03.007

Namara, W. G., Damisse, T. A., & Tufa, F. G. (2022). Application of HEC-RAS and HEC-GeoRAS model for Flood Inundation Mapping, the case of Awash Bello Flood Plain, Upper Awash River Basin, Oromiya Regional State, Ethiopia. *Modeling Earth Systems and Environment*, *8*(2), Article 2. https://doi.org/10.1007/s40808-021-01166-9

NDRMC. (2018). *Federal Democratic Republic of Ethiopia National Disaster Risk Management Commission, Early Warning and Emergency Response Directorate*.

Ongdas, N., Akiyanova, F., Karakulov, Y., Muratbayeva, A., & Zinabdin, N. (2020). Application of HEC-RAS (2D) for Flood Hazard Maps Generation for Yesil (Ishim) River in Kazakhstan. *Water*, *12*(10), 2672. https://doi.org/10.3390/w12102672

Pandey, A. C., Kaushik, K., & Parida, B. R. (2022). Google Earth Engine for Large-Scale Flood Mapping Using SAR Data and Impact Assessment on Agriculture and Population of Ganga-Brahmaputra Basin. *Sustainability*, *14*(7), 4210. https://doi.org/10.3390/su14074210

Papaioannou, G., Loukas, A., Vasiliades, L., & Aronica, G. T. (2016). Flood inundation mapping sensitivity to riverine spatial resolution and modelling approach. *Natural Hazards*, *83*(S1), 117–132. https://doi.org/10.1007/s11069-016-2382-1

Patakamuri, S. K., Muthiah, K., & Sridhar, V. (2020). Long-Term Homogeneity, Trend, and Change-Point Analysis of Rainfall in the Arid District of Ananthapuramu, Andhra Pradesh State, India. *Water*, *12*(1), 211. https://doi.org/10.3390/w12010211

Psomiadis, E., Diakakis, M., & Soulis, K. X. (2020). Combining SAR and Optical Earth Observation with Hydraulic Simulation for Flood Mapping and Impact Assessment. *Remote Sensing*, *12*(23), 3980. https://doi.org/10.3390/rs12233980

Raes, D., Willems, P., & Gbaguidi, F. (2016). *RAINBOW - a software package for hydrometeorological frequency analysis and testing the homogeneity of historical data sets*.

Rangari, V. A., Sridhar, V., Umamahesh, N. V., & Patel, A. K. (2019). Floodplain Mapping and Management of Urban Catchment Using HEC-RAS: A Case Study of Hyderabad City. *Journal of The Institution of Engineers (India): Series A*, *100*(1), 49–63. https://doi.org/10.1007/s40030-018-0345-0

Santillan, J. R., Marqueso, J. T., Makinano-Santillan, M., & Serviano, J. L. (2016). Beyond Flood Hazard Maps: Detailed Flood Characterization With Remote Sensing, Gis And 2D Modelling. *The International Archives of the Photogrammetry, Remote Sensing and Spatial Information Sciences*, *XLII-4/W1*, 315–323. https://doi.org/10.5194/isprs-archives-XLII-4-W1-315-2016

Shadmehri Toosi, A., Doulabian, S., Ghasemi Tousi, E., Calbimonte, G. H., & Alaghmand, S. (2020). Large-scale flood hazard assessment under climate change: A case study. *Ecological Engineering*, *147*, 105765. https://doi.org/10.1016/j.ecoleng.2020.105765

Su, X., Shao, W., Liu, J., Jiang, Y., & Wang, K. (2021). Dynamic Assessment of the Impact of Flood Disaster on Economy and Population under Extreme Rainstorm Events. *Remote Sensing*, *13*(19), 3924. https://doi.org/10.3390/rs13193924

Subramanya, K. (2008). *Engineering hydrology*. McGraw-Hill.

Tamiru, H., & Dinka, M. O. (2021). Application of ANN and HEC-RAS model for flood inundation mapping in lower Baro Akobo River Basin, Ethiopia. *Journal of Hydrology: Regional Studies*, *36*, 100855. https://doi.org/10.1016/j.ejrh.2021.100855

Tansar, H., Babur, M., & Karnchanapaiboon, S. L. (2020). Flood inundation modeling and hazard assessment in Lower Ping River Basin using MIKE FLOOD. *Arabian Journal of Geosciences*, *13*(18), 934. https://doi.org/10.1007/s12517-020-05891-w

Thiemig, V., De Roo, A., & Gadain, H. (2011). Current status on flood forecasting and early warning in Africa. *International Journal of River Basin Management*, *9*(1), Article 1. https://doi.org/10.1080/15715124.2011.555082

Timbadiya, P. V., Patel, P. L., & Porey, P. D. (2011). Calibration of HEC-RAS Model on Prediction of Flood for Lower Tapi River, India. *Journal of Water Resource and Protection*, *03*(11), Article 11. https://doi.org/10.4236/jwarp.2011.311090

Trambadia, N. K., Patel, D. P., Patel, V. M., & Gundalia, M. J. (2023). *Flood inundation assessment in the data-scarce region using hydrodynamic models and google earth engine -A case of Ghed region, Ozat River basin, Gujarat, India* [Preprint]. In Review. https://doi.org/10.21203/rs.3.rs-2321703/v1

Ukumo, T. Y., Abebe, A., Lohani, T. K., & Edamo, M. L. (2022). Flood hazard mapping and analysis under climate change using hydro-dynamic model and RCPs emission scenario

in Woybo River catchment of Ethiopia. *World Journal of Engineering*, *20*(3), 559–576. https://doi.org/10.1108/WJE-07-2021-0410

Ul Hassan, M., Hayat, O., & Noreen, Z. (2019). Selecting the best probability distribution for at-site flood frequency analysis; a study of Torne River. *SN Applied Sciences*, *1*(12), 1629. https://doi.org/10.1007/s42452-019-1584-z

Vojtek, M., & Vojteková, J. (2016). Flood hazard and flood risk assessment at the local spatial scale: A case study. *Geomatics, Natural Hazards and Risk*, *7*(6), 1973–1992. https://doi.org/10.1080/19475705.2016.1166874

Wagner, W., Bauer-Marschallinger, B., Navacchi, C., Reuß, F., Cao, S., Reimer, C., Schramm, M., & Briese, C. (2021). A Sentinel-1 Backscatter Datacube for Global Land Monitoring Applications. *Remote Sensing*, *13*(22), 4622. https://doi.org/10.3390/rs13224622

Wondim, Y. K. (2016). *Flood Hazard and Risk Assessment Using GIS and Remote Sensing in Lower Awash Sub-basin, Ethiopia*.

Xu, H. (2006). Modification of normalised difference water index (NDWI) to enhance open water features in remotely sensed imagery. *International Journal of Remote Sensing*, *27*(14), Article 14. https://doi.org/10.1080/01431160600589179

Zalnezhad, A., Rahman, A., Ahamed, F., Vafakhah, M., & Samali, B. (2023). Design flood estimation at ungauged catchments using index flood method and quantile regression technique: A case study for South East Australia. *Natural Hazards*, *119*(3), 1839–1862. https://doi.org/10.1007/s11069-023-06184-7

APPENDICES

Appendix A : Homogeneity test for stream flow stations using Rainbow software

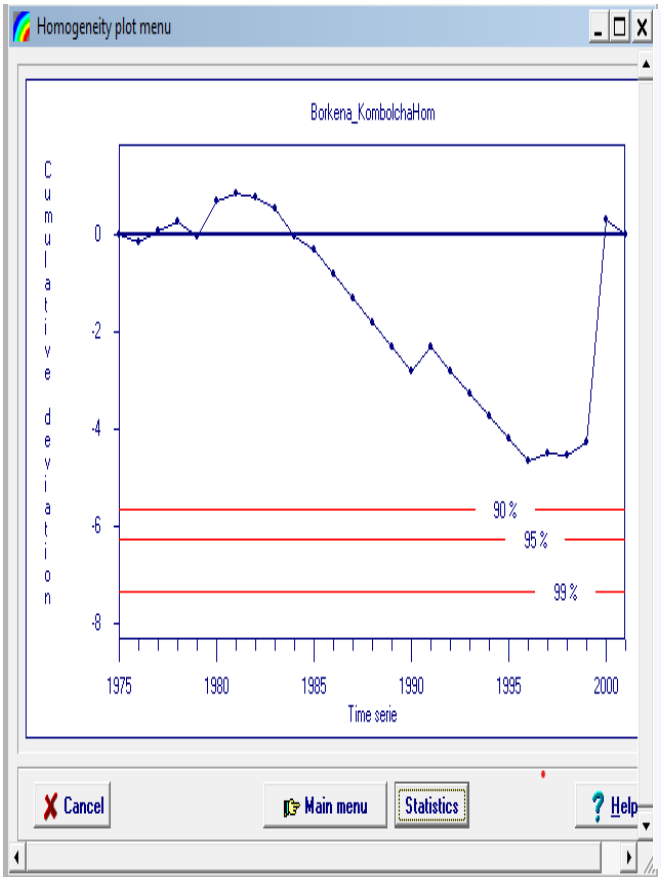

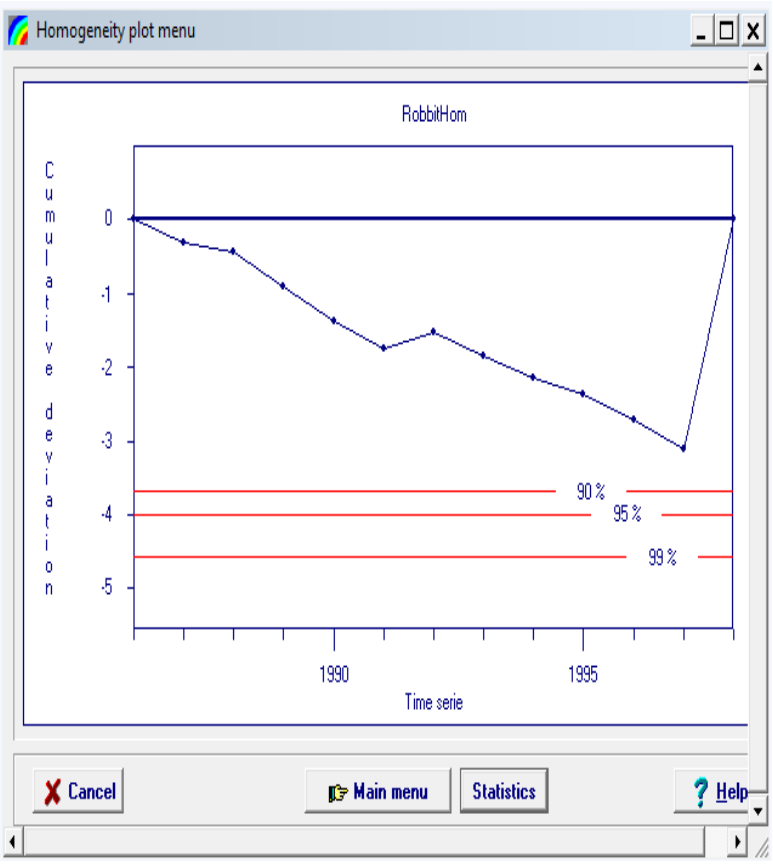

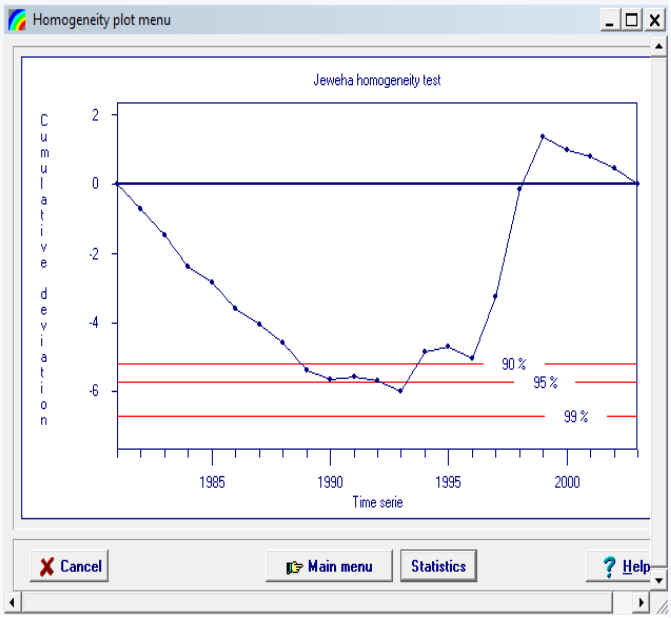

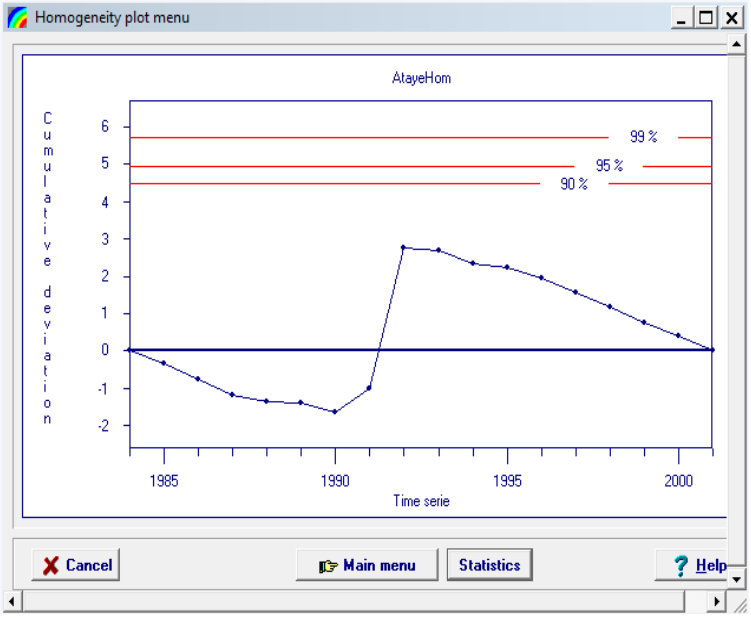

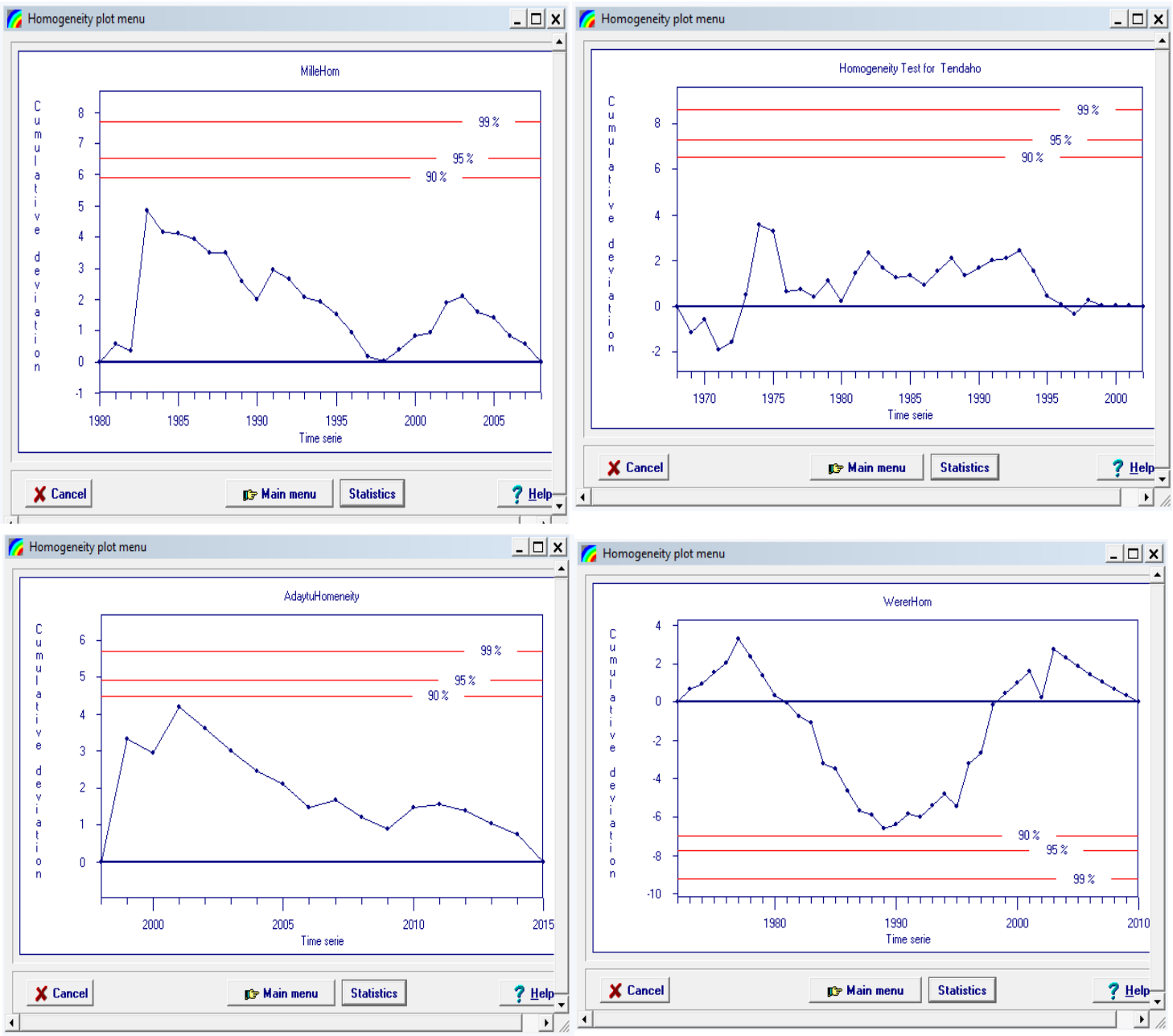

Appendix B: Quantile Water level for Mille and Logia River

Quantile Water level for Mille River station 22400 for n = 0.043					
Observed			**Simulated**		
Return period	**WL Observed**	**QT**	**Min Cha El (m)**	**W.S Elev (m)**	**WL (Simulated)**
5	2.23	300.74	442	445.26	3.26
10	**3.25**	391.05	442	445.54	3.54
20	3.446	497.43	442	445.78	3.78

50	3.6	671.08	442	446.11	4.11
100	3.92	834.31	442	446.37	4.37
200	4.03	1031.93	442	446.65	4.65
500	4.3	1358.99	442	447.04	5.04

Quantile Water level for Mille River station 22400 for n = 0.04

Observed			**Simulated**		
Return period	**WL Observed**	**QT**	**Min Cha El (m)**	**W.S Elev (m)**	**WL (Simulated)**
5	2.23	300.74	442	445.2	3.2
10	**3.25**	391.05	442	445.48	3.48
20	3.446	497.43	442	445.72	3.72
50	3.6	671.08	442	446.04	4.04
100	3.92	834.31	442	446.3	4.3
200	4.03	1031.93	442	446.59	4.59
500	4.3	1358.99	442	446.96	4.96

Quantile Water level for Mille River station 22400 for n = 0.035

Observed			**Simulated**		
Return period	**WL Observed**	**QT**	**Min Cha El (m)**	**W.S Elev (m)**	**WL (Simulated)**
5	2.23	300.74	442	445.11	3.11
10	**3.25**	391.05	442	445.36	3.36
20	3.446	497.43	442	445.62	3.62
50	3.6	671.08	442	445.94	3.94
100	3.92	834.31	442	446.19	4.19
200	4.03	1031.93	442	446.46	4.46
500	4.3	1358.99	442	446.83	4.83

Quantile Water level for Mille River station 22400 for n = 0.03

Observed			**Simulated**		
Return period	**WL Observed**	**QT**	**Min Cha El (m)**	**W.S Elev (m)**	**WL (Simulated)**
5	2.23	296.53	442	444.92	2.92
10	**3.25**	382.17	442	445.24	3.24

20	3.446	486.78	442	445.5	3.5
50	3.6	667.48	442	445.81	3.81
100	3.92	848.04	442	446.06	4.06
200	4.03	1079.15	442	446.33	4.33
500	4.3	1488	442	446.7	4.7

Quantile Water level for Logia River station 21600 for n = 0.043					
Observed			**Simulated**		
Return period	**WL Observed**	**QT**	**Min Cha El (m)**	**W.S Elev (m)**	**WL (Simulated)**
5	3.493	284.39	402	405.21	3.21
10	**3.503**	391.44	402	405.52	3.52
20	3.51	496.76	402	405.79	3.79
50	3.86	634.34	402	406.11	4.11
100	3.97	737.56	402	406.31	4.31
200	4.23	840.27	402	406.48	4.48
500	4.6	975.41	402	406.7	4.7
Quantile Water level for Logia River station 21600 for n = 0.04					
Observed			**Simulated**		
Return period	**WL Observed**	**QT**	**Min Cha El (m)**	**W.S Elev (m)**	**WL (Simulated)**
5	3.493	284.39	402	405.18	3.18
10	**3.503**	391.44	402	405.49	3.49
20	3.51	496.76	402	405.75	3.75
50	3.86	634.34	402	406.07	4.07
100	3.97	737.56	402	406.27	4.27
200	4.23	840.27	402	406.44	4.44
500	4.6	975.41	402	406.66	4.66
Quantile Water level for Logia River station 21600 for n = 0.035					
Observed			**Simulated**		
Return period	**WL Observed**	**QT**	**Min Cha El (m)**	**W.S Elev (m)**	**WL (Simulated)**

5	3.493	284.39	402	405.12	3.12
10	**3.503**	391.44	402	405.43	3.43
20	3.51	496.76	402	405.68	3.68
50	3.86	634.34	402	406	4
100	3.97	737.56	402	406.2	4.2
200	4.23	840.27	402	406.37	4.37
500	4.6	975.41	402	406.58	4.58
Quantile Water level for Logia River station 21600 for n = 0.03					
Observed			**Simulated**		
Return period	**WL Observed**	**QT**	**Min Cha El (m)**	**W.S Elev (m)**	**WL (Simulated)**
5	3.493	284.39	402	405.05	3.05
10	**3.503**	391.44	402	405.36	3.36
20	3.51	496.76	402	405.6	3.6
50	3.86	634.34	402	405.91	3.91
100	3.97	737.56	402	406.11	4.11
200	4.23	840.27	402	406.28	4.28
500	4.6	975.41	402	406.48	4.48

Appendix C1: Observed Vs simulated WL for Mille river station 22400

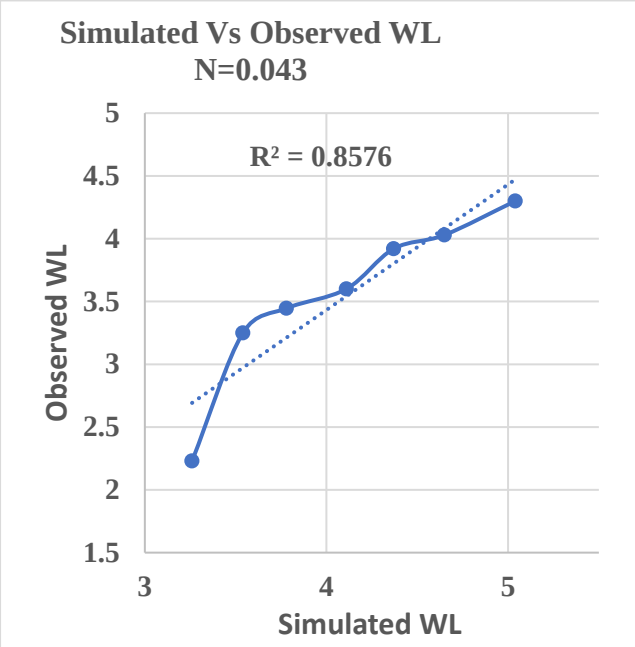

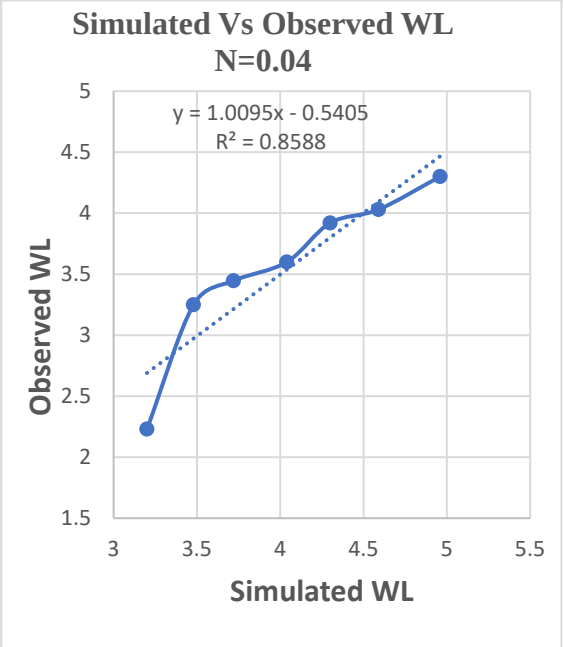

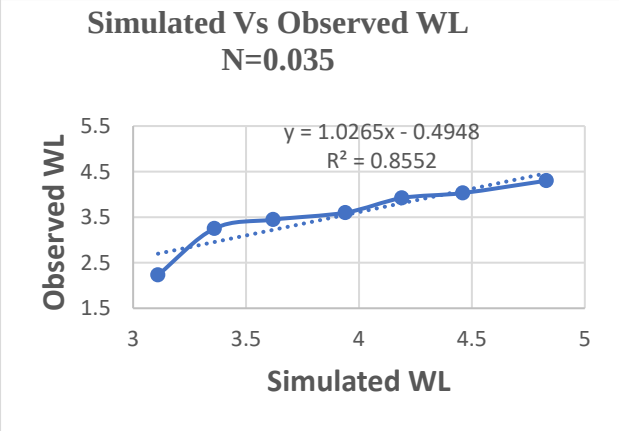

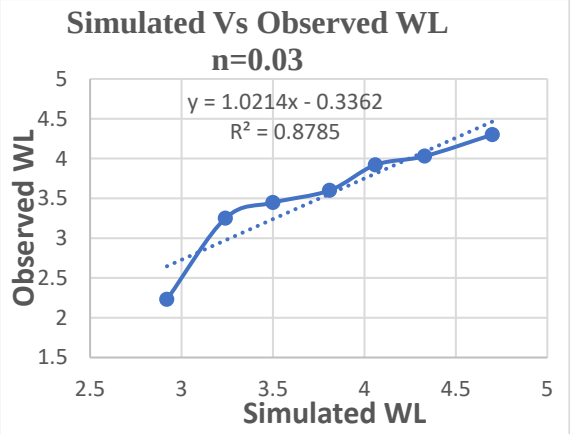

Appendix C2: Observed Vs simulated WL for Logia River station 21600

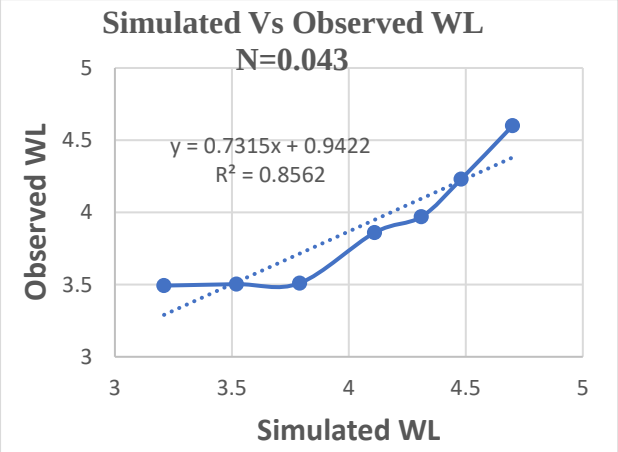

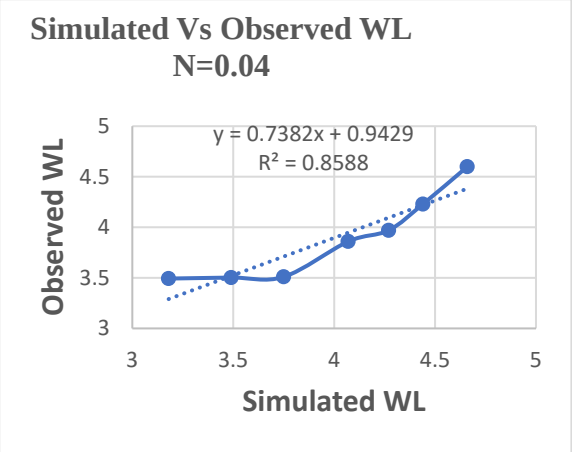

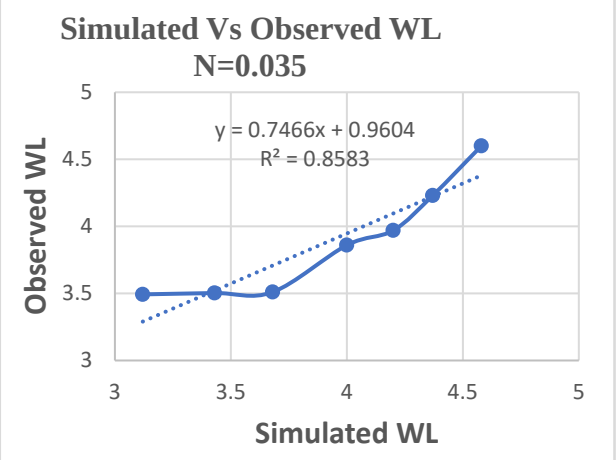

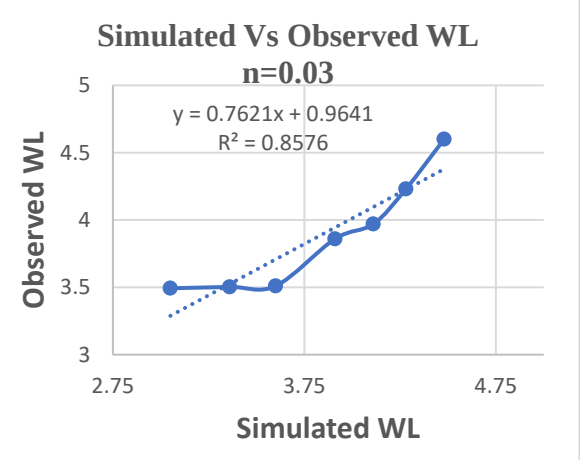

Appendix D: Flood affected areas and Hazard Levels from inundation depth

Affected Area	Return Periods							
	5 Year				10 Year			
	Low	**Medium**	**High**	**Extreme**	**Low**	**Medium**	**High**	**Extreme**
Gewane	3038.71	2292.64	2196.69	75.84	3271.98	2697.17	2667.45	90.11
Logia	364.39	219.48	274.89	10.93	377.92	320.00	375.56	15.73
Dubti	767.30	479.83	513.23	33.37	897.99	647.64	628.78	40.84
Alalnaba	317.37	129.60	442.67	5.81	96.53	455.64	451.89	11.61
Assayta	447.80	280.62	289.66	10.96	515.78	374.94	348.54	12.54
Affected Area	20 Year				50 Year			
	Low	**Medium**	**High**	**Extreme**	**Low**	**Medium**	**High**	**Extreme**
Gewane	3256.25	2702.98	2606.08	101.03	3774.52	2689.84	2660.97	109.20
Logia	389.64	362.23	411.05	24.42	500.44	395.67	466.47	32.14
Dubti	928.52	650.31	620.01	50.64	1063.11	640.35	627.73	53.46
Alalnaba	67.26	446.61	451.31	12.19	103.26	426.77	451.31	12.19
Assayta	505.18	361.73	326.14	14.08	557.23	350.63	306.28	14.29
Affected Area	100 Year				200 Year			
	Low	**Medium**	**High**	**Extreme**	**Low**	**Medium**	**High**	**Extreme**
Gewane	3694.34	2988.86	2298.58	94.67	4125.30	2959.66	2266.30	95.61
Logia	520.92	432.19	477.92	30.94	573.81	443.55	513.14	33.05
Dubti	1072.03	685.65	572.31	46.58	1169.79	694.59	582.21	47.33
Alalnaba	266.44	225.86	448.73	9.49	405.41	122.94	418.44	6.92
Assayta	540.92	348.32	267.79	12.30	588.23	322.39	251.49	11.89
Affected Area	500 Year							
	Low	**Medium**	**High**	**Extreme**				
Gewane	4105.22	2942.63	2243.16	96.31				
Logia	584.77	450.89	589.59	37.69				
Dubti	1146.51	708.32	603.49	48.08				
Alalnaba	424.22	270.02	223.33	5.64				
Assayta	570.41	301.67	235.95	11.08				

Appendix E: Flood affected areas and Hazard Levels from flow velocity

Affected Area	Return Periods					
	5 Year			10 Year		
	Low	**Medium**	**High**	**Low**	**Medium**	**High**
Gewane	137.7656	1146.32	1098.346967	137.4844	15.64063	1778.302
Logia	250.3906	26.1875	5.328125	269.0156	74.6875	20.09375
Dubti	210.8594	278.9721	256.6174557	27.14063	431.7625	285.8097
Alalnaba	30.57813	86.39748	277.0155992	18.60938	227.8219	265.8199
Assayta	23.125	140.3123	165.5203308	18.3125	249.9625	216.4868
Affected Area	20 Year			50 Year		
	Low	**Medium**	**High**	**Low**	**Medium**	**High**
Gewane	591.9063	13.76563	1737.385417	572.125	18.04688	1.28125
Logia	460.2031	171.4375	220.9929435	541.6563	219.9375	65.875
Dubti	846.2031	6.765625	336.9599185	860.7969	5.890625	313.8656
Alalnaba	7.1875	297.7375	225.65625	3.890625	213.0648	192.8686
Assayta	138.9375	2.09375	171.6513158	119.5938	1.90625	106.7182
Affected Area	100 Year			200 Year		
	Low	**Medium**	**High**	**Low**	**Medium**	**High**
Gewane	516.0938	15.20313	1.71875	496.0156	21.5625	2.671875
Logia	772.4219	113.7813	21.25	657.5625	135.4375	19.3125
Dubti	858.3281	1.734375	190.76875	870.4219	216.5313	0
Alalnaba	135.2475	0	201.2219731	302.7969	0	0
Assayta	15.20313	1.71875	141.6865079	88.9375	0.046875	1.34375
Affected Area	500 Year					
	Low	**Medium**	**High**			
Gewane	2680.359	28.375	3.625			
Logia	683.5781	275.7969	61.484375			
Dubti	682.7656	0.171875	287.375			
Alalnaba	223.0625	177.6439	106.3482143			
Assayta	537.5625	5.265625	188.76			

Appendix F: Hazard affected areas in terms of land use land cover

Affected Area	Return Periods											
	5 Year						10 Year					
	Area of Hazard Level in Land Use land Cover (ha)						Area of Hazard Level in Land Use land Cover (ha)					
	Water	Trees	Vegetation	Agriculture	Bare Ground	Range land	Water	Trees	Vegetation	Agriculture	Bare Ground	Range land
Gewane	446.1	1163	941.1521	2639.079	236.48	4959	473.2	1255	999.1905	2827.986	249.48	5303
Logia	9.185	27.57		137.9207	93.279	937	11.77	30.6		175.92953	107.9	1065
Dubti	59.32	343.1	0.625936	1082.677	21.091	662.7	65.25	366	0.703575	1184.7603	24.174	736
Alalnaba	25.66	167.6	162.7081	480.7867	2.1302	252.1	25.95	171	164.0967	485.98796	2.1302	256
Assayta	77.43	94.12	3.003229	1053.785	4.4217	108	80.05	97.4	3.08515	1126.9028	4.674	113

Affected Area	Return Periods											
	20 Year						50 Year					
	Area of Hazard Level in Land Use land Cover (ha)						Area of Hazard Level in Land Use land Cover (ha)					
	Water	Trees	Vegetation	Agriculture	Bare Ground	Range land	Water	Trees	Vegetation	Agriculture	Bare Ground	Range land
Gewane	475.3	1333	1038.544	2920.723	258.03	5506	489.1	1446	1083.211	3092.7066	271.79	5816
Logia	14.32	33.39		203.8801	121.03	1160	17.02	38.9		236.45002	141.48	1290
Dubti	69.51	375.5	0.735056	1250.943	26.101	776.7	72.87	382	0.744056	1332.6347	28.974	831
Alalnaba	26.03	171	164.2644	486.7694	2.1378	256.1	26.1	171	164.447	487.34761	2.1443	257
Assayta	81.03	98.5	3.094137	1147.598	4.7591	115.9	81.51	99.3	3.101781	1163.4978	4.8138	118

Affected Area	Return Periods											
	100 Year						200 Year					
	Area of Hazard Level in Land Use land Cover (ha)						Area of Hazard Level in Land Use land Cover (ha)					
	Water	Trees	Vegetation	Agriculture	Bare Ground	Range land	Water	Trees	Vegetation	Agriculture	Bare Ground	Range land
Gewane	490.7	1483	1093.885	3163.159	277.42	6011	493	1533	1108.878	3220.7704	289.04	6193
Logia	18.81	39.86		264.8257	154.91	1386	20.88	41.3		294.77474	169.92	1475
Dubti	75.64	384.5	0.744056	1384.806	30.941	877.5	78.17	386	0.744056	1440.4927	33.199	924
Alalnaba	26.12	171.6	164.5662	487.6294	2.1443	256.8	26.14	172	164.6425	487.74297	2.1443	257
Assayta	81.58	99.8	3.101781	1169.608	4.8199	118.7	81.73	100	3.103331	1173.5925	4.8264	119

Affected Area	Return Periods
	500 Year
	Area of Hazard Level in Land Use land Cover (ha)

	Water	Trees	Vegetation	Agriculture	Bare Ground	Range land
Gewane	495.2	1595	1125.968	3306.987	303.26	6393
Logia	24.36	43.15		325.2207	191.85	1572
Dubti	80.98	387.9	0.744056	1521.549	35.525	962.8
Alalnaba	26.16	171.8	164.6955	487.8274	2.1443	257
Assayta	81.93	100.5	3.104662	1176.707	4.8461	119.7

Appendix G: Hazard maps for return periods from (5 year to 500 year).

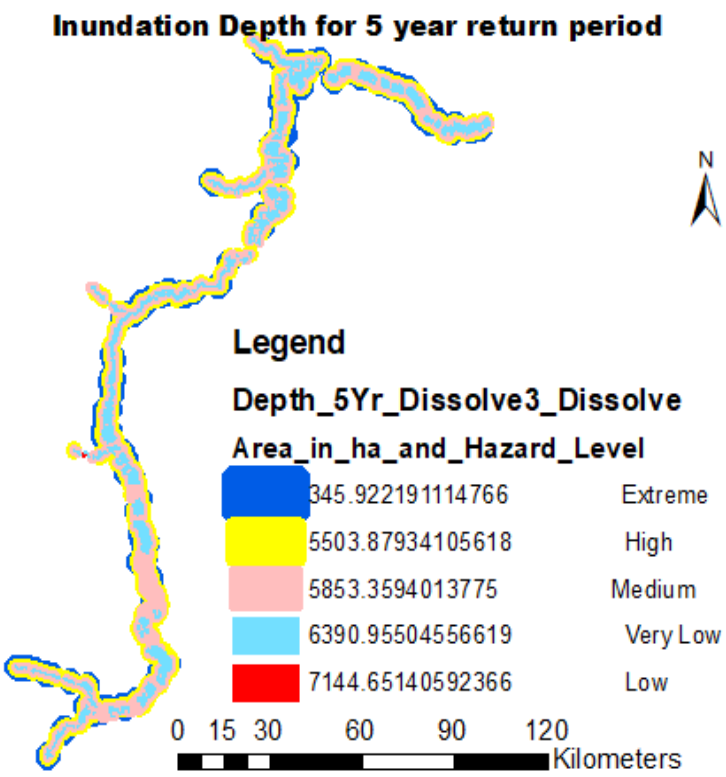

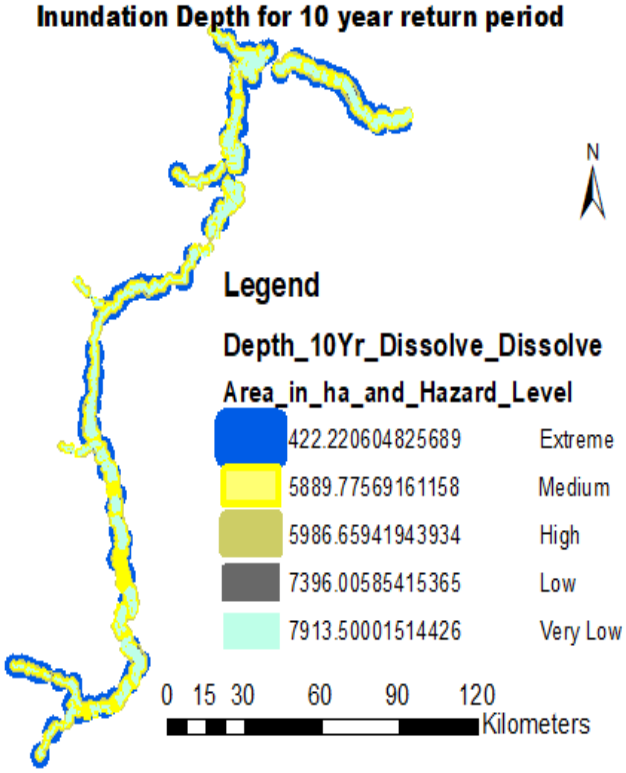

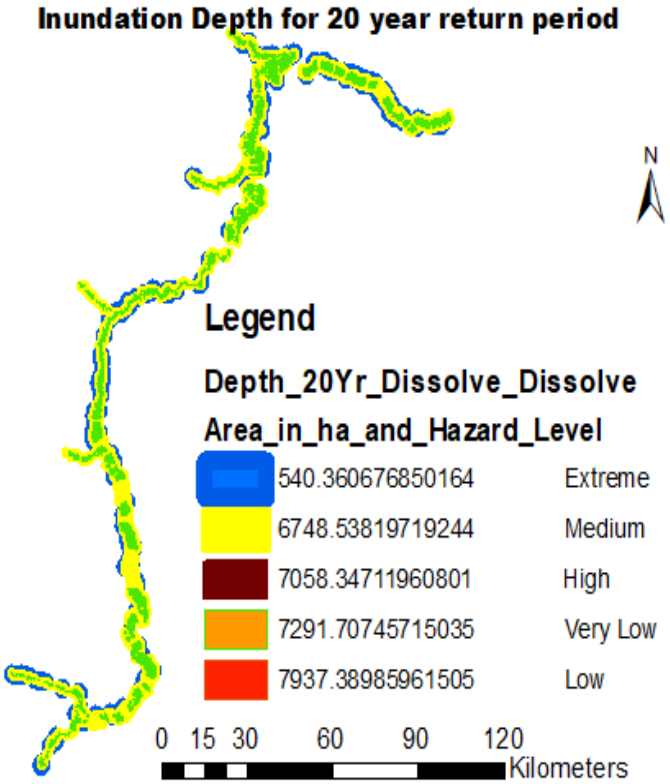

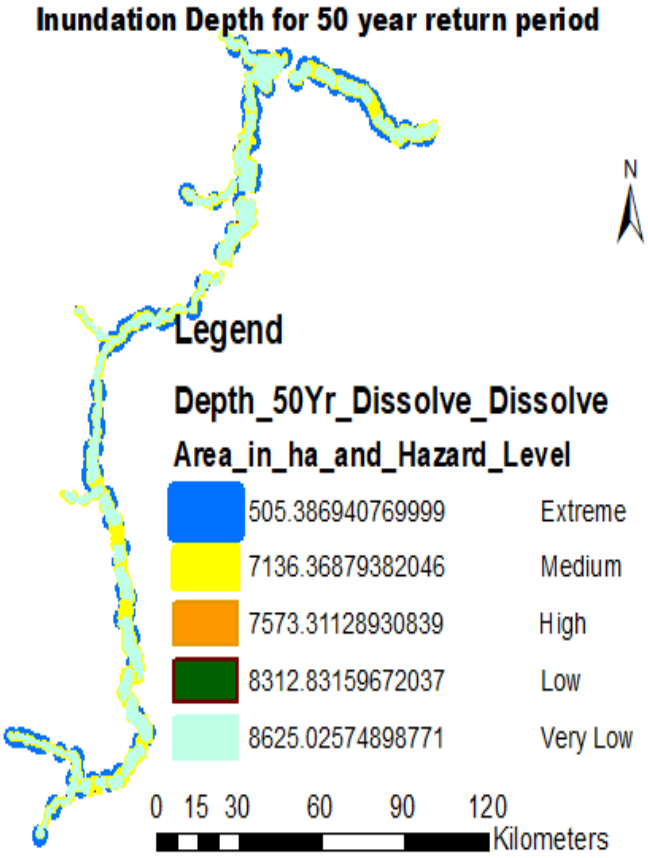

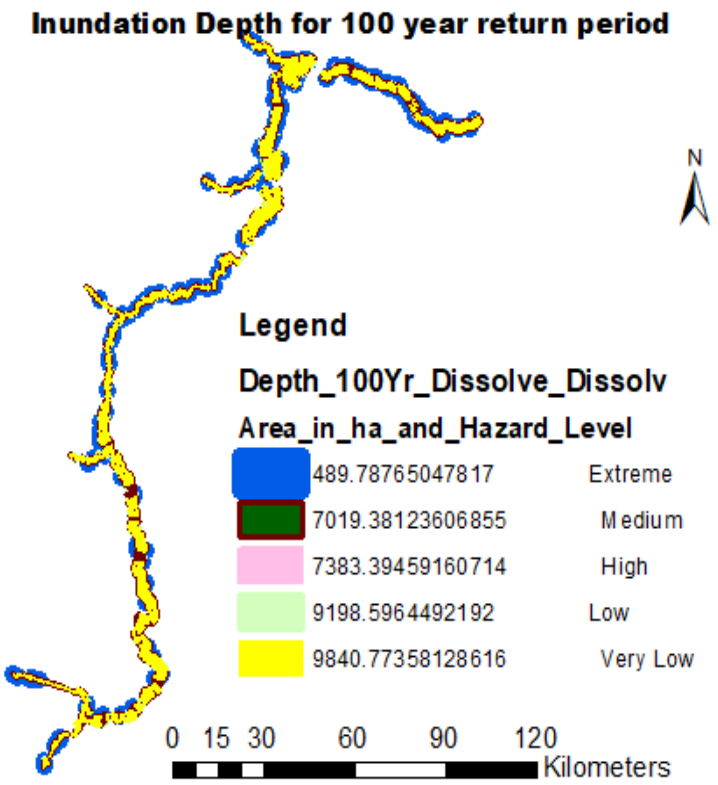
Inundation Depth for 100 year return period
N
Legend
Depth_100Yr_Dissolve_Dissolv
Area_in_ha_and_Hazard_Level
489.78765047817 Extreme
7019.38123606855 Medium
7383.39459160714 High
9198.5964492192 Low
9840.77358128616 Very Low
0 15 30 60 90 120
Kilometers

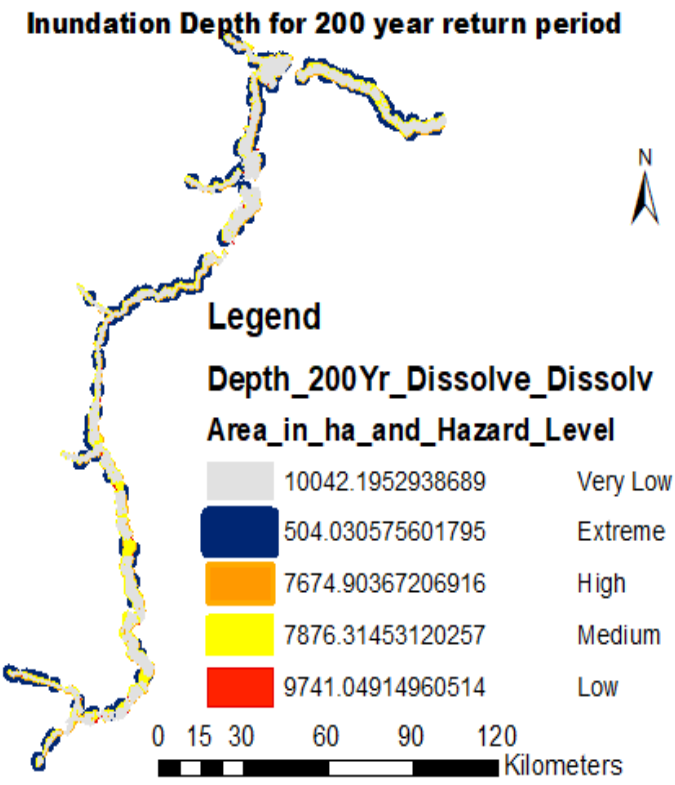
Inundation Depth for 200 year return period
N
Legend
Depth_200Yr_Dissolve_Dissolv
Area_in_ha_and_Hazard_Level
10042.1952938689 Very Low
504.030575601795 Extreme
7674.90367206916 High
7876.31453120257 Medium
9741.04914960514 Low
0 15 30 60 90 120
Kilometers

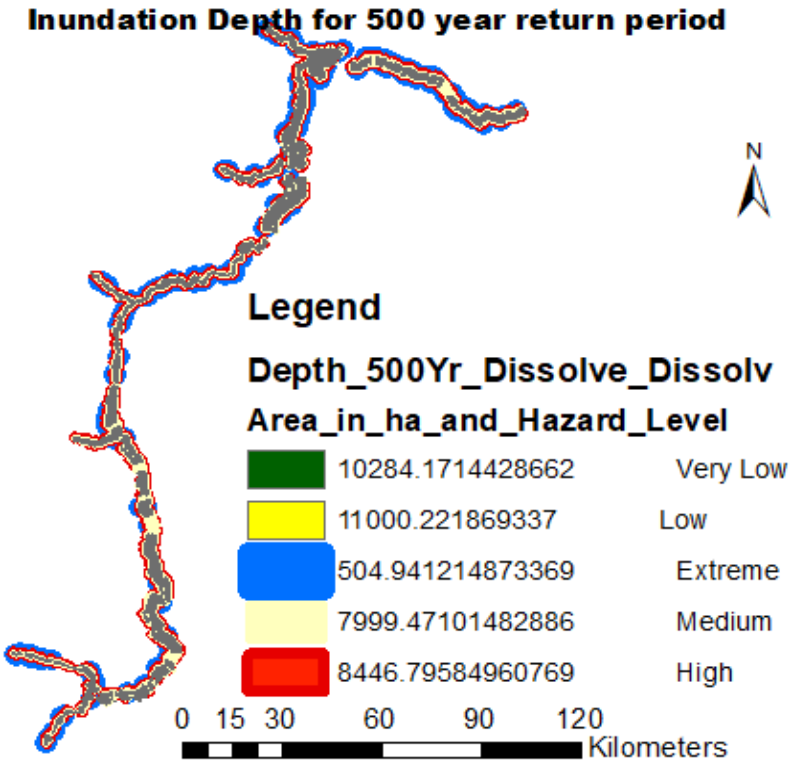
Inundation Depth for 500 year return period
N
Legend
Depth_500Yr_Dissolve_Dissolv
Area_in_ha_and_Hazard_Level
10284.1714428662 Very Low
11000.221869337 Low
504.941214873369 Extreme
7999.47101482886 Medium
8446.79584960769 High
0 15 30 60 90 120
Kilometers

Appendix H: Hazard map for HEC-RAS 2D

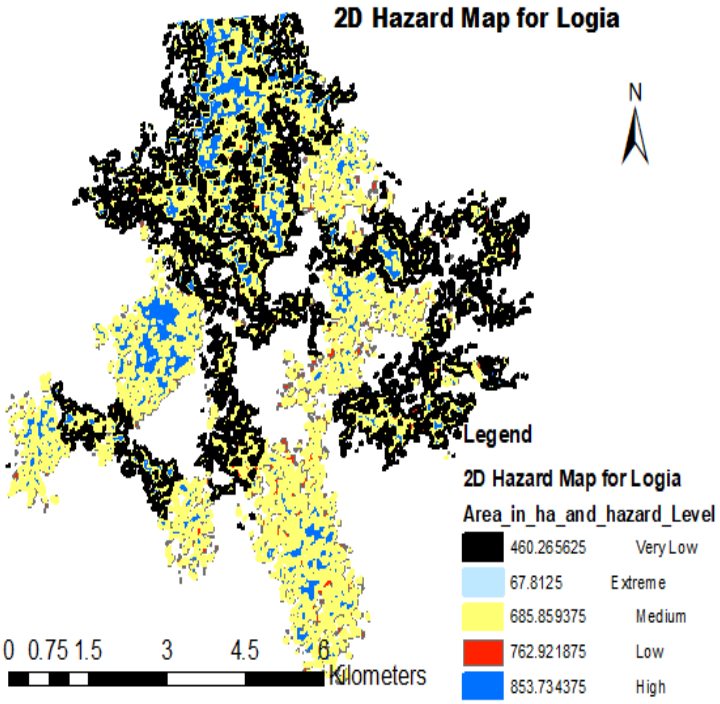

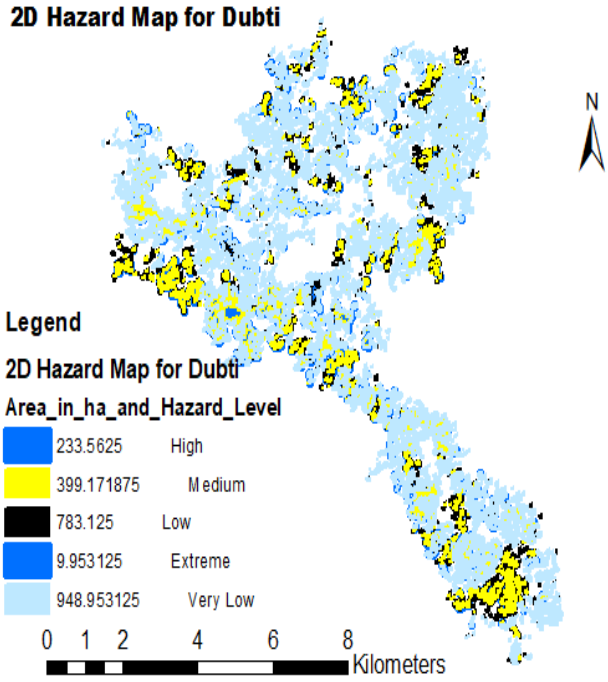

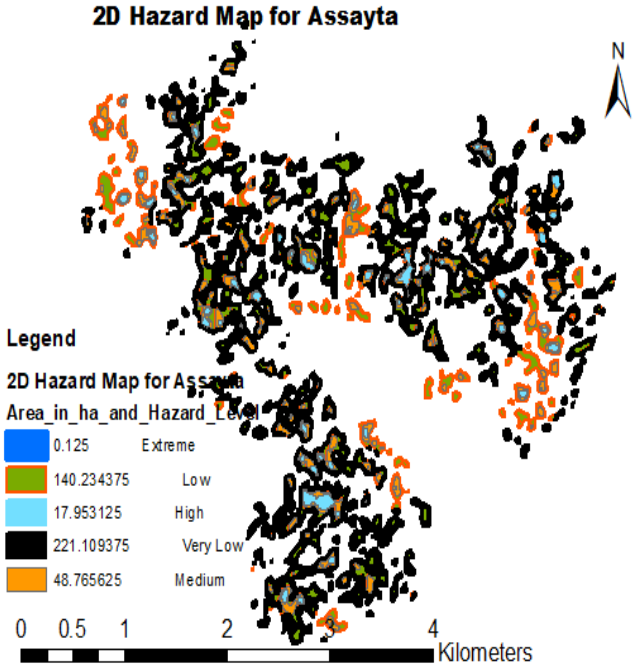

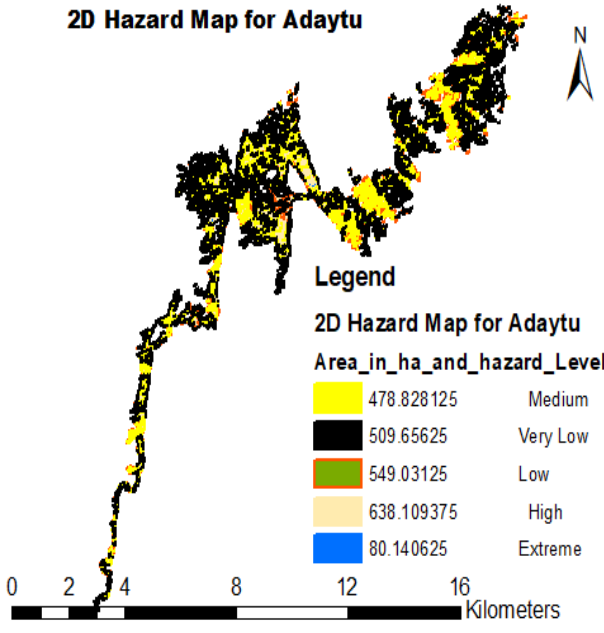

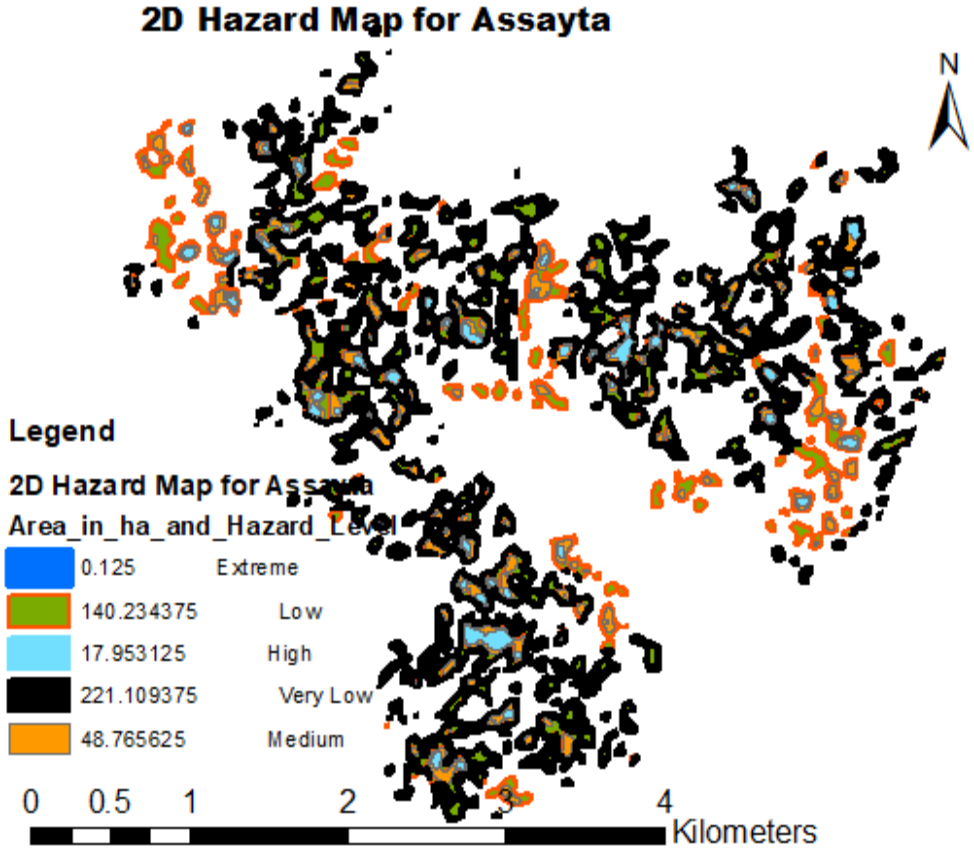
2D Hazard Map for Assayta
N
Legend
2D Hazard Map for Assayta
Area_in_ha_and_Hazard_Level
0.125 Extreme
140.234375 Low
17.953125 High
221.109375 Very Low
48.765625 Medium
0 0.5 1 2 3 4
Kilometers

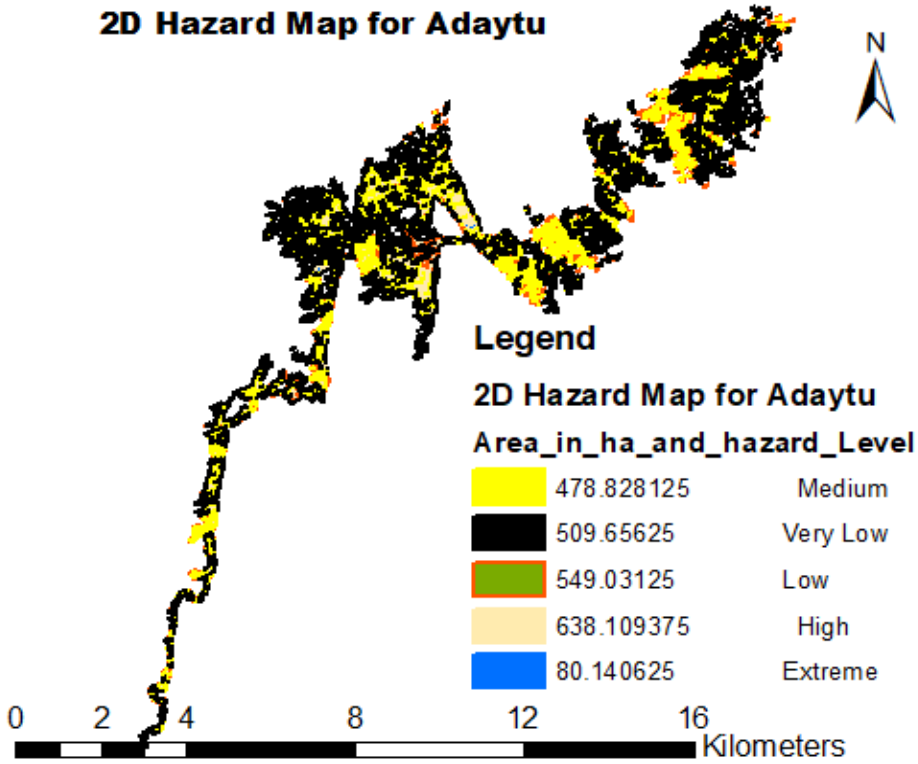
2D Hazard Map for Adaytu
N
Legend
2D Hazard Map for Adaytu
Area_in_ha_and_hazard_Level
478.828125 Medium
509.65625 Very Low
549.03125 Low
638.109375 High
80.140625 Extreme
0 2 4 8 12 16
Kilometers

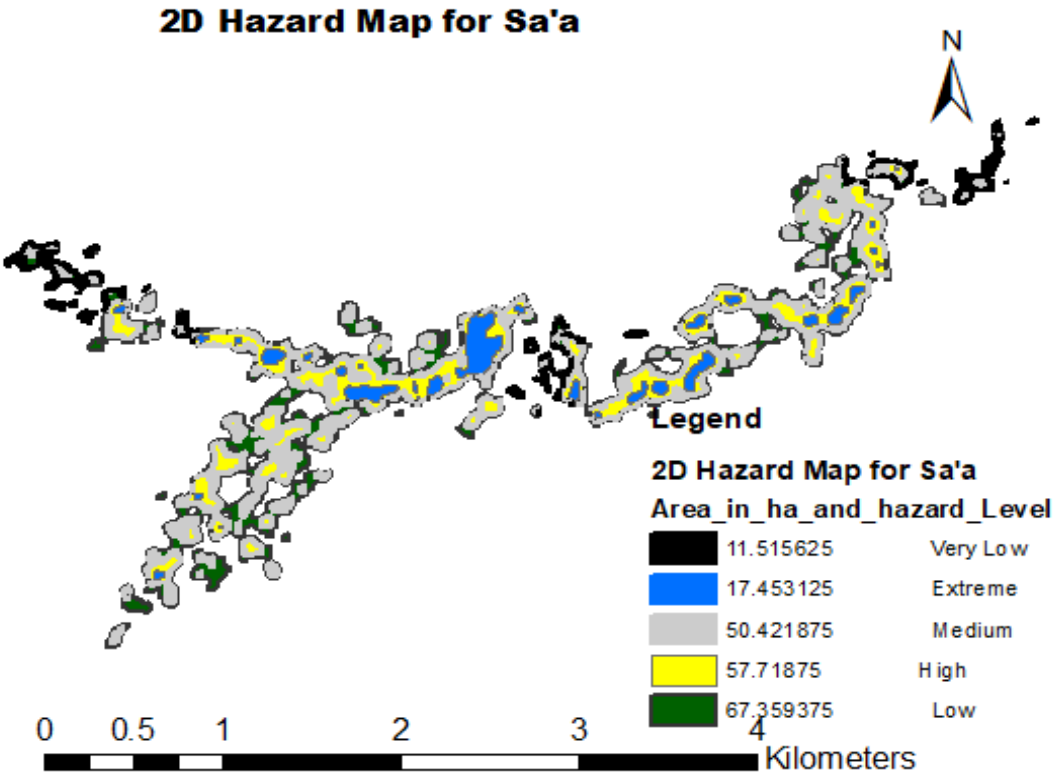
2D Hazard Map for Sa'a
N
Legend
2D Hazard Map for Sa'a
Area_in_ha_and_hazard_Level
11.515625 Very Low
17.453125 Extreme
50.421875 Medium
57.71875 High
67.359375 Low
0 0.5 1 2 3 4
Kilometers

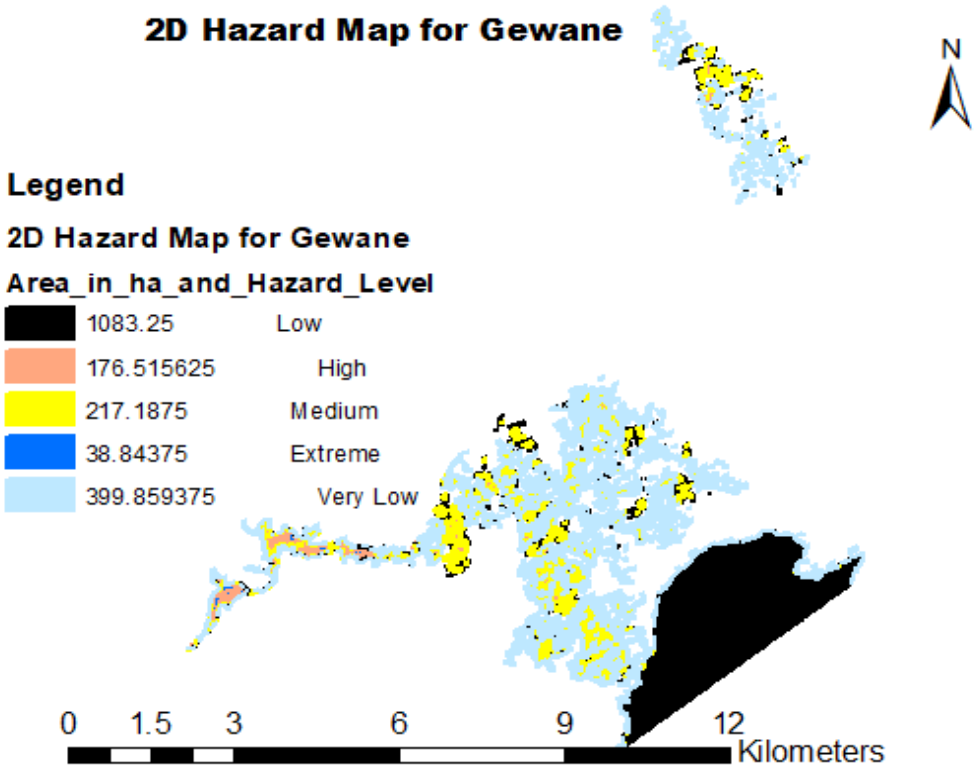
2D Hazard Map for Gewane
N
Legend
2D Hazard Map for Gewane
Area_in_ha_and_Hazard_Level
1083.25 Low
176.515625 High
217.1875 Medium
38.84375 Extreme
399.859375 Very Low
0 1.5 3 6 9 12
Kilometers

Appendix I: Code used to Visualize RGB

```
// Select images by predefined dates
var beforeStart = '2020-07-28';
var beforeEnd = '2020-08-05';
var afterStart = '2020-08-05';
var afterEnd = '2020-09-10';
// Assuming s1 is defined correctly as a Sentinel-1 image collection
var filtered = s1
  .filter(ee.Filter.eq('instrumentMode', 'IW'))
  .filter(ee.Filter.listContains('transmitterReceiverPolarisation', 'VH'))
  .filter(ee.Filter.listContains('transmitterReceiverPolarisation', 'VV'))
  .filter(ee.Filter.eq('orbitProperties_pass', 'DESCENDING'))
  .filter(ee.Filter.eq('resolution_meters', 10))
  .filterBounds(polygon)
  .select(['VV', 'VH']);
```

```
var before = filtered.filterDate(beforeStart, beforeEnd).mosaic().clip(polygon);
var after = filtered.filterDate(afterStart, afterEnd).mosaic().clip(polygon);


var addRatioBand = function(image) {
  var ratioBand = image.select('VV').divide(image.select('VH')).rename('VV/VH');
  return image.addBands(ratioBand);
};
```

```
var afterRgb = addRatioBand(after);
print(beforeRgb);
print(afterRgb);
print(filtered.first());
var visParams = {min:[-25, -25, 0] ,max:[0, 0, 2]};
Map.centerObject(polygon, 10);
Map.addLayer(beforeRgb, visParams, 'Before Floods');
Map.addLayer(afterRgb, visParams, 'After Floods');
```

Appendix J: Code used to Speckle Filter

```
var beforeFiltered = ee.Image(toDB(toNatural(before)));
var afterFiltered = ee.Image(toDB(toNatural(after)));
Map.addLayer(beforeFiltered, {min:-25,max:0}, 'Before Filtered', false);
Map.addLayer(afterFiltered, {min:-25,max:0}, 'After Filtered', false);
```

Appendix K: Code used to Apply Threshold

```
// Define a threshold
var diffThreshold = 1.25;

// Initial estimate of flooded pixels
var flooded = difference.gt(diffThreshold).rename('water').selfMask();
Map.addLayer(flooded, {min:0, max:1, palette:['orange']}, 'Initial Flood Area',false);
```

Appendix L: Code used to apply masks

```
// Mask out area with permanent/semi-permanent water

var permanentWater = gsw.select('seasonality').gte(5).clip(polygon)

Map.addLayer(permanentWater.selfMask(), {min:0, max:1, palette: ['blue']}, 'Permanent Water', false)

// GSW data is masked in non-water areas. Set it to 0 using unmask()

// Invert the image to set all non-permanent regions to 1

var permanentWaterMask = permanentWater.unmask(0).not()

var flooded = flooded.updateMask(permanentWaterMask)

// Mask out areas with more than 5 percent slope using the HydroSHEDS DEM

var slopeThreshold = 5;

var terrain = ee.Algorithms.Terrain(hydrosheds);

var slope = terrain.select('slope');

var steepAreas = slope.gt(slopeThreshold)

var slopeMask = steepAreas.not()

Map.addLayer(steepAreas.selfMask(), {min:0, max:1, palette: ['cyan']}, 'Steep Areas', false)

var flooded = flooded.updateMask(slopeMask)

// Remove isolated pixels

// connectedPixelCount is Zoom dependent, so visual result will vary

var connectedPixelThreshold = 8;

var connections = flooded.connectedPixelCount(25)

var disconnectedAreas = connections.lt(connectedPixelThreshold)

var disconnectedAreasMask = disconnectedAreas.not()

Map.addLayer(disconnectedAreas.selfMask(), {min:0, max:1, palette: ['yellow']}, 'Disconnected Areas', false)

var flooded = flooded.updateMask(disconnectedAreasMask)

Map.addLayer(flooded, {min:0, max:1, palette: ['red']}, 'Flooded Areas');
```

Appendix M: Code used to calculate the flooded area

```
// Calculate the total area of all features in the polygon collection
var totalArea = polygon.geometry().area().divide(10000); // Convert to hectares
print('Total Area (ha):', totalArea);
var stats = flooded.multiply(ee.Image.pixelArea()).reduceRegion({
  reducer: ee.Reducer.sum(),
  geometry: polygon,
  scale: 10,
  maxPixels: 1e10,
  tileScale: 16
})
print(stats)
var floodedArea = ee.Number(stats.get('water')).divide(10000)
print(floodedArea)
```

Appendix N: Codes used to export results to the GIS

```
// Convert the flooded raster image to a binary raster
var floodedAreaBinary = flooded.gt(0);
// Export the flooded area as a shapefile
Export.table.toDrive({
  collection: floodedAreaBinary.reduceToVectors({
    geometry: polygon,
    scale: 25,
    maxPixels: 1e9, // Adjust the maxPixels value
    eightConnected: false,
    labelProperty: 'water'
  }),
```

```
  description: 'flooded_area_shapefile',
  folder: 'GEE_exports',
  fileFormat: 'SHP'
});
```

```
// Export Disconnected Areas
Export.image.toDrive({
  image: disconnectedAreasMask,
  description: 'Disconnected_Areas',
  folder: 'GEE_exports',
  region: polygon.geometry(),
  scale: 10,
  maxPixels: 1e13,
  fileFormat: 'GEOTIFF',
  formatOptions: {
    cloudOptimized: true } });
// Export the permanent Water as a shapefile
Export.table.toDrive({
  collection: permanentWaterBinary.reduceToVectors({
    geometry: polygon,
    scale: 20,
    maxPixels: 1e9, // Adjust the maxPixels value
    eightConnected: false,
    labelProperty: 'water'
  }),
  description: 'permanent_Water_shapefile',
  folder: 'GEE_exports',
  fileFormat: 'SHP' });
```

```
// Convert the Initial Flood Area raster image to a binary raster
var InitialFloodAreaBinary = flooded.gt(0);
// Export the Initial flooded area as a shapefile
Export.table.toDrive({
  collection: InitialFloodAreaBinary.reduceToVectors({
    geometry: polygon,
    scale: 20,
    maxPixels: 1e9, // Adjust the maxPixels value
    eightConnected: false,
    labelProperty: 'water'
  }),
  description: 'Initial_Flood_Area_shapefile',
  folder: 'GEE_exports',
  fileFormat: 'SHP'});
```

```
// Export After Filtered
Export.image.toDrive({
  image: afterFiltered,
  description: 'After_Filtered',
  folder: 'GEE_exports',
  region: polygon.geometry(),
  scale: 10,
  maxPixels: 1e13,
  fileFormat: 'GeoTIFF',
  formatOptions: {
    cloudOptimized: true  }  });
```

```
// Export Before Filtered
Export.image.toDrive({
  image: beforeFiltered,
  description: 'Before_Filtered',
  folder: 'GEE_exports',
  region: polygon.geometry(),
  scale: 10,
  maxPixels: 1e13,
  fileFormat: 'GeoTIFF',
  formatOptions: {
    cloudOptimized: true}
});
// Export After Floods
Export.image.toDrive({
  image: afterRgb,
  description: 'After_Floods',
  folder: 'GEE_exports',
  region: polygon.geometry(),
  scale: 10,
  maxPixels: 1e13,
  fileFormat: 'GeoTIFF',
  formatOptions: {
    cloudOptimized: true
  }
});
```

```
// Export Before Floods
Export.image.toDrive({
  image: beforeRgb,
  description: 'Before_Floods',
  folder: 'GEE_exports',
  region: polygon.geometry(),
  scale: 10,
  maxPixels: 1e13,
  fileFormat: 'GeoTIFF',
  formatOptions: {
    cloudOptimized: true
  }
});
```

Appendix O: GEE Flood inundation and Affected LULC

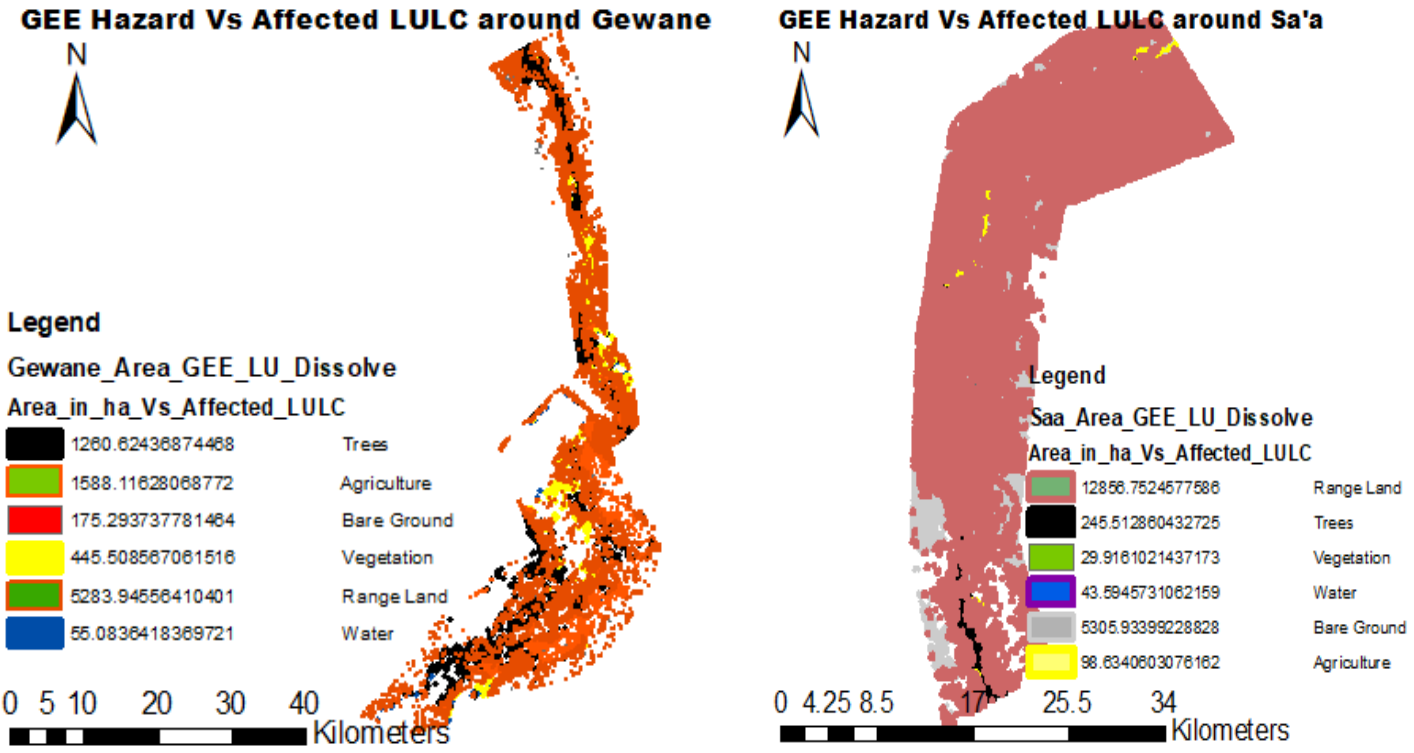

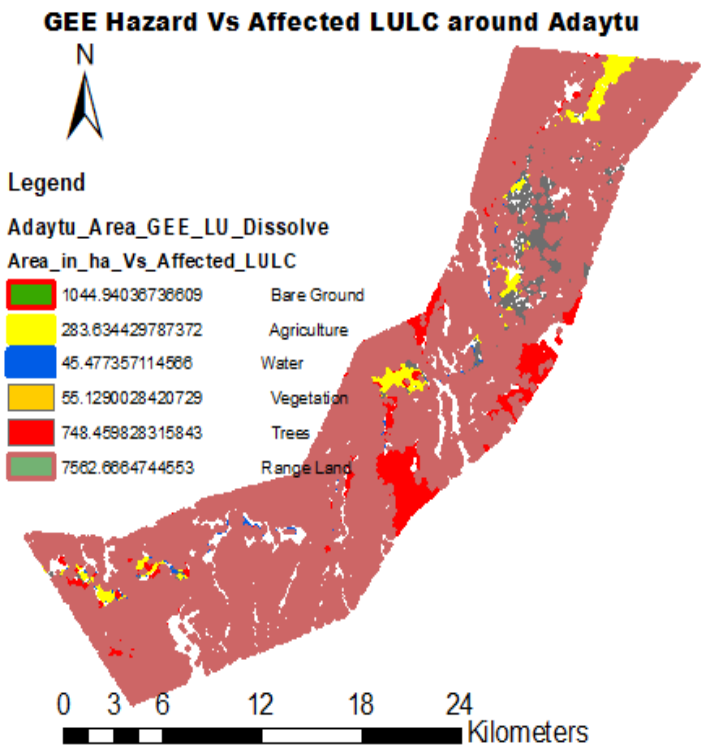
GEE Hazard Vs Affected LULC around Adaytu
N
Legend
Adaytu_Area_GEE_LU_Dissolve
Area_in_ha_Vs_Affected_LULC
1044.94036736609 Bare Ground
283.634429787372 Agriculture
45.477357114566 Water
55.1290028420729 Vegetation
748.459828315843 Trees
7562.6664744553 Range Land
0 3 6 12 18 24
Kilometers

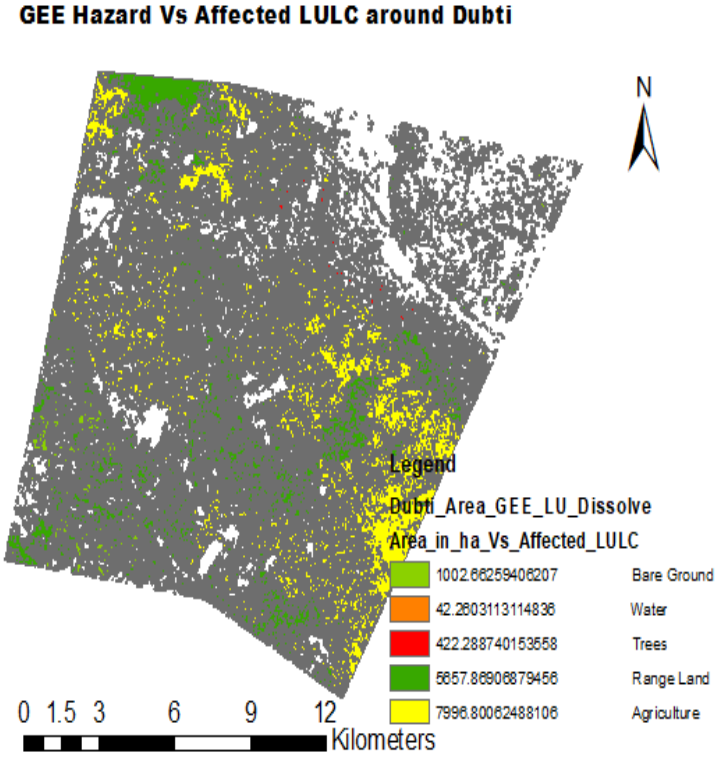
GEE Hazard Vs Affected LULC around Dubti
N
Legend
Dubti_Area_GEE_LU_Dissolve
Area_in_ha_Vs_Affected_LULC
1002.66259406207 Bare Ground
42.2603113114836 Water
422.288740153558 Trees
5657.86906879456 Range Land
7996.80062488106 Agriculture
0 1.5 3 6 9 12
Kilometers

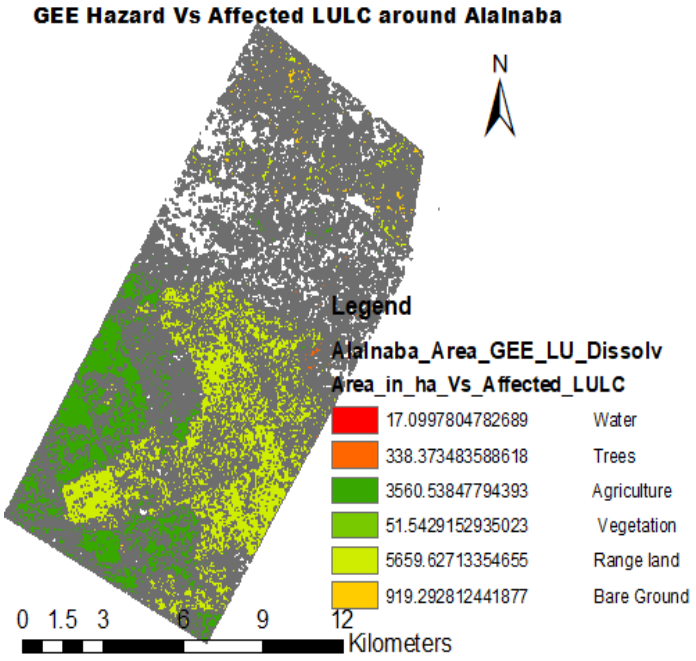
GEE Hazard Vs Affected LULC around Alalnaba
N
Legend
Alalnaba_Area_GEE_LU_Dissolv
Area_in_ha_Vs_Affected_LULC
17.0997804782689 Water
338.373483588618 Trees
3560.53847794393 Agriculture
51.5429152935023 Vegetation
5659.62713354655 Range land
919.292812441877 Bare Ground
0 1.5 3 6 9 12
Kilometers

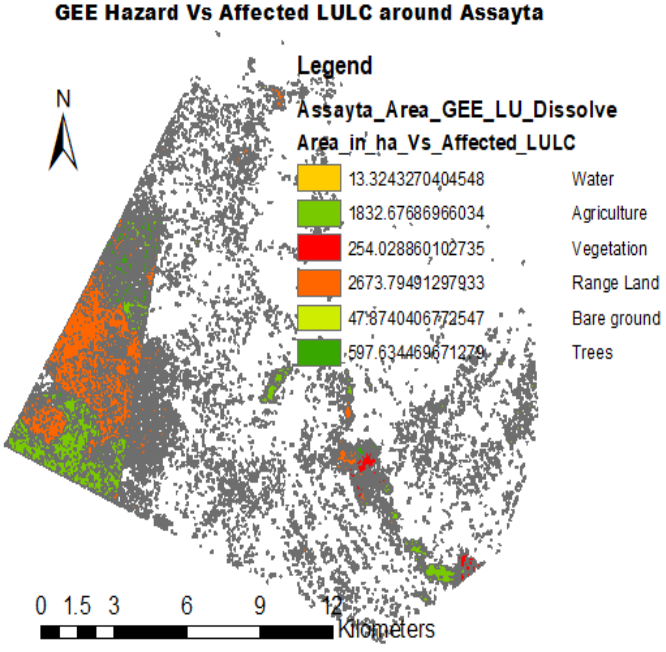
GEE Hazard Vs Affected LULC around Assayta
N
Legend
Assayta_Area_GEE_LU_Dissolve
Area_in_ha_Vs_Affected_LULC
13.3243270404548 Water
1832.67686966034 Agriculture
254.028860102735 Vegetation
2673.79491297933 Range Land
47.8740406772547 Bare ground
597.634469671279 Trees
0 1.5 3 6 9 12
Kilometers